University of Cyprus
Department of Chemistry

Doctor of Philosophy

Structural characterization of organic conjugated dyes through vibrational and time-resolved spectroscopic techniques

Elisa Alloa

November 2019

University of Cyprus
Department of Chemistry

Doctor of Philosophy Dissertation

Structural characterization of organic conjugated dyes through vibrational and time-resolved spectroscopic techniques

Elisa Alloa

A Dissertation Submitted to the University of Cyprus in Partial Fulfillment of the Requirements for the Degree of Doctor of Philosophy

November 2019

VALIDATION PAGE

Doctoral Candidate: Elisa Alloa

Doctoral Thesis Title: Structural characterization of organic conjugated dyes through vibrational and time-resolved spectroscopic techniques

*The present Doctoral Dissertation was submitted in partial fulfillment of the requirements for the Degree of Doctor of Philosophy at the **Department of Chemistry** and was approved on the 5th December 2019 by the members of the **Examination Committee**.*

Examination Committee:

Research Supervisor:

Sophia C. Hayes, Associate Professor_____

(Name, position and signature)

Committee Member:

Costas S. Patrickios, Professor_____

(Name, position and signature)

Committee Member:

Theodora Krasia, Associate Professor_____

(Name, position and signature)

Committee Member:

Panagiotis Keivanidis, Associate Professor_____

(Name, position and signature)

Committee Member:

Eftychia Pinakoulaki, Associate Professor_____

(Name, position and signature)

DECLARATION OF DOCTORAL CANDIDATE

Most of the experiments presented in this study were performed at the Molecular Spectroscopy Laboratory at the Department of Chemistry of the University of Cyprus by the undersigned under the supervision of Associate Professor Dr. Sophia C. Hayes. Some experiments were also performed at the Department of Chemistry of the University of Genova under the supervision of Professor Marina Alloisio and at the Department of Physics of the University of Valencia under the supervision of Professor Antonio Díez Cremades. The DFT calculations presented in the *Appendix* (Chapter 10) were performed at the University of Würzburg by Dr. Vincenzo Grande (Professor Frank Würthner) and at the University of Mons by Rishat Dilmurat (Professor David Beljonne). Dr. Vincenzo Grande synthesized the PBI materials at the University of Würzburg. Associate Professor Eftychia Pinakoulaki provided access to the FTIR instrument at the Department of Chemistry, University of Cyprus. Oligofluorenes analysis was conducted with the collaboration of the Central Laser Facility, STFC, Rutherford Appleton Laboratory, UK, through the Laserlab-Europe. I have analyzed these results and related them to my experimental work.

…………………………………………….. [Date]

………………………………………………… [Full Name of Doctoral Candidate]

…………………………………………….. [Signature]

To the memory of my Dad,

To my Family,

To my Beloved.

Acknowledgements

The completion of this Dissertation depends on the motivation, inspiration and support coming from many people, dropping in and out of my life along these years and across different countries. It will not be possible to greet them all one by one, however I value and recognize whoever took part to my life along this time, as all those moments somehow influenced me at different levels to finally get to this success.

First and foremost, I want to express my sincere gratitude to my supervisor, Associate Professor Sophia C. Hayes, for her patience, guidance, motivation and support in the overall research experience, as well as in the difficult transitions and challenges along this path. She represents to me an excellent and hard-working scientist, and I admire her capability to be so skillful, besides her professional capabilities, as a wholly realized human being. Without her careful supervision and tenacious help this thesis would not have come to life.

Besides my advisor, I would like to thank Professor Costas Patrickios, Associate Professor Eftychia Pinakoulaki, Associate Professor Theodora Krasia, and Assistant Professor Panos Keivanidis for accepting the invitation to be members of my examination committee.

In addition, a thank you to Professor Carlos Silva, Dr. Claudia Bazán, Professor Marina Alloisio, Professor Davide Comoretto, Professor Miguel V. Andrés and Professor Antonio Díez Cremades for hosting and supervising me during my trainings abroad at the University of Montreal, Genova and Valencia.

I am grateful to all the academic, technical, administrative personnel and fellow students of this department for making me feel like a part of this family throughout my doctoral studies.

A very special thank you goes to the members of the Molecular Spectroscopy Lab, and especially Irene and Iliana for the friendly collaboration and the pleasant working environment we have lived over these years and I wish them all the best for their future.

A warm thanks goes to Eliza, Michalis, Andreas, Galina, Anthoula, Elena, Gigi, Benedetta, Eros, Antuan, Xristos and Mirko: my mind and my heart kept inspired and nurtured thanks to the experiences and emotions we shared across time and space, in Cyprus, Spain and Italy.

I deeply thank my whole family for supporting with constant encouragement my educational path and with a renewal strength a tough life transition in a crucial moment of my PhD. I am grateful and honored to my late Dad Franco for always believing in me and to my Mum Maria Angela for all her efforts for my highest good. Last but not least, the blissful birth of my beloved Godson Gioele has been along this time a deep source of joy and inspiration, keeping me connected with home despite the distance.

Love.

ABSTRACT

The development of optoelectronics applications is directly related to the structural characterization of organic conjugated molecules. Vibrational spectroscopy represents an effective method to study conformational changes of organic molecules under variable conditions and it is employed here on perylenes (PBIs), oligofluorenes (OFs) and polydiacetylenes (PCDAs) in order to accomplish specific requirements in the field.

Understanding the transition from isolated molecules/monomers to an organized macrostructure is crucial for exploring the potential of aggregated systems in the field of condensed matter physics. The self-assembly process can drive the single units to create beautiful supramolecular structures with valuable photophysical properties, outstandingly provided by their systematized and ordered conformation. Perylene bisimides (PBIs) are dyes known for combining high absorption and emission in the visible region with their thermal and photochemical stability. H-bond-directed aggregation driven by free imide groups has been reported to promote the uncommon J-type aggregate formation of PBIs. J-aggregates are highly desired thanks to their bathochromically shifted narrow absorption and fluorescence due to excitonic coupling, together with hyperchromicity and superradiance compared to the monomer. Herein we present a water-soluble PBI (MEG-PBI, meta-ethyleneglycol tetraphenoxy PBI) showing interesting aggregation in water and in the solid state. Unlike its hydrophobic counterparts, MEG-PBI aggregates in water upon increasing temperature, indicating an entropy driven self-assembly. Temperature-dependent Resonance Raman (RR) spectroscopy was employed for the structural characterization of MEG-PBI in aqueous solution versus toluene and in aggregated thin films, employing excitation at different wavelengths to probe the contribution of various chromophores to the supramolecular structure of the aggregate. We find that the perylene core distorts upon aggregation, where the bonds along the perylene long N-N axis lengthen and the ones

perpendicular to that shorten, suggesting a head-to-tail arrangement due to H-bonding between neighboring units.

Important to optoelectronics applications is also the excited state evolution following photoexcitation, especially when methods of structural characterization are employed to decipher the exact species that are formed upon excitation of π-conjugated oligomers and polymers. We have applied Femtosecond Stimulated Raman Spectroscopy (FSRS) as a tool to investigate the ultrafast dynamics of a series of oligofluorene compounds with the goal of understanding the vibrational mode-specific dynamics that are associated with the early time relaxation of the electronic excited states, and how these depend on oligomer chain length. Polyfluorene is an archetypical π-conjugated "blue" emitting polymer and, as such, various aspects of its photophysics have been investigated by a wealth of spectroscopic methods. In the fluorene trimer we observe unique evolution in the photoinduced absorption bandshape, which is related to structural relaxation occurring on sub-15 ps timescales occurring post electronic excitation to the ^1B_u state.

A variant of the FSRS technique, inverse/stimulated Raman spectroscopy, employing nanosecond pulses and photonic fibers, has also been initiated within this Thesis. Stimulated Raman will be applied in the case of very fluorescent samples, such as the PBIs molecules investigated here, while Inverse Raman will be used for all-optical switching in organic materials. In the latter case, the material of choice, polydiacetylene (PCDA) coupled to nanoparticles has been synthesized, where large surface enhancement of the $\boldsymbol{C \equiv C}$ stretch scattering will lead to better switching capabilities.

To conclude, different techniques of vibrational spectroscopy have provided insights into the conformation of different materials, leading to a better understanding of conjugated organic systems. Moreover, a step towards a functional application will result from the implementation of the inverse Raman technique.

ΠΕΡΙΛΗΨΗ

Η ανάπτυξη οπτοηλεκτρονικών εφαρμογών εξαρτάται άμεσα από το δομικό χαρακτηρισμό των οργανικών συζυγιακών μορίων. Η δονητική φασματοσκοπία αποτελεί μια αξιόπιστη μέθοδο για τη μελέτη αλλαγών στη διαμόρφωση των οργανικών μορίων κάτω από μεταβλητές συνθήκες και εφαρμόζεται στην παρούσα μελέτη σε περυλένια, ολιγοφθορένια και πολυδιακετυλένια προκειμένου να απαντήσει συγκεκριμένα επιστημονικά ερωτήματα. Η κατανόηση της μετάβασης από τα ανεξάρτητα μόρια/μονομερή σε μια οργανωμένη μακροδομή είναι σημαντική για τη μελέτη της δυναμικής των συσσωματωμένων συστημάτων στο πεδίο της φυσικής της συμπυκνωμένης ύλης. Η διαδικασία της αυτοργάνωσης μπορεί να οδηγήσει μεμονωμένα μόρια στη δημιουργία εντυπωσιακών υπερμοριακών δομών με σημαντικές φωτοφυσικές ιδιότητες, που προκύπτουν από τη συστηματική και οργανωμένη διαμόρφωσή τους. Τα περυλενικά δι-ιμίδια (Perylene bisimides (PBIs)) είναι χρωστικές γνωστές για το συνδυασμό υψηλής απορρόφησης και φθορισμού στην περιοχή του ορατού με τη θερμική και φωτοχημική σταθερότητα. Η συσσωμάτωση επαγόμενη από δεσμούς υδρογόνου μεταξύ ελευθέρων ιμιδικών ομάδων, έχει παρατηρηθεί ότι προάγει την ασυνήθιστη συσσωμάτωση τύπου J των PBIs. Η συσσωμάτωση τύπου J προσδίδει κάποια εξαιρετικά επιθυμητά χαρακτηριστικά συγκριτικά με το μονομερές, όπως η βαθοχρωμική μετατόπιση του στενού φάσματος απορρόφησης και φθορισμού λόγω της εξιτονικής σύζευξης, σε συνδυασμό με τον υπερ-χρωμισμό και το superradiance. Στην παρούσα μελέτη παρουσιάζουμε το υδατοδιαλυτό MEG-PBI (meta-ethyleneglycol tetraphenoxy PBI) που παρουσιάζει ενδιαφέρουσα συμπεριφορά συσσωμάτωσης στο νερό και στη στερεά κατάσταση. Αντίθετα με τα αντίστοιχα υδρόφοβα, το MEG-PBI συσσωματώνεται στο νερό με την αύξηση της θερμοκρασίας, υποδηλώνοντας μια εντροπικά υποκινούμενη αυτό-οργάνωση. Για το δομικό χαρακτηρισμό του MEG-PBI σε υδάτινο διάλυμα, σε διαλύτη τολουολίου και σε συσσωματωμένο λεπτό υμένιο χρησιμοποιήθηκε Φασματοσκοπία Raman Συντονισμού

θερμοκρασιακής εξάρτησης, σε διαφορετικά μήκη κύματος προκειμένου να διερευνηθεί η συνεισφορά των διάφορων χρωμοφόρων ομάδων στην υπερ-μοριακή δομή του συσσωματώματος. Βρήκαμε ότι ο περυλενικός πυρήνας διαταράσσεται κατά τη συσσωμάτωση, καθώς οι δεσμοί κατά μήκος του άξονα N-N του περυλενίου επιμηκύνονται και αυτοί που είναι κάθετοι σε αυτές συμπιέζονται, υποδεικνύοντας μια διάταξη head-to-tail λόγω των δεσμών υδρογόνου μεταξύ γειτονικών μονάδων.

Σημαντική για οπτοηλεκτρονικές εφαρμογές είναι επίσης η εξέλιξη της διεγερμένης κατάστασης μετά από φωτοδιέγερση, και η αποσαφήνιση των ακριβών ειδών που σχηματίζονται κατά τη διέγερση των π-συζευγμένων ολιγομερών και πολυμερών που πραγματοποιείται με μεθόδους δομικού χαρακτηρισμού. Χρησιμοποιήσαμε την υπεργρήγορη Φασματοσκοπία Επαγόμενου Σκεδασμού Raman (Femtosecond Stimulated Raman Spectroscopy, FSRS) σαν εργαλείο για την διερεύνηση των υπερ-ταχέων δυναμικών διεργασιών μιας σειράς ενώσεων ολιγοφθορενίου με στόχο να κατανοήσουμε τις δυναμικές διεργασίες του κάθε τρόπου δόνησης που αφορούν σε γρήγορους χρόνους χαλάρωσης των ηλεκτρονικών διεγερμένων καταστάσεων, και πως αυτές σχετίζονται με το μήκος της αλυσίδας του ολιγομερούς. Το πολυφθορένιο είναι ένα αρχέτυπο π-συζυγιακό πολυμερές που εκπέμπει στο «μπλε» φάσμα και ως τέτοιο, διάφορες πτυχές της φωτοφυσικής του έχουν μελετηθεί από μια ποικιλία φασματοσκοπικών μεθόδων. Στο τριμερές του φθορενίου παρατηρούμε μια μοναδική εξέλιξη στο σχήμα του φάσματος απορρόφησης της διεγερμένης κατάστασης, που αφορά σε δομική χαλάρωση του ολιγομερούς που συμβαίνει στη χρονοκλίμακα <15 ps μετά την ηλεκτρονική διέγερση στην κατάσταση ^1B_u.

Μια παραλλαγή της τεχνικής FSRS, η φασματοσκοπία Επαγόμενου Σκεδασμού Raman, που χρησιμοποιεί παλμούς nanosecond και φωτονικές ίνες, έχει εφαρμοστεί στα πλαίσια αυτής της Διατριβής. Η τεχνική αυτή στοχεύει να εφαρμοστεί σε δείγματα με μεγάλο φθορισμό όπως τα μόρια PBI που μελετήθηκαν, ενώ η αντίστροφη φασματοσκοπία Raman (Inverse Raman) θα χρησιμοποιηθεί για οπτική μεταγωγή (all-optical switching) σε οργανικά υλικά.

Στην τελευταία περίπτωση, το υλικό που επιλέχθηκε είναι το πολυδιακετυλένιο (PCDA) εμπλουτισμένο με νανοσωματίδια, όπου η μεγάλη επιφανειακή ενίσχυση που παρουσιάζει η σκέδαση της διάτασης του $C \equiv C$ δεσμού θα οδηγήσει σε καλύτερες μεταγωγικές ικανότητες.

Κλείνοντας, διαφορετικές τεχνικές δονητικής φασματοσκοπίας παρείχαν σημαντικές πληροφορίες σχετικά με τη διαμόρφωση διαφόρων υλικών, οδηγώντας σε καλύτερη κατανόηση των οργανικών υλικών. Επιπλέον, η εκτέλεση της τεχνικής αντίστροφης φασματοσκοπίας Raman, θα μας φέρει ένα βήμα πιο κοντά σε λειτουργικές εφαρμογές.

TABLE OF CONTENTS PAGE

LIST OF FIGURES

LIST OF TABLES

TABLE   **PAGE**

ABBREVIATIONS AND SYMBOLS

DFT	Density Functional Theory
TD-DFT	Time Dependent - DFT
HOMO	Higher occupied molecular orbital
LUMO	Lower unoccupied molecular orbital
n	Index of refraction
RR	Resonance Raman
SRS	Stimulated Raman spectroscopy
IRS	Inverse Raman spectroscopy
TA	Transient Absorption
UV	Ultraviolet
UV-vis	Ultraviolet visible
VIS	Visible
FTIR	Fourier Transform Infrared Spectroscopy
FSRS	Femtosecond stimulated Raman
TRRR	Time-resolved Resonance Raman
OF	Oligofluorene
PBI	Perylene Bisimide
MEG-PBI	meta-ethyleneglycol tetraphenoxy PBI
PEH-PBI	2-ethylhexyl-substituted gallic acid tetraphenoxy PBI

PCDA	Polydiacetylene
NPs	Nanoparticles
AERS	Aggregation-enhanced Raman scattering
PCF	Photonic Crystal Fiber
λ	Wavelength
α	Polarizability
μ	Reduced mass
σ	Raman cross section
E_s	Incident energy
E_s	Scattered energy
i	Initial vibrational state
f	Final vibrational state
c	Speed of the light
LCOF	Liquid core optical fiber

CHAPTER 1

Introduction

The focus of this Doctoral thesis is the structural characterization of organic conjugated molecules with the use of Resonance Raman spectroscopy. The work concentrates on materials for optoelectronics applications, specifically perylene bisimides (PBIs), oligofluorenes (OFs) and polydiacetylenes (PCDAs).

Organic optoelectronics is an area of research that has seen substantial growth during the past decade, thanks to the success of devices such as organic light-emitting diodes (OLEDs), organic semiconductors and optical switches. Advances[1,2] in the field have been achieved by moving from small molecules and polymers with desirable electronic properties to electronically active π-conjugated molecules capable of self-assembly through non-covalent forces, such as hydrogen bonding, electrostatic forces, metal–ligand, dipole–dipole, hydrophobic, π–π interactions, and steric repulsion. Even inspiration from the biological world had an influence in the field: similarly to light harvesting systems in photosynthetic antenna complexes, in supramolecular assemblies the excitation is coherently transferred by resonant emission and absorption phenomena from one molecule to a neighboring one, i.e., dye molecules play directly the role of transferring units.[3] These excitons can extend over ordered and coupled molecular units in the solid state, where the packing arrangement of the aggregates governs the favored optical outcome for the chosen technological application.[4] Supramolecular assemblies deliver a strong impact on opto-electronics as they offer the chance to create structures that incorporate directed molecular order, with significant dynamics through bond reversibility.[5] To develop organic semiconductor technologies, it is necessary to understand the complex structural arrangements and processes present in the materials and how these can affect device performance. Spectroscopic methods can provide insights in the supramolecular assembly, utilizing external stimuli such as temperature to tune the desired spectral state of the chemical system.[6,7,8]

Within this research field, J-aggregates constitute a particularly interesting class of materials, especially in organic photonics due to the fact that self-assembly of molecules into a head-to-tail arrangement results in coherent π-electron states that are delocalized over part of the

molecular aggregate.[9] Perylene bisimides represent a highly interesting class of dyes for J-aggregates, with very promising functional properties, which were recently exploited in all-polymer photonic microcavities.[10] Differently from previously developed PBIs soluble in organic solvents, this chemical system has been named "aquamaterial"[11,12] because of its capability to behave as a hydrogel-like material with unique and useful properties: the red-to-blue color transition appears indeed to be exploitable in the development of cutting-edge applications e.g., as photonic material in microcavities or as lyotropic liquid crystals. Its unique properties primarily derive from its large extended π-systems, together with its various supramolecular aggregate-based architectures.[13] H-bonded aggregation driven by self-complementary free-imide groups has also been reported to promote alternative J-type aggregate formation in non-polar solvents.[14] Thanks to non-covalent connectivity, such PBIs form very sophisticated supramolecular fibers, enabling interesting photophysics involving exciton coherence and migration.[15] In this study, the transition from a monomer-like state to an ordered J-aggregated state (and vice versa) was investigated through spectroscopic methods, in order to elucidate the driving forces and mechanisms of aggregation of these promising supramolecular architectures. Different excitation wavelengths were used in order to resonantly enhance the signal from specific chromophores in the molecule. FT-IR was used to complement the study. A theoretical model for H/J aggregates was also employed in order to predict the type of aggregation of our molecule from the optical spectra.

The fluorescence exhibited by technologically important molecules such as J aggregates, while useful from the application point of view, it can be an impediment in their investigation especially in the case of resonance Raman spectroscopy. Fluorescence can overwhelm any useful Raman signal, therefore, we have initiated the development of a Raman setup that exploits stimulated Raman scattering that completely eliminates such fluorescent backgrounds. A collaboration with the University of Valencia was established in order to obtain appropriate optical fibers to generate supercontinuum light, which is necessary in this technique as a probe pulse. Our efforts concentrated on obtaining this supercontinuum using nanosecond pulses. Subsequently, a pump will be coupled and synchronized with the probe in time and space. Depending then on the excitation wavelength used, gains or losses will be monitored in the spectrum, obtaining, respectively, the stimulated or inverse Raman. The same setup can be used for Inverse Raman Scattering, which can be used as a means for all-optical switching in organic conjugated materials, with applications in the communications industry.[16,17] A collaboration with the University of Genova was established in order to obtain appropriate samples for the inverse Raman experiment:.Polydiacetylene (PCDA) was

chosen for its intense and well-defined Raman spectra (with a limited number of peaks, contrary to the case of β-carotene exemplified in the literature)[16] and coupled to nanoparticles, in order to additionally increase the Raman signal, and consequently enhance the Inverse Raman Scattering as well. PCDA exhibits a unique spatial arrangement. Its extended π-system of diynes allows a self-assembly topochemical polymerization among the chains. PCDA is a supramolecular system with thermochromic properties enabled through the twisting of the polymer backbone. The unique colorimetric and fluorescent transition of PCDAs in response to different external stimuli, makes this system useful for biosensing applications.[18]

Central to the successful application of conjugated molecules for optoelectronics applications is the understanding of their excited state processes following photoexcitation. The structural rearrangement of molecular systems is intimately tied to their excited state evolution. Thus, a powerful structural method was employed herein, femtosecond stimulated Raman spectroscopy to monitor the ultrafast structural dynamics of electronic excited states of π-conjugated oligomers and polymers, on time scales down to a few tens of femtoseconds. A series of oligofluorene compounds was chosen with the goal of understanding the mode-specific dynamics that are associated with the early relaxation of the electronic excited state. Correlation of this information with oligomer chain length can provide further insights into the relaxation process happening at early time stages in polymeric systems.

The overall aim of this doctoral dissertation is to study conformational changes of organic molecules under variable conditions. To sum up, firstly, Resonance Raman spectroscopy was used to structurally investigate the ground state conformation of perylene bisimide analogues with different chemical features. Secondly, the development of the stimulated/inverse Raman setup came as a consequence of the intense fluorescence exhibited by our PBI system and it turned out as a potential way to collaterally obtain the all-optical switching signal intended for technological applications. Finally, a series of fluorene oligomers were analyzed and compared to one another through a femtosecond stimulated Raman (FSRS) experiment in order to understand conformational evolution in the excited state at very early times following excitation. .

The originality of the present doctoral dissertation rests on the use of different vibrational spectroscopic techniques to provide insights into the conformation of different materials, in a wide range of conditions, leading to a better understanding of conjugated organic systems. As a first step, the investigation of a water-soluble PBI system involved in self-assembly

represents a promising avenue for its possible exploitation in biological systems. Resonance Raman (RR) spectroscopy was used to elucidate the structure of the PBI monomers in the assembly. Even though RR has been utilized for the characterization of a plethora of supramolecular systems, PBIs have only been analyzed by Raman spectroscopy as individual molecules[19,20] and not in their J aggregated state. Furthermore, based on our experience with PBIs, the development of a method of vibrational analysis using nanosecond pulses and photonic fibers was initiated for the case of very fluorescent samples, i.e., the inverse/stimulated Raman technique. PCDA coupled to nanoparticles was prepared to be used for the first time for all-optical switching applications. Moreover, the power of ultrafast Raman spectroscopy for probing structural dynamics in photoexcited chemical systems is employed here for the first time to systematically probe excited-state relaxation in a series of conjugated oligomeric model materials (oligofluorenes) to provide insights on the underlying photophysics at very early time stages following excitation.

The thesis is organized as follows.

In *Chapter 2* we review the literature on the aggregation phenomenon, starting from a background on its discovery, on the photophysical properties that these supramolecular structures entail and on the broad variety of J-aggregate dyes employed in optoelectronics, with a special section dedicated to perylene bisimide. Electronic excited states of π-conjugated polymers are also investigated in this work in order to explore their ultrafast dynamics: in this light, oligofluorenes are briefly reviewed. Another conjugated polymer is presented in this Chapter, polydiacetylene decorating nanoparticles, which will be used in a future study for all-optical switching applications.

In *Chapter 3* we describe in detail the experimental and theoretical methods used in this work. Perylene bisimide (PBI) aggregation was studied through Resonance Raman (RR) spectroscopy for the first time in its water soluble form. The main aspects and the theoretical background of Resonance Raman spectroscopy, which is the main experimental technique used in this work, are also discussed in this Chapter, including a brief description of the Stimulated (SRS) and inverse (IRS) Raman techniques and Femtosecond stimulated Raman spectroscopy (FSRS). Details on the theoretical calculations that complement our study are also presented here.

Chapter 4 describes the visible and UV Resonance Raman study for elucidating the J-type aggregation of a water-soluble perylene bisimide. FTIR complemented the findings.

Deuterated water and toluene supported the outcome of these results. Subsequently, a comparison with a PBI soluble in organic media is analyzed in *Chapter 5*.

The excited state relaxation of a series of oligofluorenes is explored in *Chapter 6* through femtosecond stimulated Raman. The main goal is to elucidate how such dynamics are influenced by oligomer chain length.

Chapter 7 presents the initiation of the development of a stimulated/inverse Raman setup, which is an ongoing project work. The thesis will close with the conclusions derived from this work (*Chapter 8*) and the future perspectives that arise (*Chapter 9*), suggesting potential future research on issues that are still open.

References

1. Whitesides, G. M. & Boncheva, M. Beyond molecules: self-assembly of mesoscopic and macroscopic components. *Proc. Natl. Acad. Sci. U. S. A.* **99**, 4769–74 (2002).

2. Olenyuk, B., Whiteford, J. A., Fechtenkötter, A. & Stang, P. J. Self-assembly of nanoscale cuboctahedra by coordination chemistry. *Nature* **398**, 796–799 (1999).

3. Saikin, S. K., Eisfeld, A., Valleau, S. & Aspuru-Guzik, A. Photonics meets excitonics: natural and artificial molecular aggregates. *Nanophotonics* **2**, 21–38 (2013).

4. Sorokin, A. V., Ropakova, I. Y., Borovoy, I. A., Bespalova, I. I. & Yefimova, S. L. Using cyanine dye J-aggregates as luminescence probe for nanostructured media. *Functional Materials* **24**, 388–392 (2017).

5. Jain, A. & George, S. J. New directions in supramolecular electronics. *Materials Today* **18**, 206–214 (2015).

6. Embriaco, D., Balagurov, D. B., La Rocca, G. C. & Agranovich, V. M. Topical questions in the photophysics of J aggregates. *Phys. status solidi* **1**, 1429–1438 (2004).

7. Würthner, F., Kaiser, T. E. & Saha-Möller, C. R. J-aggregates: from serendipitous discovery to supramolecular engineering of functional dye materials. *Angew. Chemie - Int. Ed.* **50**, 3376–3410 (2011).

8. Kobayashi, T. J-aggregates. *World Sci.* **17**, 67–94 (1996).

9. Brixner, T., Hildner, R., Köhler, J., Lambert, C. & Würthner, F. Exciton transport in molecular aggregates – from natural antennas to synthetic chromophore systems. *Advanced Energy Materials* **7**, 1700236 (2017).

10. Lova, P. *et al.* All-polymer photonic microcavities doped with perylene bisimide J-aggregates. *Adv. Opt. Mater.* **5**, 1700523 (2017).

11. Cohen, E. *et al.* Robust Aqua Material: A Pressure-Resistant Self-Assembled Membrane for Water Purification. *Chem. Eur. J.* **56**, 2203–2207 (2017).

12. Wang, Q. *et al.* High-water-content mouldable hydrogels by mixing clay and a dendritic molecular binder. *Nature* **463**, 339–343 (2010).

13. Würthner, F. *et al.* Perylene Bisimide Dye Assemblies as Archetype Functional

Supramolecular Materials. *Chem. Rev.* **116**, 962–1052 (2016).

14. Ambrosek, D. *et al.* Photophysical and quantum chemical study on a J-aggregate forming perylene bisimide monomer. *Phys. Chem. Chem. Phys.* **13**, 17649 (2011).

15. Lin, H. *et al.* Collective fluorescence blinking in linear J-aggregates assisted by long-distance exciton migration. *Nano Lett.* **10**, 620–626 (2010).

16. Kieu, K. *et al.* Demonstration of Zeno switching through inverse Raman scattering in an optical fiber. *Opt. Express* **19**, 12532 (2011).

17. Kieu, K. *et al.* All-optical switching based on inverse Raman scattering in liquid-core optical fibers. *Opt. Lett.* **37**, 942–944 (2012).

18. Jung, Y. K. & Park, H. G. Colorimetric detection of clinical DNA samples using an intercalator-conjugated polydiacetylene sensor. *Biosens. Bioelectron.* **72**, 127–132 (2015).

19. Hochstrasser, R. M. & Nyi, C. A. Dynamical effects from resonance Raman and fluorescence studies of the molecular exciton system perylene. *J. Chem. Phys.* **72**, 2591–2600 (1980).

20. Angelella, M., Wang, C. & Tauber, M. J. Resonance Raman spectra of a perylene bis(dicarboximide) chromophore in ground and lowest triplet states. *J. Phys. Chem. A* **117**, 9196–9204 (2013).

CHAPTER 2

Existing knowledge & theory

This chapter is organized in three parts. The first part is a literature review on aggregation aggregation of organic molecules. After a first description on the main properties of J-aggregates, a number of aggregating species are described with a special focus on perylene bisimides (PBIs). The second part deals with conjugated polymer systems and excited state processes that define the properties of these materials, with oligofluorenes as an example system. In the last part of this section we introduce the material identified for the stimulated/inverse Raman technique, i.e. polydiacetylene coupled with metal nanoparticles.

2.1 Aggregates: background, properties, species

Isolated molecules and bulk materials have an intermediate state represented by aggregated systems. The assembling phenomenon can drive the single units to create beautiful supramolecular structures with valuable photophysical properties provided by their conformational asset, which appears to be perfectly systematized and ordered. Understanding this transition from separated molecules/monomers to an organized macrostructure is crucial for exploring the potential of such materials. Aggregates can be found widespread in nature and take part in a wide number of energy or charge transfer processes that occur in living organisms, including photosynthesis.[1] These photobiological patterns became in time a source of inspiration in the quest for versatile building blocks of supramolecular aggregates in the field of condensed matter physics.[2]

The aggregation of dye molecules in solution at higher concentrations is a common phenomenon that has been studied by many authors. The behavior of pseudoisocyanine (PIC), however, differs radically from aggregation of most other dyes. The discovery happened almost 80 years ago by Günter Scheibe et al.[3] and Edwin E. Jelley[4], who independently observed the appearance of a new, very narrow absorption band and a narrow resonance fluorescence band with very little Stokes shift.

More specifically, 1,1′-Diethyl-1,1′-cyanine chloride, pseudoisocyanine (PIC), is a prototypical example of this class of dyes and is also one of the most intensively studied. As

we can observe in **Figure 2-1**, PIC chloride shows in ethanol two broad absorption maxima at around 19000 cm^{-1} and 20500 cm^{-1} (526 and 488 nm respectively), while in water a third sharp absorption maximum appears at 17500 cm^{-1} (571 nm).
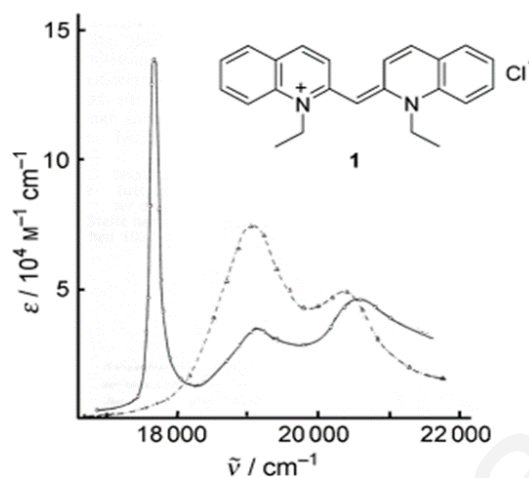
Figure 2-1 PIC molecular structure and absorption spectra in water (solid line) and in ethanol (dashed line).[4]

The intensity of this band further increases by adding sodium chloride in the same way as increasing the dye concentration. Hence, large deviations from the Lambert-Beer law were observed. Scheibe performed comprehensive studies using different dyes, solvents, concentrations and temperatures, concluding in 1937 that the change of the absorption spectrum is due to reversible polymerization of the chromophores, as the spectral changes are reversible upon heating and cooling of the dye solutions and because of self-assembly of monomers into non-covalent bound polymer states.

This phenomenon has been explained in terms of coupling of transition moments of the constituent dye molecules (molecular exciton coupling). Currently, dye aggregates that show by exciton coupling a narrow absorption band shifted to a longer wavelength (bathochromically shifted) compared to the monomer absorption band and a nearly resonant fluorescence with narrow band, together with hyperchromicity and superradiance compared to the monomer, are generally called J-aggregates or Scheibe aggregates.

By contrast, other dyes that show a shift towards the blue (smaller wavelength, hypsochromic shift) compared to the monomer band are termed H-aggregates and exhibit in most cases low or no fluorescence.[6]

Unlike the J-band, the lineshape of the H-band generally shows a rich vibrational structure and has a width of the order of that of the monomer band. Some substances, indeed PIC

itself, exhibit both a J-band and an H-band on aggregation. **Figure 2-2** shows that the molecular planes of monomers (on the left) self-align to form molecular aggregates (on the right). In the aggregates, the single elements can exhibit a range of non-covalent interactions that lead to the alignment of monomers, including $\pi-\pi$ van der Waals associations, as well as Coulombic interactions.
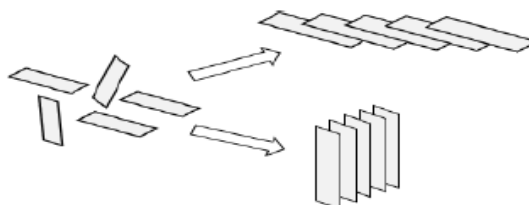
Figure 2-2 Unaligned monomers are represented as distributed structures on the left. Upper right structure is identified with a J-aggregate; the lower right structure is identified with an H-aggregate.[5]

J-aggregates are becoming very attractive due to the intrinsic properties of organic materials that can in principle provide significant advantages when compared with their inorganic counterparts. For example, expanding commercial applications involving wearable sensors and displays are successfully improving in processability (from organic media to flexible films), tuning of optical properties and price. Organic optoelectronics is an area of research that has seen substantial growth during the past decade, thanks to the success of devices such as organic light-emitting diodes (OLEDs), organic field effect transistors (OFETs), and organic photovoltaics (OPVs). In these applications, excitons in the form of π-conjugated luminescent units extend over strongly connected and ordered molecular units, where the packing arrangement of the dyes governs the favored optical outcome.[7] Moreover, supramolecular aggregates are attractive from a spectroscopic point of view, as an external change, i.e., in temperature, gives the chance to tune the desired spectral state of the monomer/aggregate and passes through an apparent isosbestic point where the two forms are present. To develop organic semiconductor technologies, it is necessary to understand the complex processes present in the materials and how these can affect device performance. J-aggregates are currently attracting increasing interest in organic photonics due to the fact that self-assembly of molecules into a head-to-tail arrangement results in coherent π-electron states that are delocalized over part of the molecular aggregate.[8] Hence, J-aggregates are considered as model materials for studying linear and non-linear optical properties of one-

dimensional excitons. Finally, J-aggregates are models for the self-assembled structures, where self-assembly crucially changes their spectral and other functional properties.[9,10, 11]

During the last two to three decades, an enormous number of dye aggregates have been developed and their structural, optical and photophysical properties have been studied intensively. Specifically, J-aggregates from cyanines, porphyrins, synthetic and semisynthetic model compounds of natural light-harvesting pigments (chlorophylls), and functional dyes such as perylene bisimides, have been prepared.[9]

2.1.1 Properties of J-aggregates

J-aggregates disclose a great potential as self-organized dyes due to the collective optical emission that takes place from a large number of coherently coupled molecules. Excitation delocalization leads to an excitonic transition resulting in a narrowing and a shift of the aggregate's absorption spectrum compared to the monomer. In particular, the linewidth of the excitonic J band is estimated to be narrower than the monomer by about the square root of the number of coherently coupled molecules, as reported by some calculations.[12] The greatest importance of these systems resides in the extraordinary optical properties of these aggregates, which are to a large extent governed by exciton delocalization, transport, and relaxation phenomena.

Exciton formation, the superradiance phenomenon, and the effect of excitonic coupling on Resonance Raman scattering will be analyzed in the next sections.

2.1.1.1 Aggregation model

A great number of structural models have been proposed to explain J-aggregate exciton formation and propagation over PIC molecular aggregates. According to one of the most discussed, Kasha exciton theory, J-aggregates are formed when interaction between transition dipoles of two or more chromophores are arranged head-to-tail.[13] In **Figure 2-3** we can see a schematic energy diagram for aggregated dimers with coplanar inclined transition dipoles. The geometry and the slip angle θ are illustrated. Note that for parallel aligned dimers the optical excitation is only allowed from the ground state to one of the two excitonic states depending on the angle θ. For $\theta < 54.7$ the lower energy state is allowed (leading to a bathochromically shifted J-band), while for $\theta > 54.7$ the allowed state is at higher energy (leading to a hypsochromically shifted H-band).
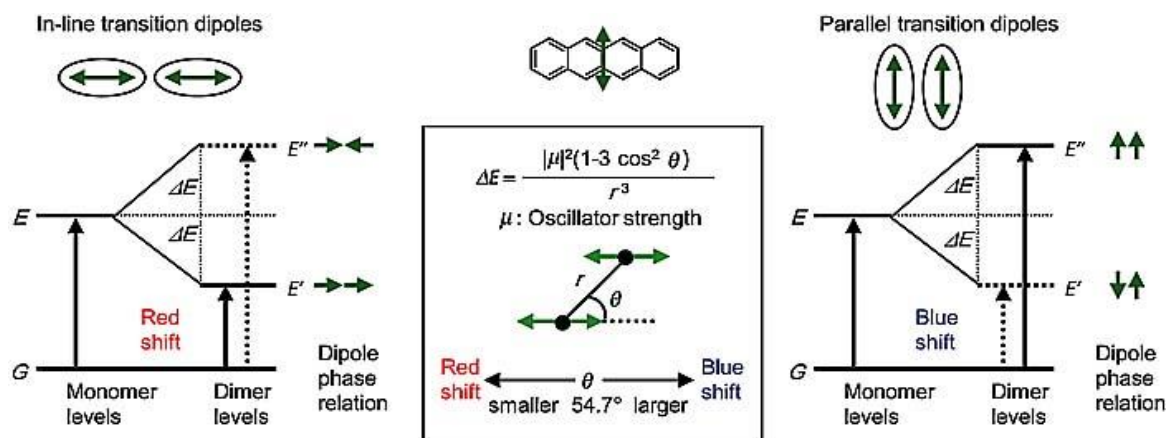
Figure 2-3 Exciton-band energy diagrams for Kasha's dimer model. Green arrows indicate transition dipole moments; the moment of the lowest excitation energy of tetracene is short-axis polarized. Solid and dotted arrows represent allowed and forbidden transitions, respectively.[14]

Although the model of Kasha and co-workers is very instructive for explaining the spectral shifts of dye aggregates, this model has some limitations. In particular, this model seems to overestimate the magnitude of energy shifts and it is not possible to find an exact agreement between experimental data and calculated spectral shifts.[15] Different models were proposed for PIC J-aggregates after Kasha's formulation. Regarding the publications in the current decade, there is still an ongoing discussion on the "true" structure of PIC aggregates. What is generally acceptable is that PIC aggregates self-assemble into extended supramolecular polymers in aqueous solution, and these polymers exhibit exciton migration over macroscopic distances. Even the highly sophisticated instrumental techniques currently available cannot reliably resolve the structural details of the molecular packing in these aggregates, probably because the aggregate structure of PIC dyes strongly depends on the different experimental conditions. Under diverse preparation conditions performed in different laboratories (temperature, pH value, ionic strength, etc.), the individual molecules might reorganize into an alternative packing motif. It is remarkable that observations made almost 70 years ago led to conclusions that are still valid nowadays.[8,16]

In describing the photophysics of polymer assemblies one must treat not only interchain coupling, as is the usual consideration for small molecular aggregates within the Kasha formalism, but also intrachain coupling. In other words, polymer π-stacks are inherently two-dimensional (2D) excitonic systems with electronic excitations delocalized along the polymer chain as well as between chains. Such excitons possess a dual nature; within polymer chains, excitons are of the Wannier-Mott type, where the electron and hole can

readily separate over several repeat units, whereas across chains, excitons are more Frenkel-like as charge separation is less likely and is limited to at most neighboring chains, resulting in the so-called interchain polarons. To account for the H- and J-like photophysical properties exhibited by many emissive conjugated polymers, an HJ-aggregate model has been developed, which accounts for both inter- and intramolecular degrees of freedom. This model considers excitons delocalized both along and across polymer chains within a π-stack and is therefore able to unravel the competitive effects of intrachain (J-favoring) versus interchain (H-favoring) interactions and their impact on the photophysical response.[16]

In a polymer π-stack, typical of the packing present in P3HT and MEH-PPV (the most common emissive polymers) films, there exists competition between the interchain (H-favoring) interactions considered in the H-aggregate model and intrachain (J-favoring) interactions. The ability of one polymer to assume both H- and J-aggregate forms most likely results from differing morphologies. P3HT specifically shows a weaker intrachain bandwidth, compared to other conjugated polymers. Processing in very polar environments can induce signatures of J-like coupling in P3HT and only in the case of sufficiently high molecular weight; for instance, enhanced intrachain coupling (and attenuated interchain coupling) is experienced by the more planar (torsionally less disordered) macromolecules of P3HT of higher molecular weight. When processing P3HT in weakly polar media, as in common organic solvents, the spectroscopic signatures are decidedly H-like and are stable to thermal treatment. P3HT appears different from other polymeric semiconductors in this respect, as H- and J-aggregates can be created by a short-range wavefunction overlap coupling induced by Frenkel/charge-transfer exciton mixing, in cases in which the conventional Coulombic coupling is much smaller by comparison. The sign of the coupling depends on the exact registry between neighboring chains. It may be that in P3HT, the interchain coupling is comparatively higher than in other materials as a result of this phenomenon, and therefore, the H-like signatures are generally observed, save exceptional processing conditions. Generally, understanding the differences in photophysical properties between the different classes of emissive polymers will require more detailed knowledge of the relationship between the various realizations of disorder and the inter- and intrachain exciton bandwidths.[16,17]

2.1.1.2 Excitons

Excitons are electrically neutral quasi-particles that are created when light interacts with matter. Following light excitation, the electrons and holes in insulators and semiconductors

are bound to each other by the electrostatic Coulomb force. It is considered to be an elementary excitation of condensed matter that can transport energy without transporting net electric charge. They have many features analogous to those of atomic hydrogen, like an electron orbiting around a proton. However, it exhibits a lower binding energy because of the small effective masses of the excited electron and hole. When an electron recombines with a positive hole in an exciton, the original atom
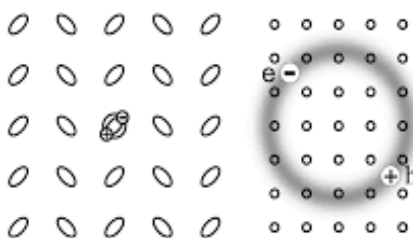
Figure 2-4 Frenkel and Wannier excitons, on left and right respectively. The Frenkel exciton is localized on or around a molecule (site), and the Wannier exciton is more extended.[18]

is restored, and the exciton vanishes. The energy of the exciton may be converted into light when this happens, or it may be transferred to an electron of a neighbouring atom in the material. If the energy is transferred to a neighbouring electron, a new exciton is produced as this electron is forced away from its atom. **Figure 2-4** shows two types of excitons, Frenkel and Wannier, generally differing in radial dimension, binding energy and dielectric constant of the material they belong to. Frenkel excitons are mostly found in organic molecular materials, Mott-Wannier excitons are typical of inorganic semiconductors.[19,20]

The wave function of a molecular exciton can be localized on a single molecule and described as a Frenkel exciton. However, delocalized electronic properties and cooperative phenomena can develop in a molecular solid if strong intermolecular interactions exist. In such cases, the exciton wave function contains a strong charge-transfer component (i.e., Wannier exciton) and is spread over several molecules. All excitons in conjugated polymers can be considered as formed from bound states of conduction band electrons and valence band holes. Instances of strong coupling result in delocalized excited states over two or more chromophores and the quantum-mechanical wave function has a particular pattern of amplitudes across the molecules. Formally, this means that the excitation is in a quantum superposition of the electronically excited states of different molecules or simply, in a state where there is electronic coherence among chromophores. Exciton-vibrational coupling enhances exciton localization due to the wide range of defects normally encountered in

organic materials. Delocalized excited states provide the most evident and widely available signature of quantum coherence in photosynthetic light harvesting. Excitons can extend over multiple chromophores and can have a profound impact on the optical properties of the system as well as on charge and energy transfer dynamics.[21]

A good example of the difference between Frenkel and Wannier models is represented by J-aggregates, where the exciton wave function covers several molecules. Specifically, the coherence number is the number of molecules over which the exciton is delocalized. Electronic coherence depends on the strength of the electronic coupling between chromophores. Quantum coherence between electronically excited states of donors and acceptors may give rise to an evolution of excitations, which in J-aggregates, thanks to their strong delocalization, can give rise to exceptional enhancements of energy transfer rates.[10] For example, based on the concentration dependence of the absorption spectra of PIC (see **Figure 2-1**), it is possible to state that the minimum number of molecules required to yield the characteristic spectral properties of the J-aggregate is 4.[22] This number represents, in essence, the exciton size, describing the relative motion of the electron and the hole. This relatively large exciton size is unusual among organic systems, since most of the excitons in molecular systems are of the Frenkel type and are localized on a single molecule. Because of the strong intermolecular interaction, the exciton is also coherently delocalized throughout the aggregate. This ultrafast coherent motion averages out the local inhomogeneities which also explains the unusual sharpness ($\sim$150-200 cm^{-1}) of the J band at room temperature. Both the large exciton size and the ultrafast coherent motion are important to understand the optical nonlinearity of J-aggregates.[23]

2.1.1.3 Superradiance

One of the most interesting optical properties of dipolar coupled molecular assemblies is their enhanced rate of collective spontaneous emission compared to that of the monomer. This effect, which is due to the coherent nature of the excited states on the aggregate (see **Figure 2-5**) is known as superradiance. Superradiance is an effect which can convert disordered energy of various kinds into coherent electromagnetic energy. For a linear chain, the enhancement factor, i.e., the number of molecules over which the optical excitation is delocalized, gives an idea of the extent of this superradiance phenomenon (e.g., for PIC dye, this is about 100 at low temperature).[24]
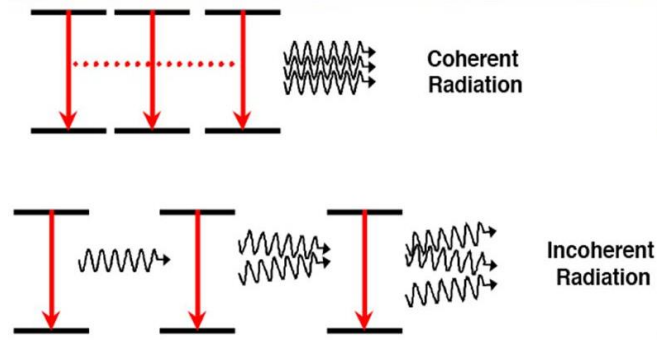
Figure 2-5 Coherent versus incoherent radiation on photon emission.[25]

This kind of emission was discovered in 1954 by Robert H. Dicke and has characteristic properties that make it different from other more common phenomena like luminescence. Indeed, by using the same words of Dicke: "a gas which is radiating strongly because of coherence will be called 'superradiant'. If the wavelength of the light is much greater than the separation of the emitters, then the emitters interact with the light in a collective and coherent fashion. This causes the group to emit light as a high intensity pulse (with rate $\propto$ N^2). This is a surprising result, drastically different from the expected exponential decay (with rate $\propto$ N) of a group of independent atoms, as in spontaneous emission. The effect has been used to produce a superradiant laser.[26] In this new type of laser, light is emitted collectively by several atoms at the same time and has the potential to be up to 1000 times more stable than the best conventional visible lasers. In **Figure 2-6** a standard laser is represented: when a photon interacts with an atom or molecule, an exact copy of the photon
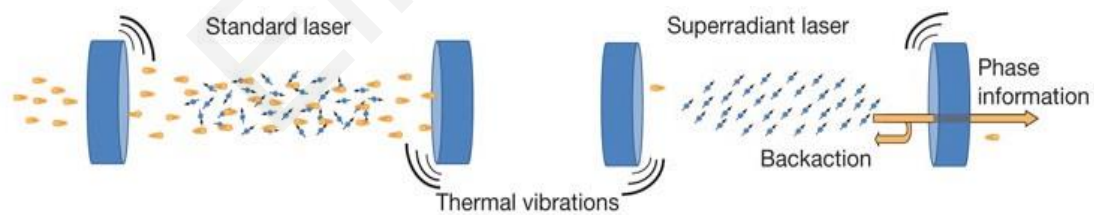
Figure 2-6 Standard vs superradiant laser. In the standard laser, photons (in yellow) circulate inside the cavity, extracting energy from the largely incoherent atomic gain medium (in blue). In the superradiant laser, the phase of atomic dipole is weakly affected by thermal mirror motion.[26]

is produced and these two photons can go on and generate four photons, and so on. If one of the mirrors is thin enough to allow some of the light to pass through it, a coherent beam of identical photons will exit the cavity to make the laser beam. The laser frequency oscillates because the atoms stick around between the mirrors causing the mirrors to vibrate or because

of environmental disturbances. In a superradiant laser instead, this is not happening because almost all photons escape from the cavity before they could be scrambled by the mirrors: indeed the atoms are constantly energizing and emitting synchronized photons. In order to store phase coherence, the laser beam, rather than relying on mere photon generation it depends on collective effects happening in an atomic medium. Such a laser system, thanks to the superradiant effect provided by coherently aligned atomic dipoles to sustain a synchronized emission of light, can have a substantially narrower linewidth than a conventional laser. JILA/NIST physicist James Thompson engineered a system called "phased arrays" in which electromagnetic waves from many radio antennas are carefully synchronized to make a really good directional antenna. The system works by trapping the atoms between two mirrors and then uses low-power lasers to tune the rate at which the atoms switch back and forth between two energy levels, thus aligning the dipoles among them. This phasing system resembles the supramolecular structural order and the outstanding related features conveyed by J aggregates.[26]

Considering the luminescence decay time of J-aggregates, this is shorter than that of the corresponding monomer. The amount of the decrease depends on the degree of chain regularity of the aggregate. The degree of disorder dictates also the radius of the excitonic state, which determines the enhancement of the decay rate (superradiance). The correspondence between the degree of disorder and the shortening of the luminescence decay time, which can be measured experimentally and used for structural diagnostics of J-aggregates, is important for all aspects of the study and applications of J-aggregates.

2.1.1.4 Electroluminescence

Electroluminescence is an optical and electrical phenomenon in which a material emits light in response to the passage of an electric current or to a strong electric field. Electroluminescence is the result of radiative recombination of electrons and holes in a material. The excited electrons release their energy as photons.

For every electroluminescent material the appearance of crystallization, or aggregation or even domains of high orientational order, are completely undesirable because they act as traps for optical excitations and they quench luminescence due to close packing of the aromatic π-electron systems. However, among other conjugated organic materials, J-aggregates have a really prominent advantage. Thanks to their strong and bright fluorescence emission, they are highly desirable as emitting carriers in thin films to be used for the fabrication of light-emitting devices. J-aggregate electroluminescence in dye-doped polymer

layers is clearly observed by light emission in the visible range dependent on the redox potentials of the dyes used.[27] A problem in building up the films could be different pH and temperature requirements affecting adsorption and stability of the aggregates.
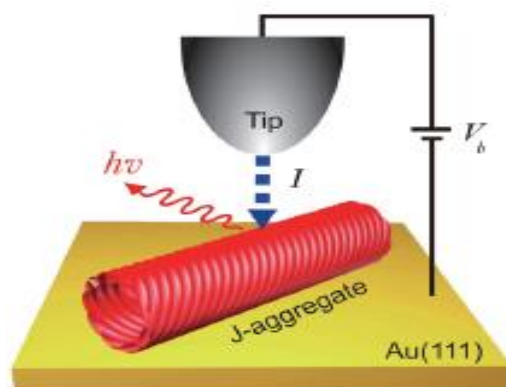
Figure 2-7 STM Technique: shematic of the tip-J-aggregate-substrate junction.[28]

J aggregates can show electroluminescence in different conditions. One of these, is by tunneling electron excitations in an ultrahigh-vacuum scanning tunneling microscope (STM): electroluminescence behavior arises in the material (in this case, a porphyrin J-aggregate). As shown in **Figure 2-7**, high-resolution STM images suggest a spiral tubular structure for the porphyrin J-aggregates on Au(111), which appear with highly ordered "brickwork"-like arrangements.[28] There is an "onset" voltage that gives rise to J-aggregate electroluminescence and it appears to be related to the energy level alignment of frontier molecular orbitals (HOMO and LUMO) at the tunnel junction. Electroluminescence shown by the STM technique provides information on J-aggregate structure and excitation mechanism.

2.1.1.5 Aggregation-enhanced Raman scattering (AERS)

Often researchers exploit Raman scattering for its intrinsic high resolution structural information content, to gain positional or reaction pathways to monitor a process. However, sometimes, they explain results with concepts that appear inappropriate for systems involving aggregated molecules.

D. Akins in 1986 advanced a theoretical formulation that aides in interpreting Raman spectra and band intensities for such aggregated elements, and termed it 'aggregation-enhanced Raman scattering' (AERS).[29] Aggregation among molecules may result in enhanced polarizability for the supramolecular assembly, which can then couple more strongly to radiation than in the case of a molecule alone. Upon excitation, the aggregate can support

the formation of molecular excitonic states which results in enhanced band intensities compared to those of the isolated monomer. Molecular exciton theory is the basis of this statement.

The vibrational Raman spectrum of an aggregate species is found to have vibrational band intensities (associated with ground electronic state vibrations of the monomer) that are enhanced when compared to those of the non-aggregated monomer. Indeed, this enhancement is observed in the intensity of low frequency modes upon aggregation of the dye that are related to out-of-plane motions.[30] This may be attributed to AERS, as the enhancement of a Raman-active mode increases with an increasing number of interacting molecules. In fact, enhancement of Raman modes which are relevant to assembly (the low frequency modes) are observed to occur only when the excitation wavelength is resonant
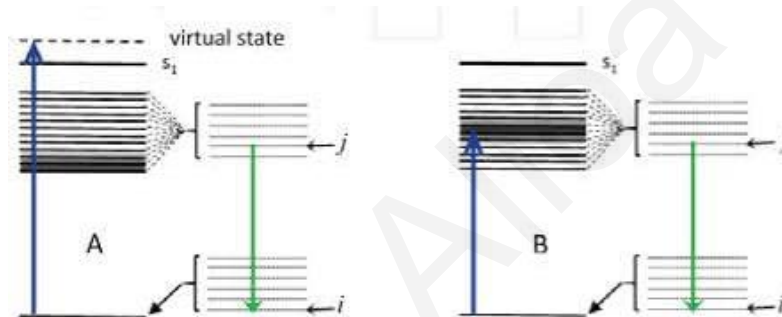
Figure 2-8 (A) Non-resonance and (B) Resonance (the incident exciton overlaps a small number of exciton bands) Raman scattering. The shaded region represents vibro-excitonic bands that are excited when radiation ('blue' transition) impacts on the aggregate system. The 'green' transition corresponds to vibronic scattering. The S1 level corresponds to the monomer absorption band.[5]

with the excitonic transition J-band absorption.[29] The dramatic enhancement of the low frequency modes may be due to exciton-phonon coupling as Raman bands can be associated with lattice motions in the aggregate formation direction, rather than to the effective coherence, as it was stated in previous works.[31]

A pictorial representation of the energy-level diagram for Raman scattering by a J-aggregate system (with a band energy lower than the monomer's energy level) is shown in **Figure 2-8**.
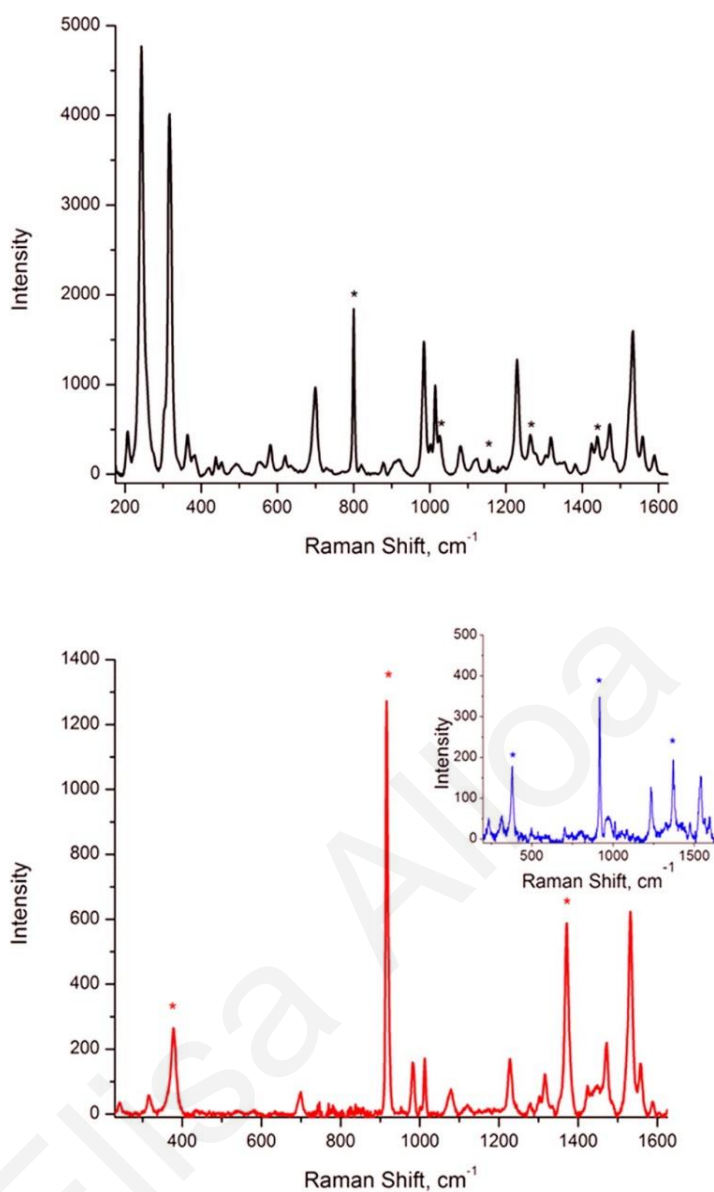
Figure 2-9 Resonance Raman spectrum of aggregates prepared from 50 μM TSPP in 0.75 M HCl (with cyclohexane as the intensity standard), excited with 488 nm wavelength light (black) and 514.5 nm wavelength light (red). The inset shows the resonance Raman spectrum of the 50 μM TSPP diacid monomer in 0.001 M HCl (with acetonitrile as the intensity standard), excited with 454.5 nm excitation wavelength (blue). Asterisks mark solvent Raman bands.[31]

In this illustration which considers AERS, the incident radiation energy is shown to be out of resonance (A) and in resonance (B) with the exciton state. S1 represents the excited state of the isolated monomer (which technically does not exist once the monomer is incorporated into the aggregate). The excited aggregate state is represented as a band composed of

supramolecular levels derived from intermolecular coupling between the N monomers of the aggregate, resulting - in general - in the formation of N levels.

An example is given in **Figure 2-9**, which shows Resonance Raman scattering spectra of porphyrin nanotubular aggregates of meso-tetra (sulfonatophenyl) porphyrin (TSPP). The image shows the background subtracted ensemble resonance Raman spectra of TSPP aggregates in aqueous solution with 0.75 M HCl, excited at 488 nm (black), which is resonant with the sharp J-band of the aggregate, and at 514.5 nm (red), which is 930 cm^{-1} to the red of the absorption maximum of the J-band. The inset shows the resonance Raman spectrum of the diacid monomer excited at 454.5 nm (blue), which is 1039 cm^{-1} to the red of the 434 nm absorption maximum. The Raman intensities of the low-frequency modes of the aggregate are dramatically enhanced, by nearly 3 orders of magnitude, when the excitation wavelength is close to the absorption maximum.

2.1.2 Types of J-aggregates

In this section, an overview on the broad variety of J-aggregate dyes will be provided. Cyanines, merocyanines and squaraine dyes as well as porpyirins, phthalocyanins and chlorophyll dyes will be considered, with general remarks on their most important properties. We will focus then on perylene bisimides in *Chapter 2.1.3* that were exploited using supramolecular formation principles, and considering their optical and photophysical properties, as well as their potential applications.

2.1.2.1 Cyanine dyes

Cyanine dyes were discovered much earlier than J-aggregates. They started being used to convey light sensitivity to silver halide in a region of the spectrum where it is generally unresponsive. However only when J-aggregates had become recognized materials, this class of chromophores gained their fame as well. Despite the fact that many cyanine dyes are known to form J-aggregates, the most relevant one is unquestionably pseudoisocyanine (PIC).
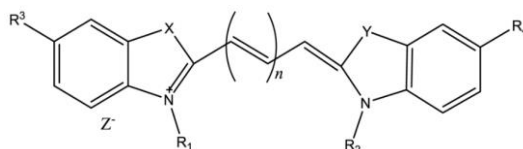
Figure 2-10 General structure of cyanine dyes. Their properties can be tuned by the appropriate choice of heterocyclic nuclei (X and Y), by the length of the polymethine chain (n), and also by varying the groups R1–R4 for instance, in order to achieve the desired solubility.[32]

Two heterocyclic units (X and Y, each with different substituents in various positions, as shown in **Figure 2-10)** constitute the generic cyanine dyes. The color of these dyes is mainly determined by the length of the conjugated polymethine chain $(CH)_n$, where n=1, 3, 5, 7,..

The general schematic structure of cyanine chromophores looks like a planar cation:
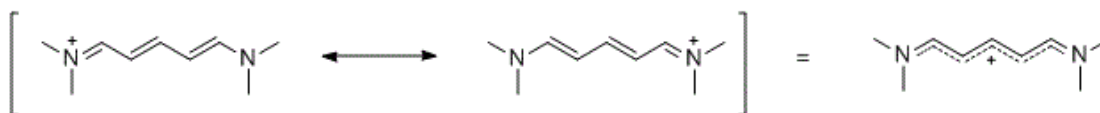
The positive charge on these molecules attracts different anions, for instance I⁻ (iodide). This is relevant because their aggregation happens, as it is for amphiphilic dyes, by a self-assembling of hydrophobic and hydrophilic substituents, whose spectra are usually characterized by both H- and J-bands, e.g., two-dimensional J-aggregates with a herringbone-type packing like a nanotube with a double-walled structure, similar to a lipid bilayer, with the hydrophobic chains at the interior of the bilayer.[33] The position of the π-π* absorption band is affected by the carbon chain length between the nitrogen atoms and does not seem particularly dependent on the end groups attached to the nitrogen atoms. The π electrons are delocalized over the length of the carbon chain between the nitrogen atoms, thus the structure of cyanine dyes is adjusted appropriately to attain better aggregation and associated optical properties, e.g., longer molecules absorb at lower energies and show bigger absorption coefficients.

The positively charged nature of cyanine molecules influences their solubility in water and consequently their applications. At the same time, this cationic character can also be a limitation for the application of cyanine dyes in other fields of high technological relevance, where J-aggregates of neutral molecules, with their exceptional exciton transport properties, are required.

2.1.2.2 Merocyanine and squaraine dyes

Merocyanines can play a major role in the growing arena of organic photovoltaics. They structurally look similar to cyanine dyes and, as such, they share with them corresponding properties. Indeed both of these classes of molecules contain linear and highly polarizable polymethine chains, however, merocyanines are not ionic. An example is dispayed in **Figure 2-11** (left image).

Merocyanines are characterized by two components, an electron donor and an acceptor, connected by a system of double bonds which transfer the electron conjugation. A resonance

between a charged and uncharged forms characterizes the ground state of such a system. A zwitterionic character can be also attained in polar solvents (see right image in **Figure 2-11**), because of an increase in aromaticity acquired throughout the charge separation.

Despite the fact that the majority of cyanine dyes form J-aggregates in solution or in silver halide emulsions, only few merocyanine J-aggregates in solution have been reported,
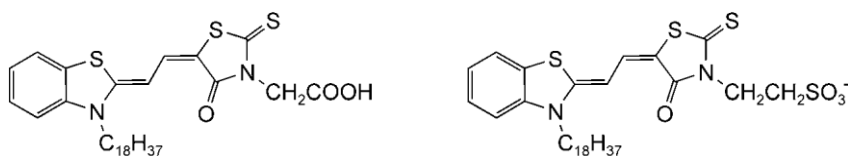
Figure 2-11 Structures of J-aggregate-forming merocyanine dyes reported by Mizutani et al. (left) and Balli and co-workers (right).[9]

probably because highly polarized merocyanines usually form sandwich H-type dimers. Infrequently, a weak J-band and fluorescence have been detected and ascribed to a displacement of two dyes in the dimers. Electrostatic interactions hold these face-to-face-stacked dimers together exhibiting the highest binding energies so far. In the solid state, functionalization of the electron-donor component with bulky substituents can induce displacement of the monomers into a slipped stacking arrangement typical of J-aggregates. In solution, few merocyanines with J-type aggregation behavior were reported in the 1980s.[9] In particular, Mizutani *et al.* observed J-type aggregation of the merocyanine chromophore displayed on the left of **Figure 2-11**, molecule bearing a long alkyl chain in methanolic aqueous solutions containing KOH and nonionic surfactant Triton X-100.

The merocyanine on the right of **Figure 2-11** bearing a sulfonate group and similar derivatives with different alkyl chain lengths and other counterions were investigated by Balli et al., and they noticed that these merocyanines form J-aggregates in water or in a mixed DMSO/water solution without adding any salt.[9] Besides that, a bathochromically shifted absorption band, typical of J aggregates, was observed when similar merocyanines in water were mixed with starch.

2.1.2.3 Chlorophyll dyes and their derivatives

Chlorophylls and their derivatives are the main chromophores in natural light-harvesting systems. They are derivatives of tetrapyrrole macrocycle porphyrin, as shown in **Figure 2-12**. Natural pigments are constructed from a chlorin derivative skeleton base bearing an extra 5-membered ring with a keto function; a magnesium metal ion is coordinated to the
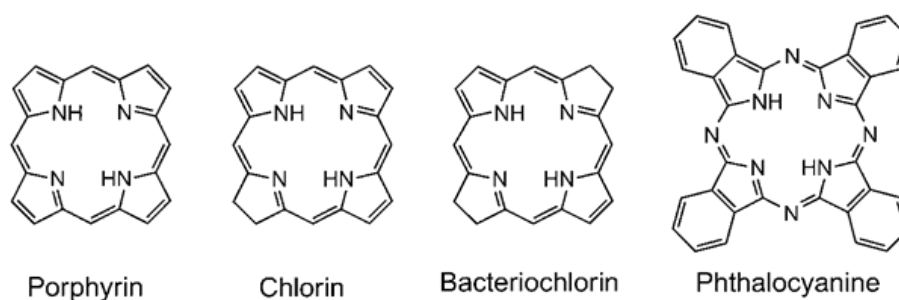
Figure 2-12 Structures of porphyrin and its derivatives; when one/two pyrrole double bonds, respectively, are reduced the derivative is named chlorin/ bacteriochlorin. The structure of the most relevant tetraazaporphyrin derivative, called phthalocyanine, is also illustrated.[9]

pyrrole nitrogen atoms. The chemical structures of these light-harvesting chlorophylls and bacteriochlorophylls are shown in **Figure 2-13**. The main structures of chlorophylls (Chls) and bacteriochlorophylls (BChls) shown are based on a chlorin or bacteriochlorin structure (to be noted: the term "bacteriochlorophyll" for BChls c,
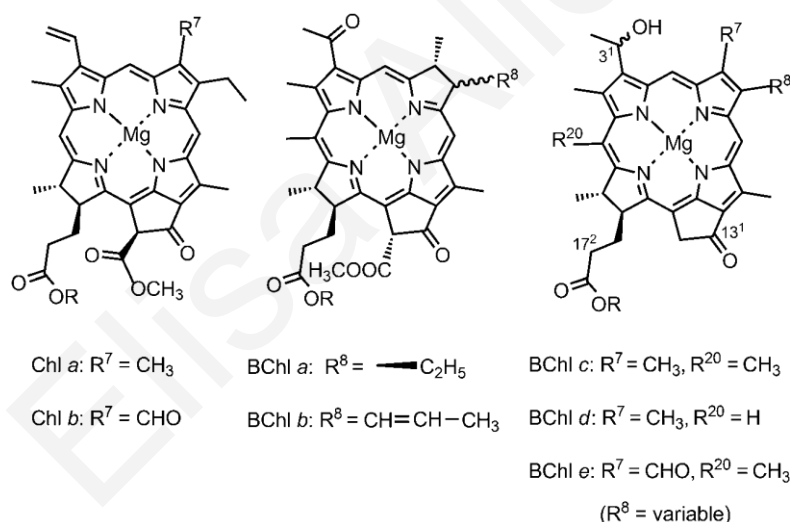
Figure 2-13 Natural chlorophylls and bacteriochlorophylls. The substituent R in the chlorophylls is a phytyl group, while in the bacteriochlorophylls it is variable (for instance, phytyl, farnesyl, or stearyl group). R8 in BChls can be a methyl, ethyl, propyl, isobutyl, or neopentyl group (c–e).[9]

d, and e is rather ambiguous, as these BChls contain a chlorin structure instead of a bacteriochlorin). However, the trivial name was assigned prior to the elucidation of their chemical structures, because of their natural occurrence in bacteria.[9,34]

Chlorophyll dyes bear a porphyrin core structure, with one or two double bonds of tetrapyrrole rings reduced. Inspired by the appealing beauty and key properties of such

natural cyclic dyes in the photosynthetic system, a multitude of artificial cyclic chromophores based on porphyrin dyes, have been created during the last decades to mimic the efficient features of the natural archetypes.

Phthalocyanines share a similar structure with porphyrin dyes. They naturally self-assemble as sandwiched face-to-face H-aggregates in solution because of their large overlapping π surfaces rather than more slipped arrangements required for J-type exciton coupling. Hence, only a few phthalocyanine J-aggregates have been reported, usually with the complexation of a metal ion to assist the head-to-face aggregate formation.[35]
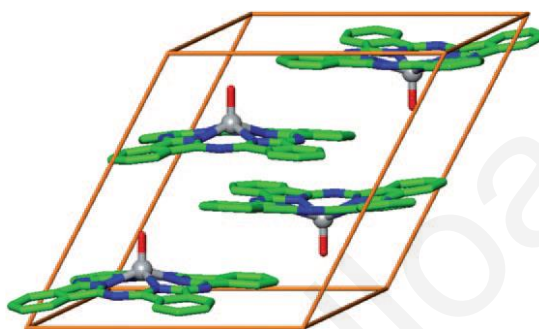
Figure 2-14 Packing of TiOPc photoconductors in the Y-polymorph of the charge-generating layers of xerographic photoreceptors in the solid-state. Colors legend: green C, blue N, red O, gray Ti.[9]

The main application of phthalocyanine chromophores as functional pigments exploits phthalocyanines with slipped π–π stacking arrangements showing bathochromically shifted J-bands. In particular, among the various metal complexes, the blue copper one of phthalocyanines is the most relevant for mass production. Their packing arrangements in the solid state determines the color of the pigment. Another phthalocyanine pigment, titanylphthalocyanine (TiOPc), is the most employed photoconductor for laser printers. For this application, J-type excitonic coupling guarantees the most efficient transfer of excitons to the interface. The Ti=O complex displayed in gray and red in **Figure 2-14** is responsible in the solid state for the displacement of the chromophores, as confirmed by many other polymorphs of TiOPc. A band broadening (suggesting also an H packing) together with a bathochromic shift of the initially very narrow absorption peak of these TiOPc photoconductors in solution at around 700 nm enabled the commercial application of the polymorph Y-TiOPc in the solid-state (the absorption band appears enlarged from 600 to 900 nm with a maximum at around 800 nm). Remarkable aspect is that this structural arrangement of the dyes and its subsequent effect on the absorption spectra are similar

aspects found in chlorophyll pigments of purple and green bacterial light-harvesting systems. However, the structural specifics of these natural light harvesting systems were yet undiscovered when those molecules were developed.[9,36]

2.1.3 In-depth: perylene bisimides (PBIs)

2.1.3.1 Applications and derivatives

PBIs have been well recognized as versatile chromophores with strong absorption, near unity fluorescence quantum yield, and high thermal and photochemical stability.[37] Their high chemical flexibility allows various substitutions thereby tuning reactivity and spectral properties.[38] Their unique properties are primarily derived from their large extended π-systems, which through a π-π stacking interaction lead to a variety of intermolecular p-orbital overlaps for the different derivatives. Due to these appealing assets, perylene bisimides and their related derivatives have continuously received significant attention for their potential applications in biomedicine (bioimaging)[39] and molecular optoelectronic devices, such as organic photovoltaics (e.g. as acceptors),[40,41] field-effect transistors,[42] light-emitting diodes,[43] light-harvesting arrays[44] and LCD color filters.[45] More specifically, their high electron mobilities and affinities and variety of functional forms with different substituents have led to their extensive use as electronic materials, among which perylene bisimides are the best n-type semiconductors obtainable to date. This n-type semiconductivity is associated to the high electron affinity of PBI dyes. In addition, based on their unique combination of redox and optical properties, perylene bisimide dyes have already been studied for decades in electrophotography. Moreover, similarly to cyanines, a major application of PBI chromophores is as high-quality color pigments with tonalities ranging from red to orange, violet, brown and even black; this behavior is again attributable to the arrangement of the molecules in the crystal and thus to the resulting excitonic coupling.[46] Last but not least, robust organogelators that are able to gelate a broad variety of media (e.g., solvents, liquid crystals, etc.) and exhibit outstanding functional properties can be also coming from PBIs. Indeed, in the last years, such adaptable organogelators have been derived from several absorbing dyes and semiconducting π-systems, comprising porphyrins, cyanines, and oligothiophenes. On the contrary, for their n-type counterparts, no organogelators have been achieved to date capable to gelate a range of different solvents. PBI based organogelators seem to be the most favorable candidates for this purpose due to their unequalled combination of absorption, photoluminescence and exceptional semiconducting properties (n-type). Moreover, perylene bisimides show a high processability and an excellent ability to self-organize via liquid crystalline phases. Indeed, liquid crystals possess the spontaneous

capability to form highly ordered structures. Due to the spontaneous ordering capability of the PBI molecules in the liquid crystalline phase, highly ordered films can also be manufactured.[45]

By considering the specific dye derivatives analyzed in this work, they were specially created according to supramolecular principles to self-assemble via π-π stacking and hydrogen bonding into one-dimensional brickwork-type J aggregates, capable in turn to self-organize into columnar liquid crystals. Furthermore, the elaboration of water-soluble PBI-based aggregate systems via self-assembly evolved as a promising research avenue because of its possible exploitation in biological systems. In the most recent research of Würthner's group, PBI J-aggregates could be formed by hydrogen-bonded self-assembly in water, which was quite surprising if we consider that water is a very competitive solvent for the self-complementary hydrogen bonding between the imide units of the PBIs.[47] Interestingly, however, these hydrogen-bonded self-assembled nanofibers with J-type coupling and fluorescence properties only occurred at elevated temperature, obviously driven by entropy from the less ordered PBI room temperature hydrogel material.

More generally, the electronic characteristics of perylene bisimide can also be finely tuned by the substitution of the conjugated aromatic core. Based on these principles, many perylene bisimide derivatives with either electron-withdrawing or electron-donating groups have been reported in the literature, including cyano-, nitro-, perfluoroalkyl-, aryl-, ferrocenyl-, boryl-, alkyl-, hydroxy-, alkoxy-, amino-, and alkylamino-substituted.[48]

2.1.3.2 Structure and Properties

The physical phase of the perylene bisimide may influence its own supramolecular structure. In the solid state indeed no fluorescence is naturally observed as the packing arrangement of the dyes is mainly of H-type character. In contrast, excellent fluorescence properties appear in solution, where, indeed, perylene bisimides exhibit both H- and J-type excitonic coupling. The absence of bay substituents causes columnar stacks aggregates, whose main absorption band is hypsochromically-shifted (to higher frequencies), indicating predominant H-aggregate formation. Nonetheless, as a result of a displacement between neighboring molecules, a second absorption band bathochromically shifted (at lower energies) becomes allowed too.

The specific arrangement and the connected photophysical properties of the aggregates are strongly dependent on substituents at imide and bay positions. Aggregates with aryloxy

substituents in the bay positions and alkoxyphenyl substituents on the imide atoms (**Figure 2-15**) exhibit predominant J-type character. Increasing the number of aryloxy substituents in the bay positions of the PBI core leads to a bathochromic shift in the UV absorption peak, which also broadens. Although this red-shift indicates the presence of slipped dyes, the
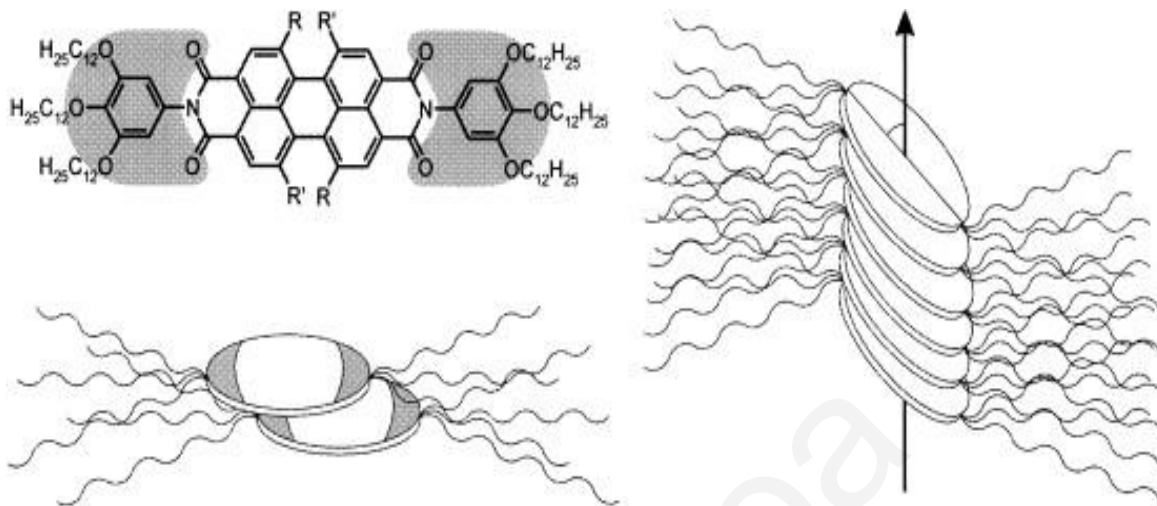
Figure 2-15 Model of the perylene bisimide columnar arrangement based on polar interactions between the dyes and steric repulsion of the substituents at bay positions which lead to a longitudinal offset. Negative electrostatic areas appear in gray.[49]

broadness of the absorption band might indicate a less ideal system predisposed to disorder due to the bulky phenoxy substituents. These ones cause a twisting of the subunits in the PBI core by different degrees depending on the bulkiness of the substituents. The subsequent loss of planarity and rigidity of the PBI molecules induces substantial spectral broadening. The calculated distance between the cores varies with the steric interaction of the aryloxy substituents in the bay positions in the range 3.7-5 Å, with the substituents of the stacked molecules interacting among them. Considering the longitudinal axis, a 35° - 45° inclination of the dyes is expected, as **Figure 2-15**.

By substituting hydrogen atoms to alkoxyphenyl groups at the imide N positions it is possible to have PBI derivatives which form J-aggregates with very specific optical properties, analogous to those of the typical cyanine J-aggregates. As such these dyes exemplify the first perylene bisimide derivatives with a J-aggregate behavior fully achieved (shown in **Figure 2-16**). In comparison, only a slight bathochromic shift was observed in the UV/Vis spectrum of a *N*-butyl-substituted reference (whose imide units cannot undergo hydrogen bonding) upon aggregation in methylcyclohexane at room temperature. This small

bathochromic shift of the absorption band can be attributed to the formation of a dimeric aggregate species.[41]
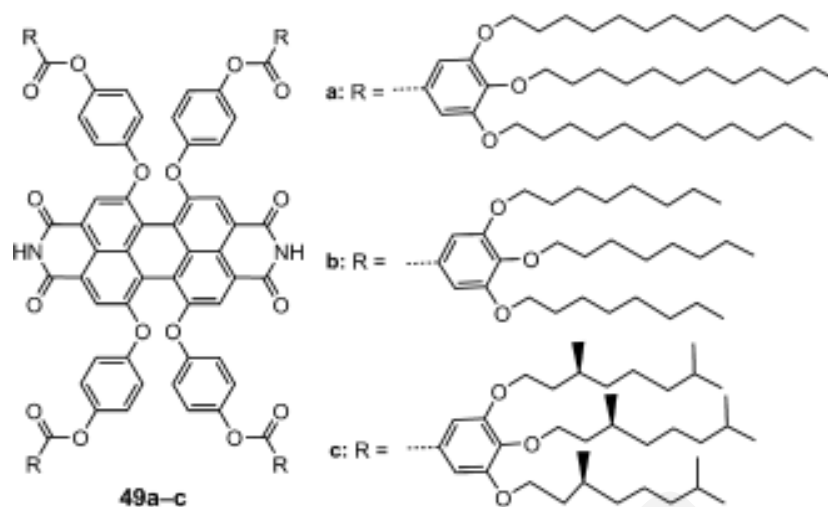
Figure 2-16 Structures of perylene bisimide dyes.[9]

Considering a supramolecular structure of perylene bisimides with both H- and J-aggregate behavior, hydrogen-bond donors/acceptors and π–π interaction were employed for the design of these functional PBI chromophores with such unique spectroscopic properties: these forces collaborate in a self-complementary way to build a supramolecular connection among the monomers in order to achieve a wired structure with a face-to-face arrangement, typical of a mixed J/H aggregate.[16] A possible model for J aggregation of hydrogen substituted imide molecules is depicted in **Figure 2-17**. Investigations on these dyes revealed the formation of elongating π–π stacked dimeric units (**Figure 2-17 c**), successively elongated into double/triple stranded aggregates represented like string cables (**Figure 2-17 d**), where their building blocks are aligned with translational offset (**Figure 2-17 e**).[41,50] The nucleation–elongation mechanism (appearing in **Figure 2-17 c)** was accomplished by applying the nucleation–elongation model to concentration dependent absorption studies, where the equilibrium constants for dimerization are nucleation $K_2 = (13\pm11)$ M^{-1} and elongation, $K = (2.3\pm0.1) \times 10^6$ M^{-1}.

The water-soluble PBI previously reported by Würthner et al., depending on the excitonic coupling extent, forms an aggregate structure with a monomer-like UV/Vis spectrum at room temperature, where the units exhibit a cofacial arrangement with weak H-type coupling, or a slipped packing with J-type coupling when the temperature increases, with fluorescence in the far-red.[47]
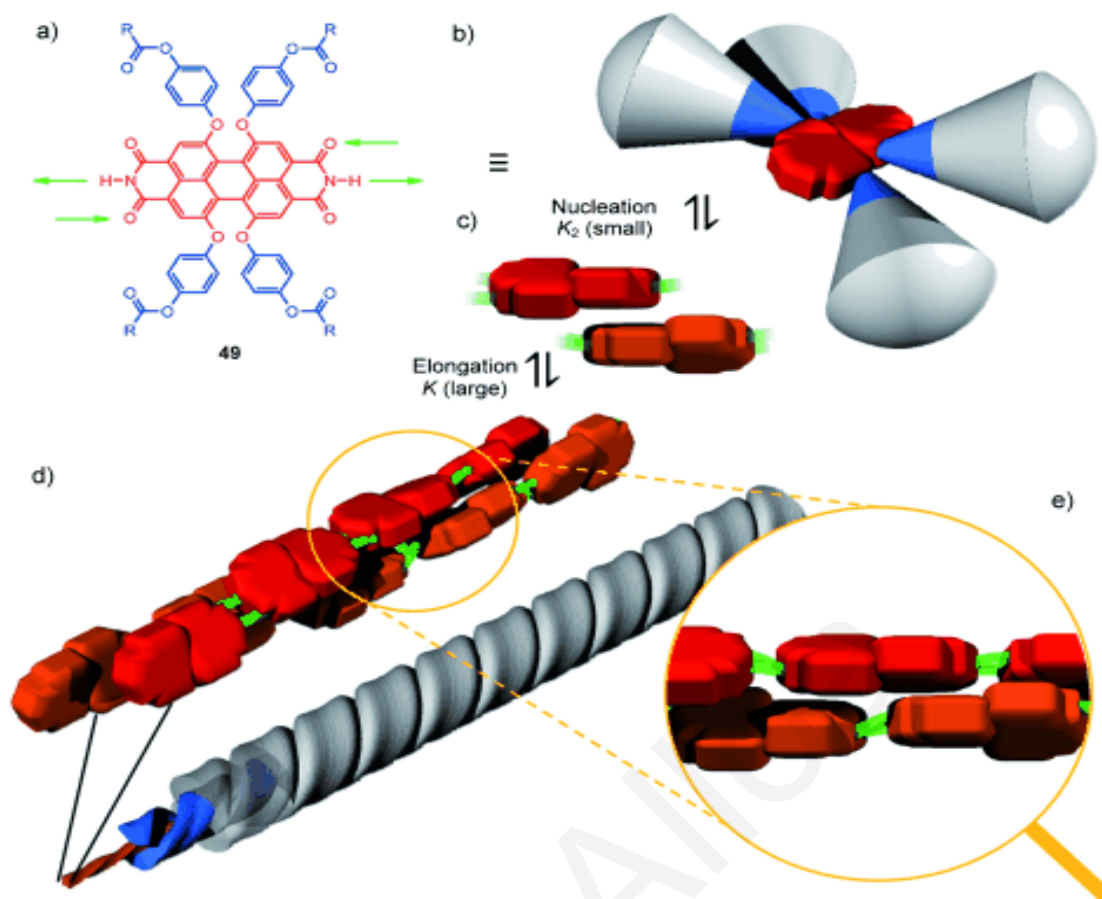
Figure 2-17 Schematic illustration of the self-assembly of the hydrogen substituted imide perylene bisimide dyes into J aggregates. a) Structure and b) image of the monomer. c) Schematic representation of the π-stacked dimeric nucleus and d) that of an extended hydrogen-bonded J-aggregate. Red twisted blocks represent the PBI cores ehile gray cones with a blue apex represent the bay substituents, and green lines represent hydrogen bonds. The dyes self-assemble in a helical fashion, as shown e) The magnification shows the J-type arrangement of the perylene bisimide core units in a double-string cable.[41]

It is very interesting that the H- or J-type aggregation model of perylene bisimide molecules could be altered by a subtle variation of the peripheral substituents. **Figure 2-18** displays a broad series of structurally related PBIs, which have been investigated to explore in detail the effects of peripheral alkyl chains and thus the resulting high steric demand. Those molecules bear three long alkyl chains at the aromatic imide substituents at the periphery. It appeared that PBI-1, PBI-2, and PBI-6 form H-aggregates, whereas PBI-3 and PBI-4 form J-aggregates, and PBI-7 forms mixtures of H- and J-aggregates. On the other hand, PBI-5 does not form any type of aggregate in the investigated concentration range.
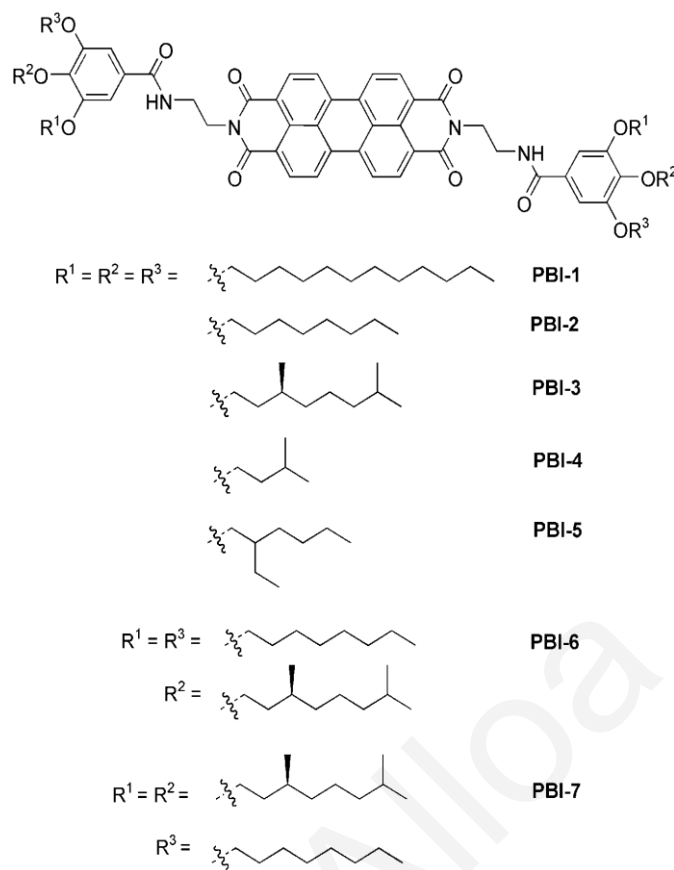
Figure 2-18 Perylene bisimide derivatives containing peripheral substituents with linear alkyl side chains.[50]

Simplified packing models suggested for the J- and H-type assemblies of these perylene shown in are illustrated in **Figure 2-19**. The transition from H- to J-type aggregate may be originated from a simple rotation around the N_{amide} bond, by retaining the π–π stacking and hydrogen-bonding interaction among the amide functionality, as the right side of **Figure 2-19** depicts. However, it was unclear how very subtle changes in the alkyl side chains could define the predilection for one of these π-stacking modes. Comparison of the self-assembly of PBI-3 and PBI-4 (both of them form J-aggregate) confirm that the bulkiness of the methyl groups in the γ position of the peripheral side chains destabilizes the sandwish packed H-type π stacking and favors the J-type one, in which the chromophores are packed with substantial longitudinal displacement. PBI-1 and PBI-2 having linear alkyl substituents prefer to self-assemble as more compact H-aggregates, as it is also for PBI-6, having only one branched chain among the three alkyl substituents at each imide position. PBI-3 and PBI-4, both of which contain three bulky substituents, prefer to self-assemble as J-aggregates

in which the dyes are packed with comparatively bigger space as shown in **Figure 2-19** (middle). PBI-7 has one linear and two branched substituents: neither of those types of
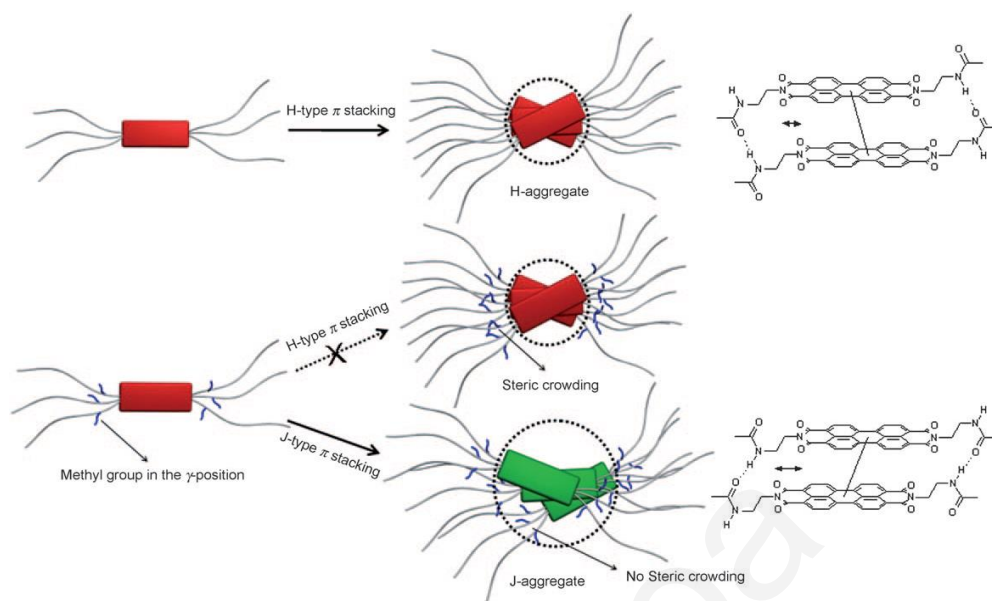
Figure 2-19 Left: Representation of perylene bisimide chromophores with linear (top) and branched (bottom) alkyl substituents. Middle: The transition from H- (top) to J-type (bottom) π stacking with increasing steric demand of the peripheral alkyl side chains. **Right:** Proposed packing model for H- (top) and J-type (bottom) π stacking. In both cases, additional rotational offsets are needed to enable both close π–π contact and hydrogen bonding.[11]

packing arrangement is favored. Notably, for this compound, aggregation required the highest amount of methylcyclohexane in the methylcyclohexane/carbon tetrachloride mixture and the lowest temperature, while no gelation of any tested organic solvents could be observed. For PBI-5, the presence of larger groups at the nearer β position constrains the formation of any π stacking.

Therefore it was found that, depending on the nature of the alkyl substituents, the π-stacking mode of the chromophores can be adapted from usually seen H type to the rather infrequent

4a: R = CH₃; **4b**: R = H
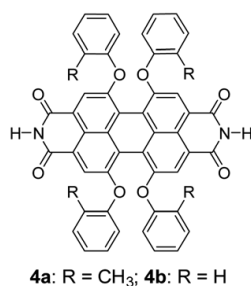
Figure 2-20 Perylene Bisimide organogelator molecule.[9]

J type. Steric effects in the peripheral substituents decree the self-assembly model. PBIs with linear alkyl chain (low steric interaction) formed H-aggregates, while chromophores with branched alkyl groups (higher steric demand) formed J-aggregates, or no aggregates at all.[50]

Another interesting investigation displays a perylene bisimide gelator molecule (see **Figure 2-20**) that doesn't bear any long alkyl chain nor any solubilizing group, crucial components in the design of organogelators. These side chains, however, are often considered a big disadvantage, as they are not just electronically inactive but also isolating and they prevent the exciton transfer of electrons and holes within the material. The solubility of this gelator molecule is conveyed by a structured aromatic core. The molecules are aligned in a 'head-
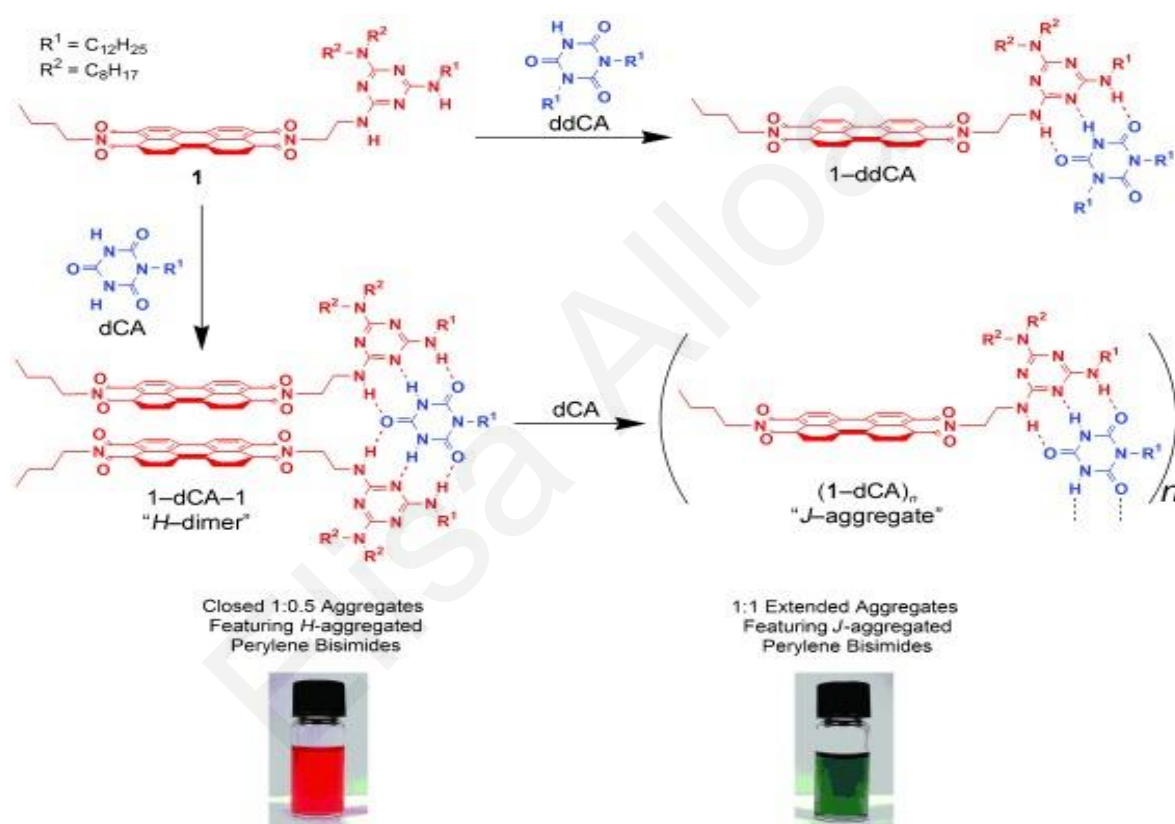
Figure 2-21 Complexation of 1 with the monotopic cyanurate ddCA and the ditopic cyanurate dCA. For 1:0.5 and 1:1 aggregates of 1 and dCA, photographs of their methylcyclohexane solutions are shown.[51]

to-tail' manner directed by hydrogen bonds. In this packing arrangement one dye interacts with four neighboring ones through π–π interactions, leading to strong J-type excitonic coupling. It is able to self-assemble into highly fluorescent one-dimensional structures through H-bonding at extremely low gelation concentrations.

J-aggregate PBIs show an extended exciton mobility exploitable for example in organic solar cells. Contrarily, H-aggregate possess a high n-type carrier mobility, favorable in electronic devices. The potential conversion of a form into the other one is thus the most profitable outcome.

An example of a core-unsubstituted perylene bisimide that self-organizes upon addition of 0.5 equivalents of ditopic cyanurate into H-type dimers was described in **Figure 2-21**. Furthermore, adding 1 equivalent of cyanurate to the H-dimers, interestingly makes them to convert into J aggregates with a >100 nm red-shifted absorption band compared to the monomer. Such an idea for the switch in between H- and J-type aggregates has the perspective to generate responsive aggregates to be used as fluorescent sensors.[9,52]

2.2 Conjugated polymer systems for optoelectronics

Another approach in optoelectronics is using conjugated polymers. Broad academic and industrial interest has been shown for conjugated polymers for various optoelectronic applications. Comparing to inorganic materials, conjugated polymers manifest clear advantages, such as light weight, feasible/large-scale manufacturing, low cost, and flexibility. While a conjugated polymer system can attain electrical properties similar to the inorganic semiconductor counterparts, molecular structure plays an essential role in the functionality of these polymer systems. The optoelectronic properties of those conjugated materials are determined by their π electrons, which can be excited with light inducing a slight deformation of the polymer backbone. [53]

2.2.1 Excited state processes

Understanding the excited state ultrafast dynamics of electronic excited states of π-conjugated oligomers and polymers is of fundamental importance for their applications and improvements in optoelectronics. Electronic excited state evolution is a complex process that couples both electronic and nuclear degrees of freedom, and plays a central role in photophysical processes that ultimately determine the optoelectronic properties of these organic materials.[54] Understanding these excitation and relaxation patterns is of fundamental importance in chemical physics to optimize quantum efficiencies and performances of optoelectronic devices,[55] e.g. in light-emitting diodes (LEDs) and polymer lasers,[56] for the investigation of photosensitive systems,[57] or for organic polariton lasers.[58] Exciton migration and torsional relaxation are examined in the next subsections.

2.2.1.1 Exciton migration

Energy flow across organic systems proceeds throughout the transfer of electrically neutral excitons. Exciton migration in conjugated polymer systems plays an important role in determining the efficiency of polymer electronic devices. In photovoltaic devices indeed a large exciton diffusion length is essential so that excitons can efficiently migrate to regions where charge separation can occur. Conjugated polymers undergo energy transport by exciton diffusion, either in dilute or aggregated solutions or in solid films, as represented in **Figure 2-22**. Many studies[59–61] put efforts into elucidating the major exciton migration mechanisms underlying excitation phenomena in conjugated materials. As exciton migration impacts the subsequent device efficiency it is essential to understand in detail and control the energy flow in organic materials. An important point to be addressed in setting up a microscopic model for the organization of the chromophores and design of elaborate systems with predictable exciton dynamics, concerns the relative efficiency of motion along the conjugated backbone of a single polymer or between closely spaced chromophore chains (inter- versus intrachain energy migration). Intrachain energy transfer processes have been proven to be slower (apart from planar chains) because of weak dipole coupling along the propagating excitons. Conjugation defects inside a chain may also impact the energy transport dynamics by trapping a moving exciton in a polymer system.[61–64] The molecular arrangement and strand alignment inside the material influence exciton migration.
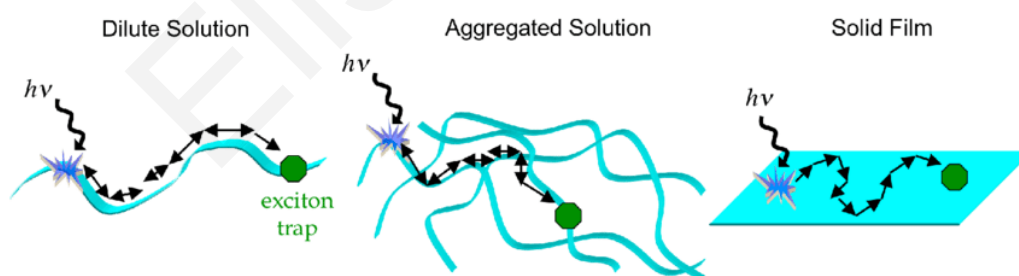

Figure 2-22 Schematic representations of exciton migration in conjugated polymers in a dilute solution, an aggregated solution, and a solid film.[65]

Orientational disorder also influences exciton diffusion due to the number of physical traps: as represented in **Figure 2-23**, in a polymer with parallel and random chain orientations relative to the substrate surface, exciton migration length is about 60 and 70% higher, respectively, than when conjugated chains are found perpendicular to the surface. The

specific nanomorphology of the molecular structure is consequently a very important parameter to be considered for energy transfer efficiency.[66]
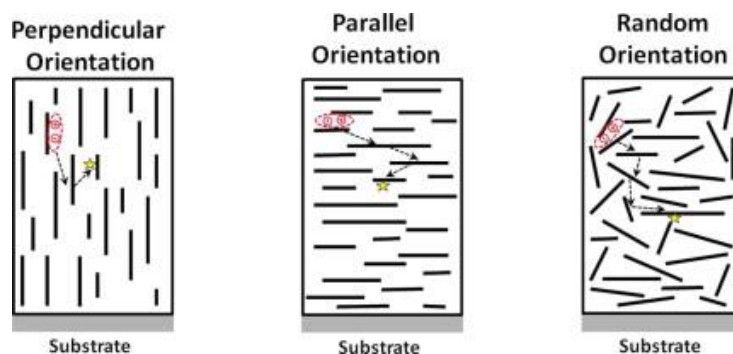

Figure 2-23 Exciton diffusion model to the substrate surface with perpendicular, parallel and random orientation of the strands.[66]

The effective migration of excitons is important in many energy transport processes, i.e. sensor devices, photosynthesis, and photovoltaics. Considering both artificial and natural light harvesting aggregates, the efficient creation and migration of excitons dictate the optical properties of such systems: solar energy is captured and transferred to reaction centers on a 10−100 ps time scale. This ultrafast timescale, together with a proper aggregate population and coherence-transfer dynamics, reduces losses due to exciton recombination with ground state holes.[67] Once the excitation is relocated through space among the chromophores, it eventually reaches a reaction centre (antenna complex) where charge separation is carried out with a specific quantum efficiency (e.g. 84-90% for photosystem II of higher plants).[68] Energy transfer of electronic excitation energy in light-harvesting systems occurs through the well-known mechanism named RET (resonant energy transfer), which is based on electronic coherence between electronically excited states of donor and acceptor units inside the chromophores. Following photoexcitation, coulombic interaction drives their electronic excitation and charge transfer with each other. For large distances between the molecules, this interaction becomes a dipole–dipole coupling and the exchange of excitation is slower compared with the relaxation processes.[21]

The effects of exciton migration can be disentangled from the ones deriving from other excited state processes (see the next *Subchapter*) by employing smaller organic structures, e.g. oligomers, where this diffusive process is limited to occur because of the restricted conjugation length.[69]

2.2.1.2 Torsional relaxation

The torsional relaxation of a polymer backbone happens when excitons go through a decay process within the time scale of vibrational relaxation by cooling down from the original "hot" state. In **Figure 2-24** an overview of the basic excited state series of events is presented: after the initial photoexcitation, excited state evolution initiates with exciton self-trapping, followed by torsional relaxation, and the final relaxation to the ground state; those processes respectively happen in femto-, pico-, and nanosecond timescales.[70] Conjugated oligomers first absorb light and within few hundred femtoseconds the excitons rapidly
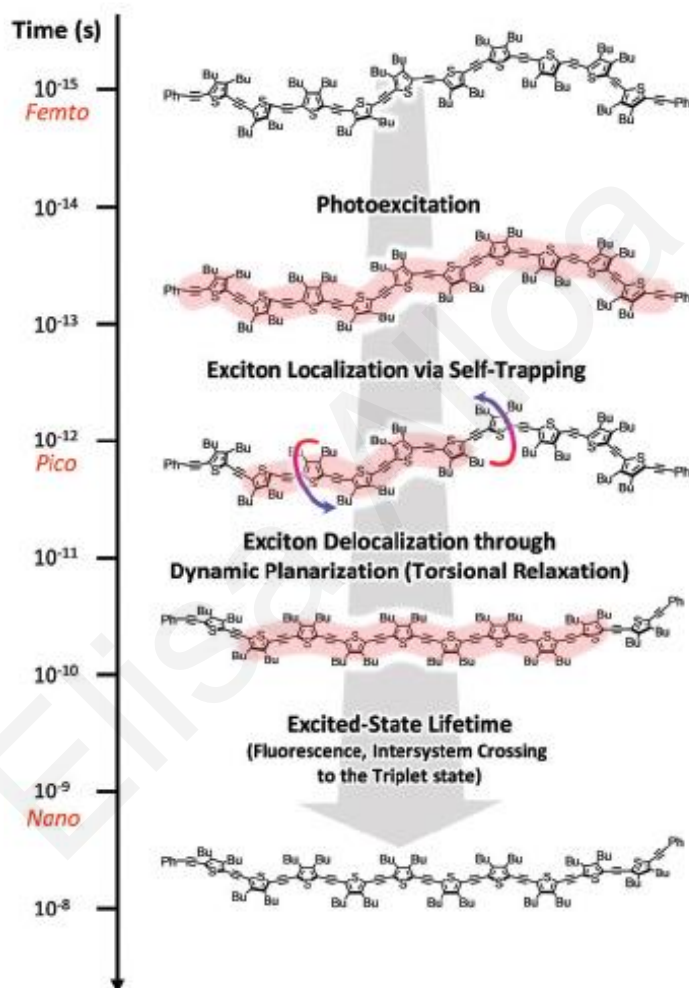

Figure 2-24 Schematic representation of excited-state dynamics of linear oligothiophenes from femto- to nanosecond timescales.[70]

localize on conjugated parts of the chain: this is called exciton localization process. After this ultrafast process (happening in the sub-ps regime), an additional relaxation process occurs within picoseconds: the dynamic planarization process, which is also named torsional relaxation. During this planarization of the molecular backbone, the torsional angle between the monomeric units reduces. Exciton delocalization happens along the oligomer chain causing a reduction of the excited state energy. The spectral dynamics occurring on

picosecond time scales in systems like porphirins or oligothiophenes [70–73] are related to exciton delocalization through dynamic planarization. Despite this significant finding, the evolution of a molecular state from an initial vibrationally excited state to a geometrically relaxed one still requires further investigation.[70,72,74] Indeed, it would be useful to discriminate and get more insights about both the exciton localization and delocalization processes, however the ultrafast timescale of these processes makes these findings still challenging to be attained.

2.2.2 Structural dynamics studies

In this work, femtosecond stimulated Raman spectroscopy (FSRS)[75–77] was employed in light of understanding ultrafast excited state spectral relaxation and photoinduced conformational changes in polymeric semiconductors at very early times following excitation. FSRS, apart from providing a complete vibrational spectrum on the timescale that is most valuable for understanding reaction kinetics of photoexcited conjugated molecules, it can specifically probe the evolution of specific modes, focusing on a more localized observation of structural change.[78]

So far several studies have interrogated the relaxation processes of photoexcited π-conjugated oligomers using time-resolved spectroscopies: time-resolved fluorescence and transient stimulated emission have been employed on oligothiophenes in order to understand the charge photogeneration processes. In order to discriminate the different stages which characterize the whole excitation process, oligo- and polyfluorenes have been studied by picosecond single photon counting and streak camera techniques in order to disentangle contributions to relaxation effects from exciton migration and conformational rearrangement.[59,79,80]

Both experimental and theoretical studies on OFs have monitored the excited state evolution, attributing it to conformational relaxation and in particular to planarization of the oligomers/polymer, that ultimately yields a quinoidal excited-state geometry.[18] Time-resolved resonance Raman (TRRR) technique provides significant structural description of organic conjugated systems,[82,83] however it doesn't reach the time resolution achieved by FSRS.[84] The torsional relaxation dynamics occurs on a subpicosecond to picosecond timescale and can be resolved using transient absorption spectroscopy and stimulated emission. A key feature in order to get insights on the structural rearrangement in oligofluorenes is the torsional dynamics concerning the conjugated backbone, as calculated in the study of Franco and Tretiak.[54]

Exciton delocalization plays therefore a key role in the understanding of these conjugated systems, however more stages occur along the process: in order to get a deeper understanding on the internal energy redistribution process, the highly polarizable π-electron system of conjugated molecules should be properly investigated and addressed at different timescales, providing thus insights on different phases occurring during the overall excited-state process (as seen in the previous *Subchapter*). Exciton self-trapping (occurring in a femtosecond timescale) precedes and leads the following exciton delocalization process and it is thus of fundamental importance. For a complete assessment of excitons behavior, it should be considered that the absorption is dominated by completely delocalized excitations, while the fluorescence comes from the recombination of self-trapped excitons, i.e. an exciton is completely delocalized along the chain in its 'hot' state, while it self-traps itself after vibrational relaxation.[54]

A confinement of the excitation on some segments of the structure may be also induced by conformational disorder. This phenomenon is called exciton localization or exciton self-trapping, meaning that the localization in space of the excitation energy caused by the nuclear rearrangement of the molecule undergoes a redistribution in charge density from the delocalized starting state. This process impacts the chromophore energy distribution and may contribute to the origin of intramolecular interchromophoric electronic coherences with relevant potential outcomes, e.g. an efficient charge generation.[79,85,86]

Observations that resulted from these optical techniques provided an overall picture of the series of events that occur post photoexcitation, that eventually lead to a global planarization of the oligofluorene molecules.[87] However, direct observation of the structural dynamics involved has not yet been achieved. FSRS can offer this possibility based on the high sensitivity provided by Raman spectroscopy by following e.g. evolution of torsional modes, lengthening and shortening of C=C and C-C bonds.[88]

Even though much effort has been dedicated to a wider understanding of these processes, determination of the excited-state molecular structure and details of conformational evolution at the very early-time have still to be properly clarified.

2.2.3 Oligofluorenes: a model for ultrafast evolution

Oligofluorenes (OFs) are fluorescent conjugated oligomers attracting a wide research interest due to their applications as laser dyes and as emitters in OLEDs in their polymeric form.[89] A series of fluorene oligomers (OFs) are used in the present thesis as a must-have

model system for a detailed study of excited state processes within homopolymeric materials. As explained above, excited-state structural relaxation dynamics and associated exciton delocalization processes are indeed capable of highlighting the conformational and electronic changes in conjugated polymers that arise by excitation. Polyfluorene is an archetypical π-conjugated "blue" emitting polymer[90,91] and, as such, various aspects of its photophysics have been investigated by a wealth of spectroscopic methods.[92] The complexity of the excited state dynamics can be reduced by employing model oligomeric systems. Oligomers of different chain length (in **Figure 2-25** the series of OFs employed herein) could indeed support the process of relating spectral dynamics with structural evolution, by observing their excited state dynamics change from monomer to polymer, with a particular focus on the determination of the excited-state molecular structure and the early-time dynamics of configurational change.
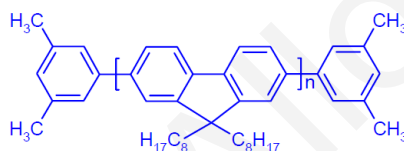
 Figure 2-25 Structure of OFs studied. Three oligomers were investigated (n = 3, 5, and 7).

Following a bottom-up approach, this study is therefore along the lines of the so-called "oligomer approach", in order to elucidate how oligomer chain length may affect structural dynamics of longer structures: a series of oligomers are studied in a step-by-step process to understand their excited state evolution process in a microscale and applying then this knowledge to more complex polymer structures. Different computational studies were carried out up to date in order to find correlations among oligomers with different chain lengths. Franck-Condon analysis was employed on polyenes with increasing polyene chain length. These reveal variable displacement trends of the C=C and C–C stretching vibrational modes (with an opposite behavior between the 2 ^{1}Ag and 1 ^{1}Bu states because of their different electronic configurations), together with absorption and fluorescence bandwidths exhibiting a monotonic decrease (by increasing chain length).[93] Jansson et al. investigated the dihedral angle change in oligofluorenes (from monomer to heptamer) demonstrating that upon excitation from S1 to T1 the dihedral angle between two adjacent monomers almost goes to zero, i.e. the two adjacent monomers are only a few degrees from forming a planar structure within the oligomer.[94] Chen et al. explored the natures of charges and excited states in conjugated oligomers of different lengths, in order to provide insights into electron and

energy transfer according to the conjugation length parameter, considering that charges and excitons do not distribute along the entire lengths of the conjugated oligomer, but partially delocalize by forming polarons. The work was carried out by measuring reduction potentials (a ground state property), and excited state energies coming from the lowest triplet for oligofluorenes of different lengths. It has been highlighted that the energy of the polaron becomes constant for chain lengths greater than the delocalization length, while free energies for forming anions or triplets changes rapidly with increasing length and becomes constant for lengths longer than the delocalization length (which for the electron polaron is 4−5 units).[95]

These fluorene oligomers exhibit, apart from blue emission, high fluorescence quantum yield, good carrier mobility, good thermal and electrochemical stability, facile chemical modification; all significant features which make them suitable and representative models to investigate the excited state relaxation.[96]

2.3 Polydiacetylene-Decorated Nanoparticles for all-optical switching applications

In this final section, we will describe the last system of interest in this thesis. Polydiacetylenes (PCDA) have been primarily chosen because of their intense vibrational signal, in light of assessing the stimulated Raman technique developed herein (useful for fluorescent samples like perylene bisimides). The large Raman cross-section of the C=C and C≡C vibrations of these polymers (see **Figure 2-26**) makes them good candidates as well to apply the stimulated / inverse Raman effect (IRS) to obtain all-optical switching in these materials. This process has attracted relevant research interest in many areas, as nanophotonics, nonlinear optics, material science, and optical communications.[97] The ultrafast feedback and the nonlinear optical response that may be achieved by PCDA materials (coupled to nanoparticles to further increase the Raman signal) have the potential to achieve the high performance indexes needed for all-optical switching to a great degree.

Polydiacetylene (PCDA) assemblies are conjugated chromatic polymers studied in various fields of science and engineering, including chemistry, biology, materials science and electronics, which have attracted significant interest over the past 40 years as a promising platform for chemo- and bio-sensing. Their optical, spectral, electronic and structural properties, due to their π-electron delocalization in their backbone, provide the material with special stimuli responsive and conduction properties, and thus exploitable, e.g., in sensing and signal transmission. Different dimensional arrangements of PCDAs appear to be more

suitable for certain application areas (for example, 2D films for imaging technology and 3D structures for sensing applications).[98,99] The molecular structure is characterized by the presence of C-C alternating double and triple bonds. Color transition from blue to red (achieved in the processing phase by increasing the temperature) and exciton coherence in these polymers make them appropriate for sensor applications. Indeed, an unequivocal optical fingerprint for the detection of molecules (e.g. DNA, food spoilage molecules[100,101]) is guaranteed by the quantum superposition of excited electronic states of different chromophores resulting into bright fluorescent excitons: superradiant effects which may be indeed exploitable for non-linear outcomes like all-optical switching.[21,102,103]
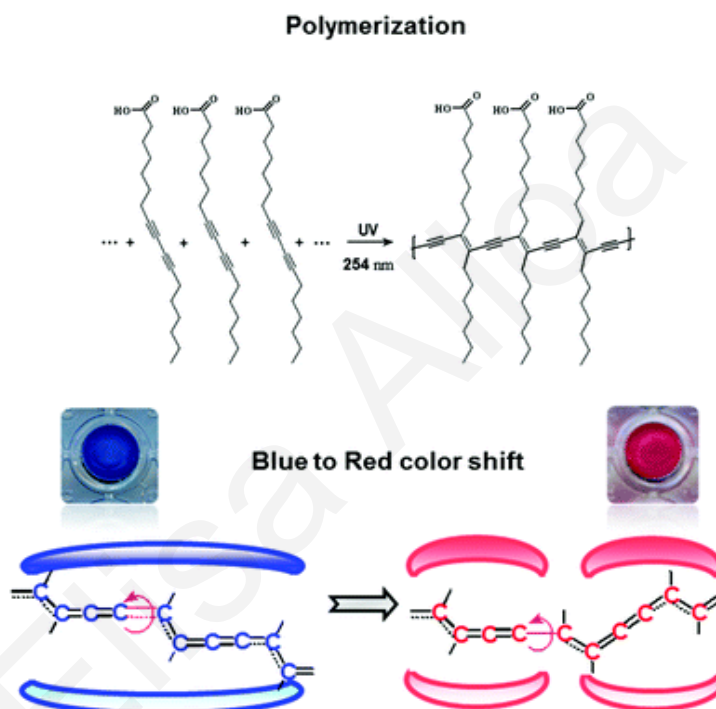
Figure 2-26 PCDA photo-polymerization and thermal conversion.[98]

For the current study, PCDA was coupled to metal nanoparticles in order to further increase its stimulated Raman signal. This enhancement is based on the Surface Enhanced Raman Scattering, (SERS), a phenomenon where Raman scattering by molecules adsorbed on metal surfaces is enhanced, due to the plasmon resonance generated at the metal due to the excitation light. Gold and silver nanoparticles were used for this purpose, in order to compare the enhancement obtained.[104,105] **Figure 2-26** shows the PCDA structure conversion under UV irradiation and heat. PCDA first self-assembles and polymerizes onto nanoparticles by forming a triple bond among the chains and thus generates its blue form. Conversion to the red phase is achieved by thermal treatment and is obtained by a change in the electronic configuration of the chain itself.[106]

References

1. Bixon, M. & Jortner, J. Electron transfer-from isolated molecules to biomolecules. *Adv. Chem. Phys.* **43**, 35–202 (2007).

2. McConnell, I., Li, G. & Brudvig, G. W. Energy conversion in natural and artificial photosynthesis. *Chem Biol* **17**, 434–447 (2010).

3. Scheibe, G., Kandler, L. & Ecker, H. Polymerisation und polymere adsorption als ursache neuartiger absorptionsbanden von organischen Farbstoffen. *Naturwissenschaften* **25**, 75 (1937).

4. Jelley, E. E. Spectral absorption and fluorescence of dyes in the molecular state. *Nature* **138**, 1009–1010 (1936).

5. Akins, D. L. Enhanced Raman scattering by molecular nanoaggregates. *Nanomater. Nanotechnol.* **4**, 1 (2014).

6. Eisfeld, A. & Briggs, J. S. The J- and H-bands of organic dye aggregates. *Chem. Phys.* **324**, 376–384 (2006).

7. Sorokin, A. V., Ropakova, I. Y., Borovoy, I. A., Bespalova, I. I. & Yefimova, S. L. Using cyanine dye J-aggregates as luminescence probe for nanostructured media. *Funct. Mater.* **24**, 388–392 (2017).

8. Hestand, N. J. & Spano, F. C. Molecular Aggregate Photophysics beyond the Kasha Model: Novel Design Principles for Organic Materials. *Acc. Chem. Res.* **50**, 341–350 (2017).

9. Würthner, F., Kaiser, T. E. & Saha-Möller, C. R. J-aggregates: from serendipitous discovery to supramolecular engineering of functional dye materials. *Angew. Chemie - Int. Ed.* **50**, 3376–3410 (2011).

10. Embriaco, D., Balagurov, D. B., La Rocca, G. C. & Agranovich, V. M. Topical questions in the photophysics of J aggregates. *Phys. status solidi* **1**, 1429–1438 (2004).

11. Kobayashi, T. J-aggregates. *World Sci.* **17**, 67–94 (1996).

12. Potma, E. O. & Wiersma, D. A. Exciton superradiance in aggregates: the effect of disorder, higher order exciton-phonon coupling and dimensionality. *J. Chem. Phys.*

108, 4894–4903 (1998).

13.   Mcrae, E. G. & Kasha, M. Enhancement of phosphorescence ability upon aggregation of dye molecules [6]. *J. Chem. Phys.* **28**, 721–722 (1958).

14.   Kitamura, C. Tuning the solid-state optical properties of tetracene derivatives by modification of the alkyl side-chains: Crystallochromy and the highest fluorescence quantum yield in acenes larger than anthracene. *Chem. Rec.* **12**, 506–514 (2012).

15.   Kirstein, S. & Möhwald, H. Exciton band structures in 2D aggregates of cyanine dyes. *Adv. Mater.* **7**, 460–463 (1995).

16.   Spano, F. C. & Silva, C. H- and J-aggregate behavior in polymeric semiconductors. *Annu. Rev. Phys. Chem.* **65**, 477–500 (2014).

17.   Hestand, N. J. & Spano, F. C. Interference between Coulombic and CT-mediated couplings in molecular aggregates: H- to J-aggregate transformation in perylene-based π-stacks. *J. Chem. Phys.* **143**, 244707 (2015).

18.   https://en.wikipedia.org/wiki/Exciton (Accessed: 12th April 2019).

19.   Fox, M. *Optical Properties of Solids, Second Edition*. *Oxford Master Series in Physics* (Oxford University Press, 2011).

20.   Reynolds, D. C., Collins, T. C. & Sturge, M. Excitons: Their Properties and Uses. in *Physics Today* **36**, 73–75 (Academic Press, 1983).

21.   Fassioli, F., Dinshaw, R., Arpin, P. C. & Scholes, G. D. Photosynthetic light harvesting: excitons and coherence. *J. R. Soc. Interface* **11**, 20130901 (2014).

22.   Herz, A. H. Aggregation of sensitizing dyes in solution and their adsorption onto silver halides. *Adv. Colloid Interface Sci.* **8**, 237–298 (1977).

23.   Wang, Y. Resonant third-order optical nonlinearity of molecular aggregates with low-dimensional excitons. *J. Opt. Soc. Am. B* **8**, 981 (1991).

24.   Dicke, R. H. Coherence in spontaneous radiation processes. *Phys. Rev.* **93**, 99–110 (1954).

25.   https://www.kobo.com/us/en/ebook/superradiance-1 (Accessed: 8th April 2019).

26.   Bohnet, J. G. *et al.* A steady-state superradiant laser with less than one intracavity photon. *Nature* **484**, 78–81 (2012).

27.   Mal'tsev, E. I. *et al.* J-aggregate electroluminescence in dye doped polymer layers. *Appl. Phys. Lett.* **73**, 3641–3643 (1998).

28.   Meng, Q. S. *et al.* Tunneling electron induced molecular electroluminescence from individual porphyrin J-aggregates. *Appl. Phys. Lett.* **107**, 43103 (2015).

29.   Akins, D. L. Theory of Raman scattering by aggregated molecules. *J. Phys. Chem.* **90**, 1530–1534 (1986).

30.   Coles, D. M. *et al.* A characterization of the Raman modes in a J-aggregate-forming dye: a comparison between theory and experiment. *J Phys Chem A* **114**, 11920–11927 (2010).

31.   Rich, C. C. & McHale, J. L. Resonance Raman spectra of individual excitonically coupled chromophore aggregates. *J. Phys. Chem. C* **117**, 10856–10865 (2013).

32.   Conceição, D. S., Ferreira, D. P. & Vieira Ferreira, L. F. Photochemistry and cytotoxicity evaluation of heptamethinecyanine near infrared (NIR) dyes. *Int. J. Mol. Sci.* **14**, 18557–18571 (2013).

33.   Qiao, Y., Polzer, F., Kirmse, H., Kirstein, S. & Rabe, J. P. Nanohybrids from nanotubular J-aggregates and transparent silica nanoshells. *Chem. Commun.* **51**, 11980–11982 (2015).

34.   Smith, K. M. Nomenclature of the bacteriochlorophylls c, d, and e. *Photosynth. Res.* **41**, 23–26 (1994).

35.   Satake, A. & Kobuke, Y. Artificial photosynthetic systems: assemblies of slipped cofacial porphyrins and phthalocyanines showing strong electronic coupling. *Org Biomol Chem* **5**, 1679–1691 (2007).

36.   Okada, O., Oka, K. & Iijima, M. Study of the crystal structure of titanylphthalocyanine by rietveld analysis. II. *Jpn. J. Appl. Phys.* **32**, 3556–3560 (1993).

37.   Weil, T., Vosch, T., Hofkens, J., Peneva, K. & Müllen, K. The rylene colorant family-tailored nanoemitters for photonics research and applications. *Angew. Chemie - Int. Ed.* **49**, 9068–9093 (2010).

38.   Würthner, F. Perylene bisimide dyes as versatile building blocks for functional supramolecular architectures. *Chem. Commun.* **4**, 1564–1579 (2004).

39.   Sun, M., Müllen, K. & Yin, M. Water-soluble perylenediimides: design concepts and biological applications. *Chem. Soc. Rev.* **45**, 1513–1528 (2016).

40.   Zhang, C. *et al.* Thienobenzene-fused perylene bisimide as a non-fullerene acceptor for organic solar cells with a high open-circuit voltage and power conversion efficiency. *Mater. Chem. Front.* **1**, 749–756 (2017).

41.   Kaiser, T. E., Wang, H., Stepanenko, V. & Würthner, F. Supramolecular construction of fluorescent J-aggregates based on hydrogen-bonded perylene dyes. *Angew. Chemie* **119**, 5637–5640 (2007).

42.   Nowak-Król, A., Shoyama, K., Stolte, M. & Würthner, F. Naphthalene and perylene diimides – better alternatives to fullerenes for organic electronics? *Chem. Commun.* **54**, 13763–13772 (2018).

43.   Zhou, J. *et al.* Magic-angle stacking and strong intermolecular π-π interaction in a perylene bisimide crystal: an approach for efficient near-infrared (NIR) emission and high electron mobility. *J. Phys. Chem. Lett.* **9**, 596–600 (2018).

44.   Hippius, C., Schlosser, F., Vysotsky, M. O., Böhmer, V. & Würthner, F. Energy transfer in calixarene-based cofacial-positioned perylene bisimide arrays. *J. Am. Chem. Soc.* **128**, 3870–3871 (2006).

45.   Struijk, C. W. *et al.* Liquid crystalline perylene diimides: architecture and charge carrier mobilities. *J. Am. Chem. Soc.* **122**, 11057–11066 (2000).

46.   Tsai, H. Y., Chang, C. W. & Chen, K. Y. 1,6- and 1,7-regioisomers of asymmetric and symmetric perylene bisimides: synthesis, characterization and optical properties. *Molecules* **19**, 327–341 (2013).

47.   Grande, V., Soberats, B., Herbst, S., Stepanenko, V. & Würthner, F. Hydrogen-bonded perylene bisimide J-aggregate aqua material. *Chem. Sci.* **9**, 6904–6911 (2018).

48.   Chang, C. W., Tsai, H. Y. & Chen, K. Y. Green perylene bisimide dyes: Synthesis, photophysical and electrochemical properties. *Materials (Basel).* **7**, 5488–5506 (2014).

49.   Kaiser, T. E., Stepanenko, V. & Würthner, F. Fluorescent J-aggregates of core-substituted perylene bisimides: Studies on structure-property relationship, nucleation-

elongation mechanism, and sergeants-and-soldiers principle. *J. Am. Chem. Soc.* **131**, 6719–6732 (2009).

50. Ghosh, S., Li, X. Q., Stepanenko, V. & Würthner, F. Control of H- and J-type pi stacking by peripheral alkyl chains and self-sorting phenomena in perylene bisimide homo- and heteroaggregates. *Chemistry (Easton).* **14**, 11343–11357 (2008).

51. Yagai, S., Seki, T., Karatsu, T., Kitamura, A. & Würthner, F. Transformation from H- to J-aggregated perylene bisimide dyes by complexation with cyanurates. *Angew. Chemie* **120**, 3415–3419 (2008).

52. Würthner, F., Bauer, C., Stepanenko, V. & Yagai, S. A black perylene bisimide super gelator with an unexpected J-type absorption band. *Adv. Mater.* **20**, 1695–1698 (2008).

53. Inganäs, O. & Zhang, F. Polymer optoelectronics - towards nanometer dimensions. *Nanotechnol. Nano-Interface Control. Electron. Devices* **45**, 65–81 (2003).

54. Franco, I. & Tretiak, S. Electron-vibrational dynamics of photoexcited polyfluorenes. *J. Am. Chem. Soc.* **126**, 12130–12140 (2004).

55. Li, Y. *et al.* Ultrafast carrier dynamics in two-dimensional transition metal dichalcogenides. *J. Mater. Chem. C* **7**, 4304–4319 (2019).

56. Dickson, R. M., Cubitt, A. B., Tsien, R. Y. & Moerner, W. E. On/off blinking and switching behaviour of single molecules of green fluorescent protein. *Nature* **388**, 355–358 (1997).

57. Tang, L. *et al.* Excited state structural evolution of a GFP single-site mutant tracked by tunable femtosecond-stimulated Raman spectroscopy. *Molecules* **23**, 2226 (2018).

58. Wei, M. *et al.* Low-threshold polariton lasing in a highly disordered conjugated polymer. *Optica* **6**, 1124 (2019).

59. Hintschich, S. I., Dias, F. B. & Monkman, A. P. Dynamics of conformational relaxation in photoexcited oligofluorenes and polyfluorene. *Phys. Rev. B - Condens. Matter Mater. Phys.* **74**, 1–10 (2006).

60. Ma, X. S. *et al.* 2D hyperbranched conjugated polymer for detecting TNT with excellent exciton migration. *Sensors Actuators, B Chem.* **238**, 48–57 (2017).

61. Lim, T. L. *et al.* Illumination of exciton migration in rodlike luminescent conjugated

polymers by single-molecule spectroscopy. *Phys. Rev. B - Condens. Matter Mater. Phys.* **67**, (2003).

62. Willis-Fox, N. *et al.* Synergistic photoluminescence enhancement in conjugated polymer-di-ureasil organic-inorganic composites. *Chem. Sci.* **6**, 7227–7237 (2015).

63. Nguyen, T. Q., Wu, J., Doan, V., Schwartz, B. J. & Tolbert, S. H. Control of energy transfer in oriented conjugated polymer-mesoporous silica composites. *Science (80-.).* **288**, 652–656 (2000).

64. Meng, R. *et al.* Exciton transport in π-conjugated polymers with conjugation defects. *Phys. Chem. Chem. Phys.* **19**, 24971–24978 (2017).

65. Controlling the architectures and optical properties of conjugated polymer aggregates and films. Available at: https://www.researchgate.net/publication/38000035_Controlling_the_architectures_ and_optical_properties_of_conjugated_polymer_aggregates_and_films/figures?lo=1 . (Accessed: 18th November 2019)

66. Correia, H. M. G., Barbosa, H. M. C., Marques, L. & Ramos, M. M. D. Unravelling the effect of strand orientation on exciton migration in conjugated polymers. *Comput. Mater. Sci.* **75**, 18–23 (2013).

67. Milota, F. *et al.* Vibronic and vibrational coherences in two-dimensional electronic spectra of supramolecular J-aggregates. *J. Phys. Chem. A* **117**, 6007–14 (2013).

68. Blankenship, R. E. Molecular mechanisms of photosynthesis. *Mol. Mech. Photosynth.* **43**, 1–321 (2008).

69. Fu, Y. *et al.* Insight into correlation between molecular length and exciton dissociation, charge transport and recombination in Polymer: Oligomer based solar cells. *Org. Electron. physics, Mater. Appl.* **58**, 75–81 (2018).

70. Park, K. H. *et al.* Excited-state dynamic planarization of cyclic oligothiophenes in the vicinity of a ring-to-linear excitonic behavioral turning point. *Angew. Chemie - Int. Ed.* **54**, 12711–12715 (2015).

71. Kim, P. *et al.* Relationship between dynamic planarization processes and exciton delocalization in cyclic oligothiophenes. *J. Phys. Chem. Lett.* **6**, 451–456 (2015).

72. Kim, T. W. *et al.* Chain-length dependent exciton dynamics in linear oligothiophenes

probed using ensemble and single-molecule spectroscopy. *J. Phys. Chem. Lett.* **7**, 452–458 (2016).

73.   Chang, M. H., Hoffmann, M., Anderson, H. L. & Herz, L. M. Dynamics of excited-state conformational relaxation and electronic delocalization in conjugated porphyrin oligomers. *J. Am. Chem. Soc.* **130**, 10171–10178 (2008).

74.   Parkinson, P., Müler, C., Stingelin, N., Johnston, M. B. & Herz, L. M. Role of ultrafast torsional relaxation in the emission from polythiophene aggregates. *J. Phys. Chem. Lett.* **1**, 2788–2792 (2010).

75.   Mathies, R. A. Femtosecond stimulated Raman spectroscopy. *Opt. InfoBase Conf. Pap.* **58**, 461–88 (2007).

76.   Dietze, D. R. & Mathies, R. A. Femtosecond stimulated Raman spectroscopy. *ChemPhysChem* **17**, 1224–1251 (2016).

77.   Frontiera, R. R. & Mathies, R. A. Femtosecond stimulated Raman spectroscopy. *Laser Photon. Rev.* **5**, 102–113 (2011).

78.   Zhou, J., Yu, W. & Bragg, A. E. Structural relaxation of photoexcited quaterthiophenes probed with vibrational specificity. *J. Phys. Chem. Lett.* **6**, 3496–3502 (2015).

79.   Park, K. H., Kim, W., Yang, J. & Kim, D. Excited-state structural relaxation and exciton delocalization dynamics in linear and cyclic p-conjugated oligothiophenes. *Chem. Soc. Rev* **47**, 4279 (2018).

80.   Lanzani, G., Nisoli, M., De Silvestri, S. & Tubino, R. Femtosecond vibrational and torsional energy redistribution in photoexcited oligothiophenes. *Chem. Phys. Lett.* **251**, 339–345 (1996).

81.   Fujitsuka, M., Cho, D. W., Huang, H. H., Yang, J. S. & Majima, T. Structural relaxation in the singlet excited state of star-shaped oligofluorenes having a truxene or isotruxene as a core. *J. Phys. Chem. B* **115**, 13502–13507 (2011).

82.   Sahoo, S. K., Umapathy, S. & Parker, A. W. Time-resolved resonance Raman spectroscopy: exploring reactive intermediates. *Appl. Spectrosc.* **65**, 1087–1115 (2011).

83.   Lanzani, G. *et al.* Photophysics of conjugated polymers: The contribution of ultrafast

spectroscopy. *Phys. Status Solidi Appl. Res.* **201**, 1116–1131 (2004).

84.　Greetham, G. M. *et al. ULTRA: A unique instrument for time-resolved spectroscopy. Applied Spectroscopy* **64**, (2010).

85.　Aggarwal, A. V. *et al.* Fluctuating exciton localization in giant π-conjugated spoked-wheel macrocycles. *Nat. Chem.* **5**, 964–970 (2013).

86.　Kim, Y. *et al.* Device annealing effect in organic solar cells with blends of regioregular poly(3-hexylthiophene) and soluble fullerene. *Appl. Phys. Lett.* **86**, 063502 (2005).

87.　Clark, J., Nelson, T., Tretiak, S., Cirmi, G. & Lanzani, G. Femtosecond torsional relaxation. *Nat. Phys.* **8**, 225–231 (2012).

88.　Castiglioni, C., Del Zoppo, M. & Zerbi, G. Vibrational Raman spectroscopy of polyconjugated organic oligomers and polymers. *Journal of Raman Spectroscopy* **24**, 485–494 (1993).

89.　Geng, Y. *et al.* Synthesis, characterization, and optical properties of monodisperse chiral oligofluorenes. *J. Am. Chem. Soc.* **124**, 8337–8347 (2002).

90.　Tamarat, P. *et al.* Stark shift control of single optical centers in diamond. *Phys. Rev. Lett.* **97**, 083002 (2006).

91.　Nirmal, M. *et al.* Fluorescence intermittency in single cadmium selenide nanocrystals. *Nature* **383**, 802–804 (1996).

92.　Scherf, U. & Neher, D. *Advances in Polymer Science: Preface. Advances in Polymer Science* **212**, (2008).

93.　Itoh, T. Franck-Condon analysis of the absorption and fluorescence spectra of all trans α,ω-diphenylpolyenes with one to seven polyene double bonds. *J. Chem. Phys.* **123**, 0–6 (2005).

94.　Jansson, E., Jha, P. C. & Ågren, H. Chain length dependence of singlet and triplet excited states of oligofluorenes: A density functional study. *Chem. Phys.* **336**, 91–98 (2007).

95.　Chen, H. C. *et al.* Chain length dependence of energies of electron and triplet polarons in oligofluorenes. *J. Phys. Chem. C* **121**, 5959–5967 (2017).

96.   Li, W.-J. *et al.* Synthesis and characterization of diazafluorene-based oligofluorenes and polyfluorene. *Polym. Chem.* **4**, 1796 (2013).

97.   Chai, Z. *et al.* Ultrafast all-optical switching. *Adv. Opt. Mater.* **5**, 1600665 (2017).

98.   Jelinek, R. & Ritenberg, M. Polydiacetylenes-recent molecular advances and applications. *RSC Adv.* **3**, 21192–21201 (2013).

99.   Wenzel, M. & Atkinson, G. H. Chromatic properties of polydiacetylene films. *J. Am. Chem. Soc.* **111**, 6123–6127 (1989).

100. Kim, S. *et al.* A polydiacetylene-based colorimetric chemosensor for malondialdehyde detection: A food spoilage indicator. *J. Mater. Chem. C* **5**, 8553–8558 (2017).

101. Jung, Y. K. & Park, H. G. Colorimetric detection of clinical DNA samples using an intercalator-conjugated polydiacetylene sensor. *Biosens. Bioelectron.* **72**, 127–132 (2015).

102. Feierabend, M., Berghäuser, G., Knorr, A. & Malic, E. Proposal for dark exciton based chemical sensors. *Nat. Commun.* **8**, 14776 (2017).

103. Yarimaga, O., Jaworski, J., Yoon, B. & Kim, J. M. Polydiacetylenes: Supramolecular smart materials with a structural hierarchy for sensing, imaging and display applications. *Chem. Commun.* **48**, 2469–2485 (2012).

104. Alloisio, M. *et al.* Synthesis of fluorescent core-shell metal nanohybrids: A versatile approach. *Materials (Basel).* **9**, 417–425 (2016).

105. Dellepiane, G., Cuniberti, C., Alloisio, M. & Demartini, A. Spectroscopical properties of organic/metal nanohybrids. *Phys. Chem. Chem. Phys.* **12**, 2968 (2010).

106. Okada, S., Peng, S., Spevak, W. & Charych, D. Color and Chromism of Polydiacetylene Vesicles. *Acc. Chem. Res.* **31**, 229–239 (1998).

CHAPTER 3

Experimental and computational methods

3.1 Experimental methods

3.1.1 Materials

3.1.1.1 PBIs

The samples studied were synthesized at the University of Würzburg in the group of Prof. Frank Würthner. They are based on perylene bisimide (PBI) molecules and are designed to self-assemble via hydrogen bonding and π–π interactions into a supramolecular J-aggregated structure. We have studied two types of PBIs, differing only in the nature of their side chains in order to modulate and compare the molecular hydrophilicity: a PBI soluble in organic solvents (with hydrophobic alkyl-substituted chains, see **Figure 3-1**, Left)[1] and a water-soluble one (**Figure 3-1**, Right).[2]
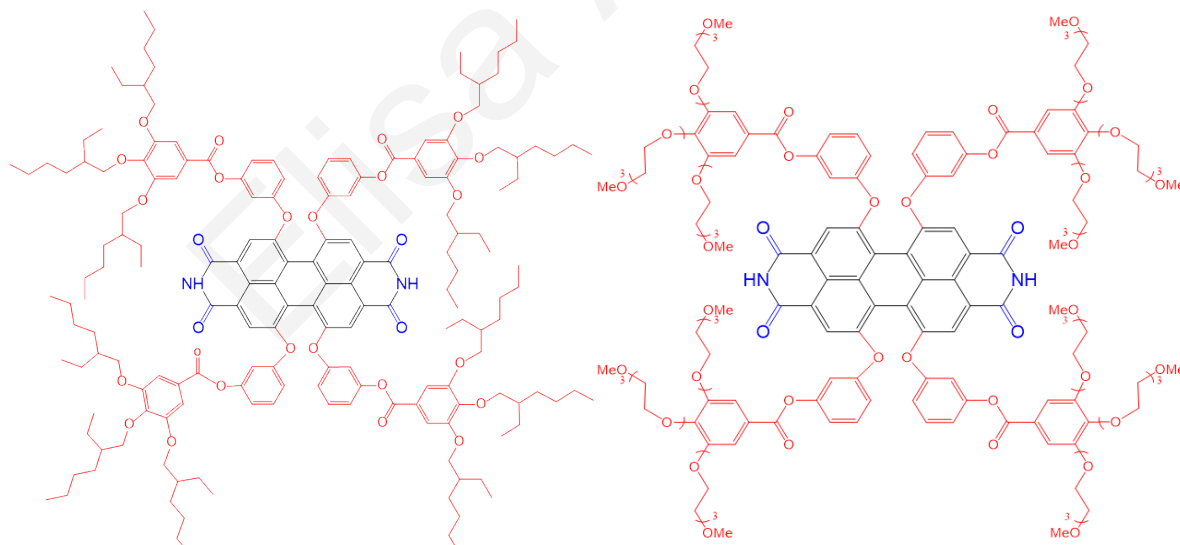
Figure 3-1 Left: Hydrophobic perylene bisimide (MEH-PBI), MW=2777.69 g/mol. **Right:** Water-soluble perylene bisimide molecule (MEG-PBI), MW=3185.35 g/mol.

MEH-PBI and MEG-PBI dyes bear, respectively, 2-ethylhexyl-substituted gallic acid and twelve ethylene glycol chain residues at *meta*-positions of a tetraphenoxy-functionalized perylene bisimide. MEG-PBI is a dark-blue solid that gradually dissolves in water under stirring. MEG-PBI water / deuterated water solutions were prepared at a concentration of 62.5 μM, while a further comparative experiment was

performed with a 6-times diluted solution (10 μM). Higher concentrations were necessary to initiate the aggregate formation in toluene, with a minimum concentration of 2.9 mM. In both cases this was the minimum concentration required for aggregation. A thin film with MEG-PBI in the aggregated state, was prepared by spin-coating a 1mM MEG-PBI in CHCl$_3$ solution on quartz films (rotation speed = 800 rpm, film thickness between 50 - 300 nm). The concentration of the MEH-PBI in organic media (cyclohexane, carbon tetrachloride and benzene) was 41.8 μM.

3.1.1.2 OFs

Oligomers of fluorene {trimer OF3 (9,9,9′,9′,9″,9″-hexakis(octyl)-2,7′,2′,7″-trifluorene), MW=1167.94 g/mol, 98% purity; pentamer OF5 (9,9,9′,9′,9″,9″,9‴,9‴,9⁗,9⁗-decakis(hexyl)-2,7′;2′,7″, 2″,7‴;2‴,7⁗-pentafluorene), MW=1664.62 g/mol, 98% purity; heptamer OF7 (9,9,9′,9′,9″,9″,9‴,9‴,9⁗,9⁗, 9⁗′, 9⁗″, 9⁗‴, 9⁗⁗, 9⁗⁗′-dodecakis(hexyl)-2,7′;2′,7″, 2″,7‴;2‴,7⁗, 2⁗,7⁗′, 2⁗′,7⁗″-heptafluorene, 2327.77 g/mol) were purchased from American Dye Source and were used as received. Solutions of the OFs were prepared in HPLC grade dichloromethane (DCM) at a concentration of 0.2 mg/ml. Chemical structures appear in **Figure 3-2**.
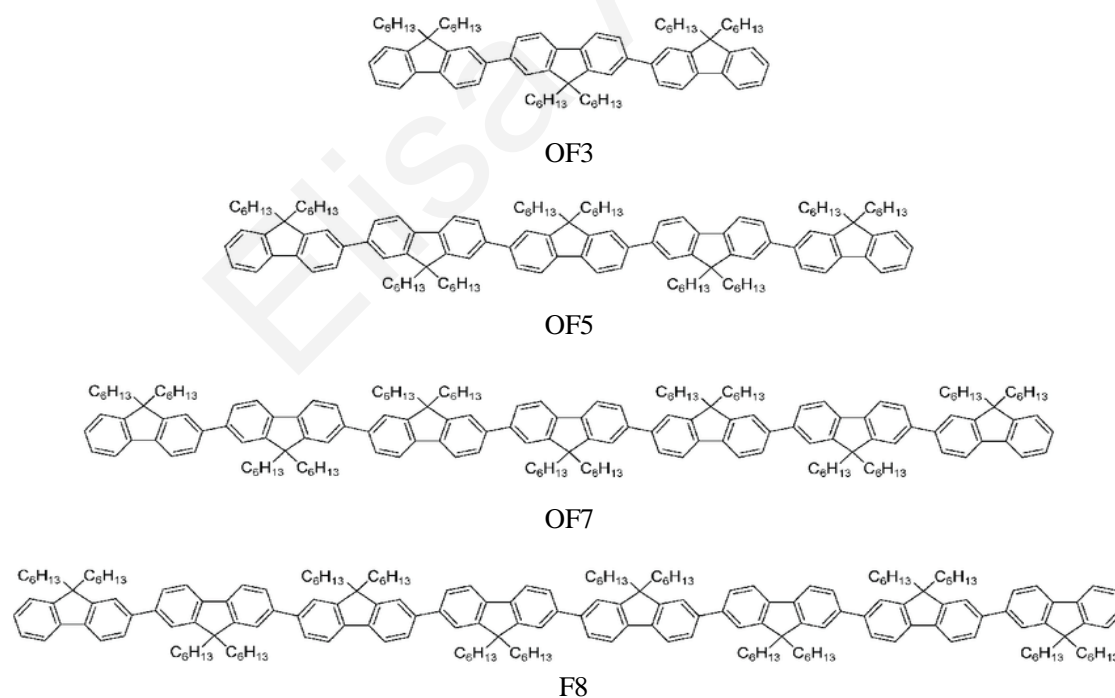
Figure 3-2 Oligofluorenes of different length employed in our study.

3.1.1.3 PCDA

For the synthesis of PCDA, medium molecular mass chitosan (MW= 1.34×10^6 g/mol) was used to stabilize the solutions. The chitosan-protected particles were prepared as follows: a

2% w/v solution of chitosan was obtained in acetic medium by dissolving 100 mg of the polymer in 50 ml of 1% acetic acid solution; 7.2 ml of the as-prepared chitosan solution were added to an aqueous solution of $AgNO_3$ (18 ml, 5 mM) under magnetic stirring and, half an hour later, a freshly prepared aqueous solution of $NaBH_4$ (4.4 ml, 0.1 M) was added drop by drop, maintaining the stirring for approximately 2 h to ensure full reaction. Once synthesized, nanoparticles were kept at 4 °C. Chit/NPs were coated with PCDA molecules by adding the chitosan-protected particles to a 3 mM solution of PCDA monomer dissolved in ethanol. The suspensions were then maintained under vigorous stirring for 3 days in the dark at room temperature. Samples were purified from excess PCDA chains by filtration through a syringe filter. Photopolymerization of the diacetylene outer shell was carried out in a Rayonnet photochemical chamber reactor operating at 254 nm and 35 W power for 1 minute. Subsequently, in order to get the red component of the PCDA (the most thermodynamically stable one), samples were heated at 373 K in an oven for 1 h.[3,4]

3.1.2 Methods
3.1.2.1 RR
3.1.2.1.1 Theoretical background
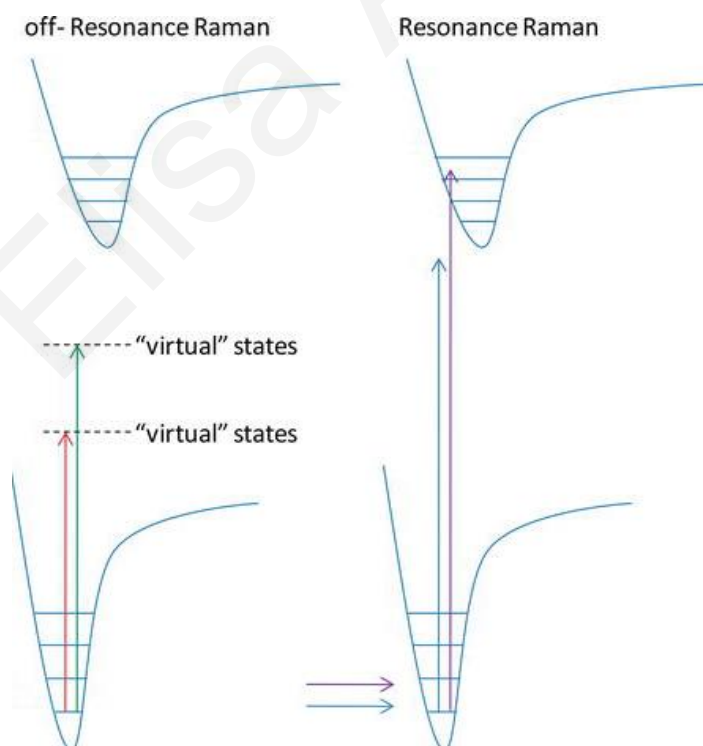
Figure 3-3 Schematic representation of the energy diagrams for a diatomic molecule. The figure represents the off-resonance and the resonant Raman, in which a laser line with enough energy can excite the molecule to other electronic states.

When a monochromatic light beam with a specific frequency impinges on a sample there are three possibilities: passing through it without undergoing changes (transmission), being absorbed (depending on the wavelength of light and the nature of the sample), or being scattered. The Raman process is based on this last process: the largest portion of the incident beam is scattered elastically, i.e. with the same frequency as the incident light (Rayleigh effect). A small percentage of the light undergoes inelastic scattering (Raman effect): it is scattered with a higher or lower frequency than the incident light because of its interaction with the molecule. The difference in energy between the incident and inelastically scattered photons corresponds to the vibrational energy levels of the molecule: the analysis of the displacement of the spectral lines due to Raman effect can therefore provide information on the chemical composition, the molecular structure, the intermolecular interactions of the sample. The Raman effect was independently discovered from the Indians Raman and Krishnan and the Russians Landsberg and Mandelstam in 1928, just a few months apart from each other.[5,6] Scattering recorded at higher energies is named anti-Stokes, while at lower energies is reported as Stokes scattering. In a thermodynamic equilibrium, the lower state is more populated than the upper state. Therefore, the probability of transitions from the more populated lower state to the upper state (Stokes transitions) will be higher than in the opposite direction (anti-Stokes transitions). Correspondingly, Stokes scattering peaks are stronger than anti-Stokes scattering peaks and in most Raman experiments Stokes transitions are detected for better intensities of the acquired spectra. Resonance Raman (RR) spectroscopy is employed to increase the signal-to-noise: to benefit from a resonance enhancement, the incident photon energy is chosen in order to be close in energy to an electronic transition of the material under examination, as represented in **Figure 3-3**. While Raman scattering is usually extremely weak, the frequency resonance can lead to greatly enhanced intensity of the Raman scattering, which facilitates the study of chemical compounds present at low concentrations (until 10^{-6} mol/L). Considering the theoretical formalisms, the Raman cross section of a system going from an initial vibrational state i to a final vibrational state f, with incident energy E_I and scattered energy E_F depends, among other factors, from $a_{i \to f}$, which is the molecular polarizability tensor. Its mathematical expression is given by:

$$\sigma_{i \to f}(E_I) = \frac{8\pi e^4 E_s^3 E_I}{9\hbar^4 c^4} \left| a_{i \to f}(E_I) \right|^2$$

Figure 3-4 Experimental setup for Resonance Raman. **Left:** light at 532 nm coming out from the Raman shifter and properly conveyed through the optical system towards the sample (right). **Right:** sample holder (placed inside a closed-cycle cryostat system), collecting and collimating lenses.
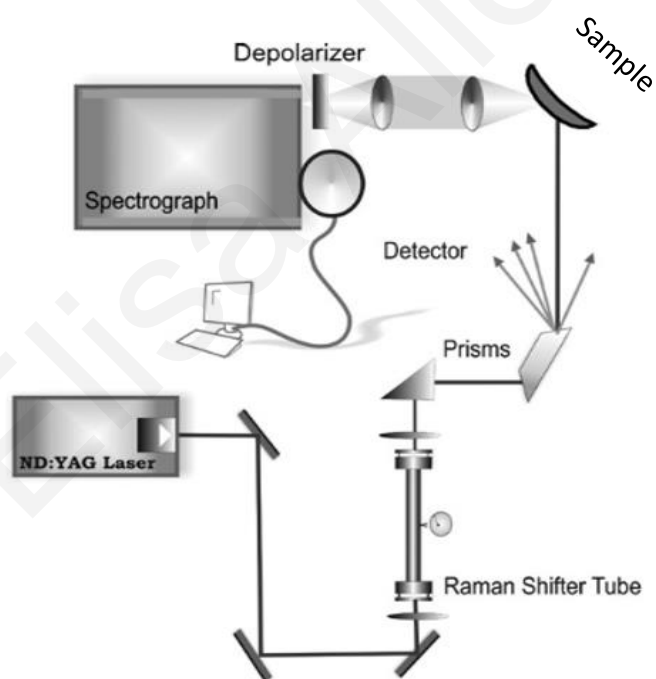
Figure 3-5 Schematic of Raman spectrometer with its components. In the order: YAG laser, Raman shifter tube, prisms, sample, lenses (collecting and collimating), spectrograph and CCD camera, personal computer.

Figure 3-4 and **Figure 3-5** respectively depict the experimental Setup employed for our experiments and the diagram of a Raman spectrometer.

RR spectra provides information about the geometry and the electronic structure of the ground state of the system from the frequency of vibrational bands, while their intensity provides evidence about excited state dynamics and geometry changes between ground and excited states.[7,8] Temperature and solvent dependent RR experiments can provide insights on molecular transitions and dynamics among different states of a molecule.

3.1.2.1.2 Experimental details

Aqueous MEG-PBI samples were excited at 217, 282, 266 and 532 nm, of which the former two were obtained from Raman-shifting in H_2 gas the second harmonic of an Nd:YAG laser at 532 nm, while the 266 nm wavelength is generated from the fourth harmonic of the laser. Further excitations were provided at 405 and 473 nm by CW diode lasers (MonopowerTM 405-50-MM, Alphalas, and Ultralasers, 473 nm, 50 mW OEM DPSS Laser). The aqueous solutions were placed in a custom-made cryocell (Figure 3-6) that was fitted to the cold finger of a sample-in-vacuum closed-cycle cryostat (**Figure 3-4**). The sample cavity had a 13 mm diameter and 3 mm pathlength. The cryostat was fitted on a translation stage for periodic translation of the sample during data acquisition in order to avoid degradation. The toluene samples were placed in a 0.2 mm pathlength suprasil cuvette (Hellma) with a 12.5 μl sample volume. Experiments in the UV were performed with the sample in a spinning cell consisting of an EPR suprasil tube (diameter: 4 mm) attached to a rheostat-controlled motor for choice of rotation speed. Use of the spinning cell prolonged the lifetime of the samples. Both the cuvette and the tube were placed inside a thermostated holder (thermal mantle) controlled by a water bath. Modest excitation powers (0.1 mW for the pulsed lasers, 1 mW for CW lasers) were employed to avoid decomposition of the sample. The Raman scattered light was collected in a 135° backscattering geometry and delivered to a 0.75 m focal-length Czerny−Turner spectrograph, equipped with a 1200-grooves/mm UV-enhanced holographic grating. Experiments in the UV utilized the 2400 gr/mm UV-enhanced holographic grating. The slit width was set to 100 μm providing for ~5 cm^{-1} spectral resolution for the visible wavelengths used in this work, and up to ~12 cm^{-1} for the experiment in the UV. The scattered light was detected by a back-illuminated UV-enhanced CCD detector. Each spectrum presented here is the accumulation of 6 to 12 10-min spectra. Raman spectra of aqueous MEG-PBI samples were obtained at room temperature and 313 K. A long incubation period (overnight) was necessary to reach a stable aggregate state of MEG-PBI. A color change from violet (at room temperature) to blue (at 313 K) confirmed the transition from one form to the other, as shown in **Figure 3-6**. In the case of toluene samples, experiments were run at 283 K, room temperature and 333 K and the temperature was

allowed to stabilize for 10 - 15 min. In this case, the sample turned from dark blue (at 283 K) to violet (at 333K). The MEH-PBI derivative soluble in organic solvents was excited at 473 nm. Its temperature-dependent RR experiments in cyclohexane solution were performed at 277, room temperature and 313 K; in carbon tetrachloride and benzene, experiments were carried out starting from 250 and 280 K, respectively, and up to room temperature. MEH-PBI samples turned from dark blue (lower temperature) to bright orange (higher temperature). Immediate solubilization of the molecule and aggregate formation was attained for MEH-PBI. Its organic solutions were studied in the same cell system in the cryostat and with the same laser power as for the aqueous MEG-PBI. Moreover, the absorption spectrum was monitored before and after each experiment in order to check for conformational changes and sample degradation. Frequency calibration of all the spectra was accomplished with the use of cyclohexane. MATLAB and ORIGIN were used for spectral treatment and analysis.

Figure 3-6 Image of the custom cryocell with aqueous MEG-PBI solutions at RT (left) and 313 K (right).

3.1.2.2 SRS/IRS

3.1.2.2.1 Theoretical background

Stimulated (SRS) and inverse (IRS) Raman spectroscopy are non-linear spectroscopic techniques that can be employed to produce optical gains or losses as a Raman footprint, in the case for example of very fluorescent samples.[9,10] The Raman scattering effect as described above happens spontaneously: incoming photons are instantaneously scattered by the material in an incoherent way, i.e., not in phase and in all directions. Alternatively, SRS and IRS can take place when deliberately injecting Stokes (red-shifted) and anti-Stokes (blue-shifted) photons together with pump photons in order to increase the total Raman-scattering rate, beyond that of spontaneous Raman scattering: in the case of SRS, pump photons are converted more rapidly into additional Stokes photons, generating peaks upon a supercontinuum spectrum. **Figure 3-7** depicts the non-linear photon conversion process for both cases.

The inverse Raman effect was first noted by W.J.Jones and B.P. Stoicheff.[11] As SRS, IRS is a pump-probe technique and it requires a proper Raman peak intensity to be employed with a sufficient signal-to-noise, so that the outcome signal is appreciable.

This technique produces a practical and robust signal which is markedly desirable in switching applications, important in high-speed signal processing and telecommunication networks. In this process, a material is simultaneously irradiated by intense monochromatic
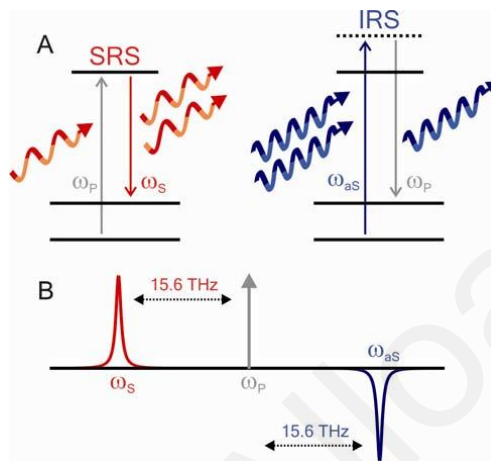
Figure 3-7 IRS and SRS are corollary processes arising in Raman scattering. A) SRS: Stokes photons amplified at expense of pump. IRS: anti-Stokes photons absorbed, transferring energy to pump. B) Red-shifted SRS gain line and blue-shifted IRS loss line from the pump position.[9]

light of frequency v_L and a whitelight continuum; the light can be scattered either from the monochromatic beam at v_L to the continuum at v_L+v_M, or from the continuum at v_L+v_M to the monochromatic beam at v_L, where v_M is a Raman frequency of the material. The continuum pulse provides all the Stokes or anti-stokes photons for the stimulated process. In the IRS process, light on the blue side of the excitation beam is attenuated in the presence of an intense pump (losses in this case are recorded on a whitelight continuum), opposite to the stronger Stokes gain happening for the SRS.[12–15] Essentially SRS and IRS behave as amplifier and attenuator of Raman radiation.

Supercontinuum generation occurs when a collection of nonlinear processes sum together in a smooth spectral continuum upon a pump beam (next section will provide more details on this process). Spectral broadening of the original pump beam occurs by channeling the beam through a strongly non-linear device e.g. a microstructured optical fiber, with a waveguide structure which ensures a high beam quality.[16–19]

An example of the response expected from such an IRS experiment is presented for β-carotene in **Figure 3-8**: on top of a supercontinuum, negative peaks obtained upon interaction with a Raman pump represent the outcome signal. This method has the advantage to provide a Raman fingerprint free from the strong fluorescence that overwhelms the Raman signal in fluorescent samples, once the supercontinuum background is subtracted.
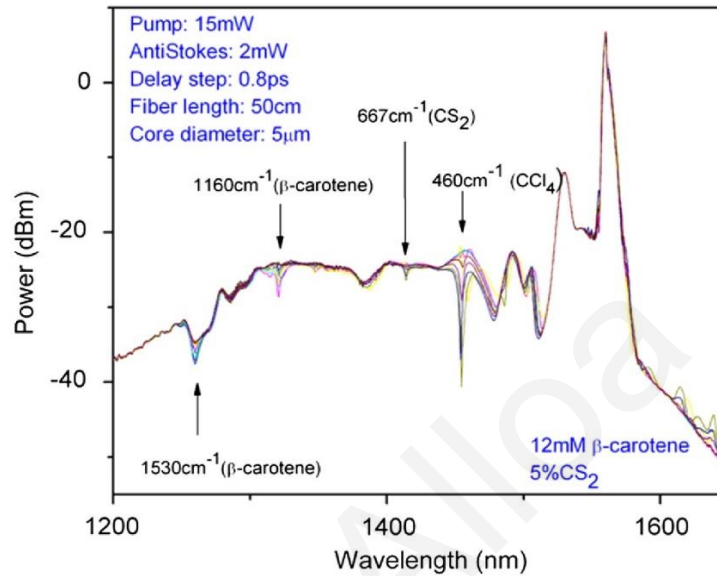
Figure 3-8 Inverse Raman signal for β-carotene dissolved in CCl₄ and 5% CS₂ by volume.[20]

3.1.2.2.2 Optical fibers: supercontinuum generation

The study of the process of generation of new frequency components was initiated around the early 1960s, when Franken et al.[64] for the first time could demonstrate second harmonic generation of light.[65] From that time on, advances in the field lead to the development of the continuum generation process, which occurs when narrow-band incident pulses undergo nonlinear spectral broadening to produce a broadband spectrum, sometimes leading to a whitelight continuous output.[18,23] Supercontinuum generation started in the late 1990s with an innovation in the generation of ultrabroad bands which contributed as well to the advent of a new type of optical waveguides in the form of the photonic crystal fiber (PCF). Such optical improvements found uses in many fields, as non-linear devices, in fiber optic telecommunication, for supercontinuum generation, for sensing technology, etc.[24,25] In this class of optical fibers, light is trapped inside a hollow fiber core by creating a periodic lattice of microscopic holes in the cladding glass.

When high-energy, ultrashort pulses travel throughout a material, their frequency spectrum can experience massive broadening due to a range of interrelated non-linear effects, i.e. a

combination of Raman and Kerr effects.[24,26–28] The successful realization of microstructured optical fibers depends on the use of complex air/glass structures within the fiber cross-section. Most photonic crystal fibers have been fabricated with a cladding surrounding a core lattice of air holes in a silica medium (a cross-section is depicted in **Figure 3-9**, left). In the same Figure (right), generation of whitelight through a PCF is presented, with a special pattern due to the inner configuration of the fiber core. In a solid-core PCF the pattern of air holes acts like a filter. Indeed, as light is evanescent in the air, the holes act as strong barriers. A very important concept in fiber optics is that of waveguide modes; these are field configurations which maintain their intensity profile during propagation, apart from possible power losses. A fundamental mode is unable to escape because it cannot fit in the gaps between the air holes, as its effective wavelength in the transverse plane is too large. Higher order modes are able to leak away because the transverse effective wavelength is smaller. If the diameter of the air holes is increased, the gaps between them shrink and more and more higher order modes are trapped. Considering the whitelight continuum passing throughout the fiber, each frequency interacts its own way with each mode and it coherently adds up with the rest of the radiation. Correct choice of geometry thus guarantees that only the fundamental mode appears.[26,29]
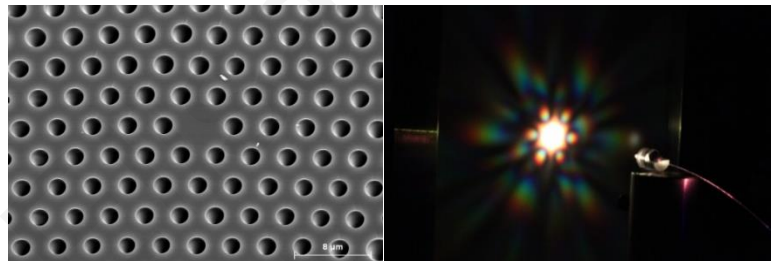
Figure 3-9 Left. SEM micrographs of a photonic-crystal fiber. Important for the light conversion is the diameter of the solid core at the center of the fiber and the diameter of the holes. **Right**. Supercontinuum-generated light exiting from the fiber.

3.1.2.2.3 Experimental details

Nanosecond/picosecond pulses and photonic fibers are used for whitelight continuum generation. Pulses at 532 and 1064 nm were pumped throughout the fiber, singularly or simultaneously, in order to generate the supercontinuum and to have a light component to act as a probe beam. Pump and probe should be synchronized in time and space at the sample (**Figure 3-10**). Gains or losses can then be monitored in the spectrum, obtaining, respectively, the stimulated or inverse Raman.
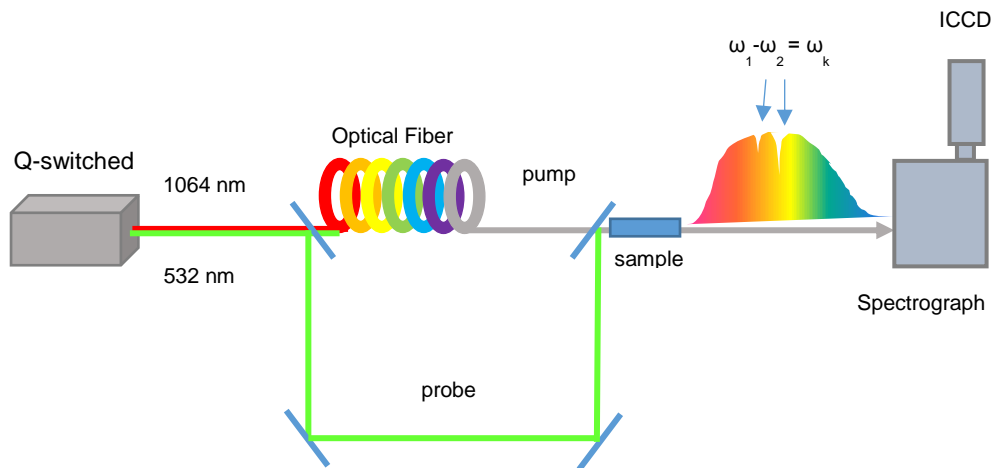
Figure 3-10 Stimulated/Inverse Raman setup.

A collaboration with the University of Valencia was established in order to obtain appropriate optical fibers to generate the supercontinuum light, which acts as the probe pulse in SRS or IRS. A pump is accordingly coupled and synchronized with the probe in time and space. The setup employed at the University of Valencia (see **Figure 3-11**) for the supercontinuum generation consisted of:

1. Laser (700 ps, 1064 nm)

2. Two mirrors and the corresponding adjustable mirror mounts

3. 3-axes flexural stage

4. A platform to support the fiber and the fiber holder

5. Aspheric lenses with different numerical apertures (NA)

More specifically, supercontinuum laser light was generated by coupling the 1064 nm laser beam into an optical fiber, responsible for this conversion to white light. The laser power employed was ~10 mW, depending on the fiber. Different optical fibers were tested in order to choose the most appropriate one, i.e. with the widest possible conversion wavelength range. The same setup tested at the University of Valencia was used at the University of Cyprus (, below), with the difference that 2 ns pulsed beams at 532 and 1064 nm were employed with a beam power ranging from 1 to 70 mW.
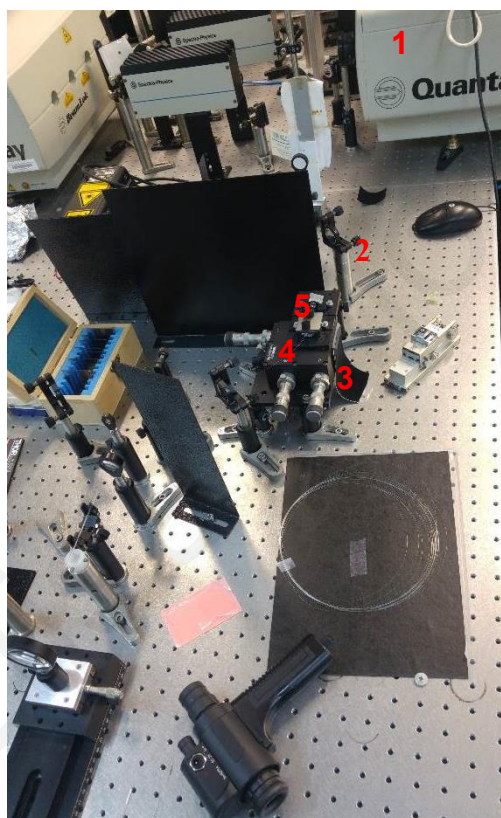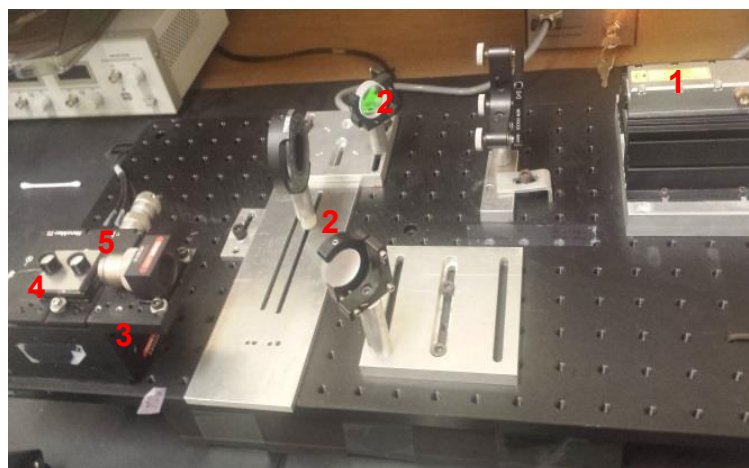
Figure 3-11 Supercontinuum light generation setup (top) University of Valencia; (bottom) University of Cyprus. The setup consists of: 1) Laser. 2) Mirrors. 3) 3-axes flexural stage 4) Fiber holder. 5) Aspheric lenses.

3.1.2.3 FSRS

3.1.2.3.1 Theoretical background

The investigation on oligofluorenes was performed through Femtosecond stimulated Raman spectroscopy (FSRS) in order to gain understanding of the conformational changes occurring in the excited state at very early times following excitation.[30]

After photoexcitation with sufficient energy, any material experiences an excess of vibrational energy, which is transferred to the environment by a relaxation process of its excited energetic state (called vibrational cooling).[31] According to the Franck-Condon principle, electronic transitions are vertical, which means that none of the nuclei in the structure moves initially. Nuclear displacements following excitation results in an experimentally observed spectral shift in the fluorescence spectrum. The difference between the ground and the excited state geometry leads to a conformational rearrangement (associated to a sometimes pronounced spectral shift), which is particularly evident for instance in highly twisted structural conformations. In conjugated polymers, a torsional relaxation may consequently lead to a planarization of the structure.[32,33] This process is associated to exciton delocalization along the chain.[34] Monitoring specific mode frequencies i.e. the C-C / C=C stretching[35] throughout the torsional dihedral angle or ring breathing provides information on the planarity of the system achieved in the process of excited-state relaxation.[36–38] The complementary process to the energetic relaxation towards a more ordered structure is exciton migration between localized energetic sites;[39,40] the overall time scale of the relaxation process depends on the exciton migration mechanism and eventual self-trapping effects due to material defects.[36] This overall process happens on a sub-picosecond scale; a range in which FSRS is a sensitive technique. FSRS is a nonlinear optical
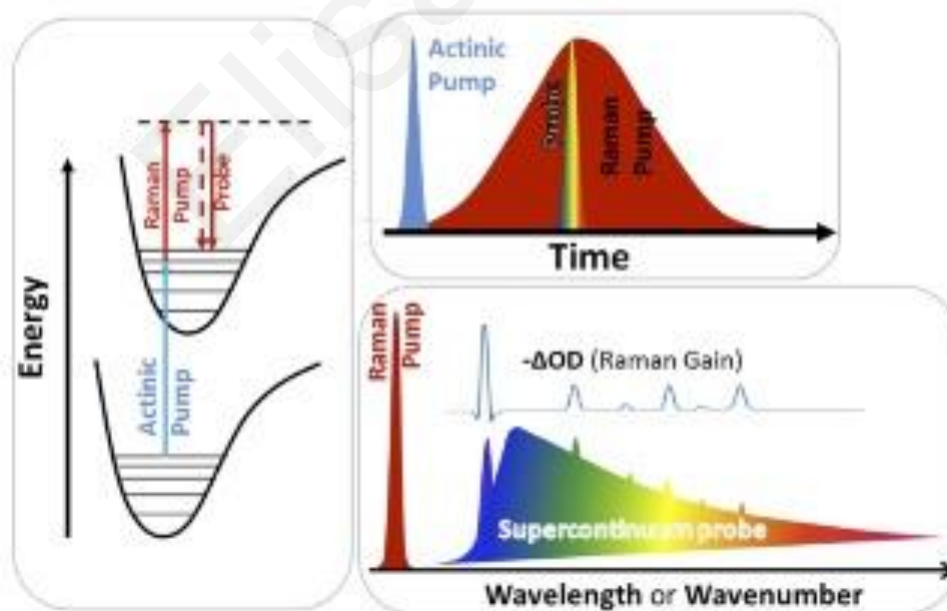
Figure 3-12 Conceptual sketchs of an FSRS experiment, in function of energy (left), time (up right) and wavelength (down right).

technique capable to provide vibrational structural information with simultaneously high temporal (sub-50 fs) precision and high spectral ($\sim$15 cm^{-1}) resolution. **Figure 3-12** depicts the theoretical representation of the combination of pulses used in order to achieve the FSRS process: an actinic pump initiates the photoexcitation, by promoting the system to an excited electronic state. Subsequently a Raman pump and Raman probe monitor the structural evolution of the system driving stimulated Raman transitions. The Raman pump is a narrow-bandwidth, picosecond pulse, whereas the probe is a broadband femtosecond continuum pulse. When both pulses are overlapped spatially and temporally in a Raman-active medium, photons are transferred from the high-intensity Raman pump to the weak probe pulse at the vibrational resonances of the sample.[30,34,41]

3.1.2.3.2 Experimental details

Oligofluorene samples were circulated through a 340 μm pathlength CaF$_2$ window rastered Harrick cell during spectroscopic measurements; oligofluorenes solutions were introduced into the flow circuit under air-free conditions. Although relatively high concentrations was used for the FSRS measurements ($\sim$0.2 mg/mL), it was verified that the TA spectral dynamics of these samples were identical to those measured at ten times lower concentration; this suggests that Raman measurements described here should not be affected by aggregation of the material studied. This is confirmed by Dynamic Light Scattering experiments that show that at this concentration we are in the dilute solution regime.[42] Laser pulses for these experiments were derived from the fundamental output of a dual 10-kHz chirped pulse amplified Ti:sapphire laser system (Thales Laser). The photoexcitation pulses at 350 nm were generated using an optical parameteric amplifier (OPA) and were attenuated to 0.6 μJ/pulse. Narrowband (10-15 cm^{-1}) picosecond pulses ($\sim$1.5-ps duration) centered at 750 nm were generated with a picosecond OPA. The Raman pump pulse energy was typically 0.11 μJ/pulse. Near-IR white-light probe continuum was generated by focusing $\sim$ 1 μJ of the signal output from an OPA at 1300 nm into a 2 mm-thick sapphire window.

The actinic pump, Raman pump and probe beams were focused into the sample cell using 10-cm-focal-length fused silica lenses with typical beam diameters of 50 μm (probe) and 100 μm (pump) set in a non-collinear geometry with an angle of $\sim$10$^{\text{o}}$ between the IR and UV pump beams and the probe. Excitation and Raman pump pulses were blocked after the sample with a set of long-pass filters, and probe light was collected and dispersed with a 250 mm f/4 spectrograph (DK240, Spectral Products)) onto a 512-element silicon array detector (Quantum Detectors, QD). The camera was configured to collect spectra at the laser's 10

kHz repetition rate, with the Raman and photoexcitation beam synchronously chopped at 2.5 and 5 kHz, respectively. Ground state stimulated Raman, transient absorption (TA) and transient stimulated Raman spectra were then calculated from 4 consecutive probe spectra. Each Raman spectrum presented is an average of 17,000 of these on/off ratios. TA measurements were made using a low-resolution grating (150 grooves/mm). In contrast, Raman spectra were collected at much higher resolution, using a 600 grooves/mm grating, limited by the ~ 15 cm^{-1} bandwidth of the ps-OPA, as well as natural spectral linewidths, spectral congestion, and spectral inhomogeneity. The photoexcitation pulse delay relative to the Raman pump−probe pulse pair was controlled with a motorized translation stage outfitted with a corner-cube mirror. The relative timing between the Raman pump and probe pulses was optimized according to the spectral shapes of nonresonant features from the solvent but also to minimize Raman-pump-induced depletion of the excited-state population. Polarizations of all three pulses were kept parallel in the measurements presented here.[43] MATLAB and ORIGIN were used for spectral treatment and kinetics studies.

3.2 Computational methods

Structural optimization of MEG-PBI was carried out on its methylated precursor obtained by replacing the twelve glycol chain units with methoxy groups. The structural optimization was performed with Density Functional Theory (DFT) calculations at the B3LYP/6-31+G** level of theory utilizing the Gaussian16[44] program package. All the calculations were carried out in the gas phase. Calculated IR and Raman spectra, as well as the electronic properties and HOMO–LUMO energies, were obtained at the same level of theory. For simplicity, absorption wavelengths and oscillator strengths were calculated on the MEG-PBI precursor, obtained after removing the tris-(methoxytriethyleneglycol) gallate units. The calculations were carried out using time-dependent DFT (TD-DFT)[45,46] with the B3LYP functional and the 6-31(d,p) basis set,[41,42] based on the optimized structure in the gas phase. The structures were rendered with the UCSF Chimera package. Chimera is developed by the Resource for Biocomputing, Visualization, and Informatics at the University of California, San Francisco (supported by NIGMS P41-GM103311).[47] The nature of the electronic excitations was explored by extracting natural transition orbitals[48] (NTO) from the Gaussian16 check point files using the Multiwfn software.[49] These calculations are reported in *Appendix A*.

References

1.   Herbst, S., Soberats, B., Leowanawat, P., Lehmann, M. & Würthner, F. A columnar liquid-crystal phase formed by hydrogen-bonded perylene bisimide J-aggregates. *Angew. Chemie - Int. Ed.* **56,** 2162–2165 (2017).

2.   Grande, V., Soberats, B., Herbst, S., Stepanenko, V. & Würthner, F. Hydrogen-bonded perylene bisimide J-aggregate aqua material. *Chem. Sci.* **9,** 6904–6911 (2018).

3.   Alloisio, M. *et al.* Enhanced and reproducible photogeneration of blue poly(pentacosadiacetylene) chemisorbed onto silver nanoparticles: An optimized synthetic protocol. *Mater. Chem. Phys.* **147,** 293–303 (2014).

4.   Alloisio, M. *et al.* Synthesis of fluorescent core-shell metal nanohybrids: A versatile approach. *Materials (Basel).* **9,** 417–425 (2016).

5.   Landsberg, G. & Mandelstam, L. Eine neue erscheinung bei der lichtzerstreuung in krystallen. *Naturwissenschaften* **16,** 557–558 (1928).

6.   Raman, C. V. & Krishnan, K. S. A new type of secondary radiation. *Nature* **121,** 501–502 (1928).

7.   Myers, A. B. Resonance Raman intensities and charge-transfer reorganization energies. *Chem. Rev.* **96,** 911–926 (1996).

8.   Myers, A. B. *et al.* Absolute resonance Raman intensities demonstrate that the spectral broadening induced by the β-ionone ring in retinal is homogeneous. *J. Chem. Phys.* **84,** 633–640 (1986).

9.   Solli, D. R., Koonath, P. & Jalali, B. Inverse Raman scattering in silicon: A free-carrier enhanced effect. *Phys. Rev. A - At. Mol. Opt. Phys.* **79,** 1–4 (2009).

10.   Kieu, K. *et al.* Demonstration of Zeno switching through inverse Raman scattering in an optical fiber. *Opt. Express* **19,** 12532 (2011).

11.   Jones, W. J. & Stoicheff, B. P. *Inverse raman spectra: Induced absorption at optical frequencies*. *Physical Review Letters* **13,** (1964).

12.   James Hughes Jr, L. The inverse Raman effect : applications and detection techniques. 1–37 (1980).

13. Yeung, E. S. Inverse Raman effect: A quantitative spectroscopic technique. *J. Mol. Spectrosc.* **53,** 379–392 (1974).

14. Qiu, X. *et al.* Inverse Raman bands in ultrafast Raman loss spectroscopy Inverse Raman bands in ultrafast Raman loss spectroscopy. *J. Chem. Phys.* **164502,** 1–7 (2014).

15. Aloi, A. & Tommasi, R. Inverse Raman scattering in femtosecond broadband transient absorption experiments. *Raman Spectrosc. Appl.* 270–290 (2017).

16. Kinney, J. B. & Staley, R. H. Applications of Photoacoustic Spectroscopy. *Annu. Rev. Mater. Sci.* **12,** 295–321 (1982).

17. Kieu, K., Jones, R. J. & Peyghambarian, N. Generation of few-cycle pulses from an amplified carbon nanotube mode-locked fiber laser system. *IEEE Photonics Technol. Lett.* **22,** 1521–1523 (2010).

18. Dudley, J. M., Genty, G. & Coen, S. Fibre supercontinuum generation overview. *Supercontinuum Gener. Opt. Fibers* **4,** 52–61 (2010).

19. Verlag, S. & Laubereau, A. Non-linear Raman spectroscopy and its chemical applications. *D. Reidel Publ. Co.* **93,** 83–183 (1982).

20. Kieu, K. *et al.* All-optical switching based on inverse Raman scattering in liquid-core optical fibers. *Opt. Lett.* **37,** 942–944 (2012).

21. Bloembergen, N. Nonlinear optics: Past, present, and future. *IEEE J. Quantum Electron.* **6,** 876–880 (2000).

22. Franken, P. A., Hill, A. E., Peters, C. W. & Weinreich, G. Generation of optical harmonics. *Phys. Rev. Lett.* **7,** 118–119 (1961).

23. Dudley, J. M. Supercontinuum generation in photonic crystal fiber fundamentals to applications. *Conf. Opt. Fiber Commun. Fiber Opt. Eng. Conf.* **78,** 1135–1184 (2008).

24. Wadsworth, W., Knight, J. & Birks, T. State-of-the-art photonic crystal fiber. *Opt. Photonics News* **23,** 24 (2012).

25. Ranka, J. K., Windeler, R. S. & Stentz, A. J. Visible continuum generation in air–silica microstructure optical fibers with anomalous dispersion at 800 nm. *Opt. Lett.* **25,** 25 (2000).

26.   Benabid, F., Knight, J. C., Antonopoulos, G. & Russell, P. S. J. Stimulated Raman scattering in hydrogen-filled hollow-core photonic crystal fiber. *Science (80-.).* **298,** 399–402 (2002).

27.   Wadsworth, W. J. *et al.* Supercontinuum and four-wave mixing with Q-switched pulses in endlessly single-mode photonic crystal fibres. *Opt. Express* **12,** 299 (2004).

28.   Russell, P. S. J. Photonic-crystal fibers. *J. Light. Technol.* **24,** 4729–4749 (2006).

29.   Kuhlmey, B., Renversez, G. & Maystre, D. Chromatic dispersion and losses of microstructured optical fibers. *Appl. Opt.* **42,** 634 (2003).

30.   Mathies, R. A. Femtosecond stimulated Raman spectroscopy. *Opt. InfoBase Conf. Pap.* **58,** 461–88 (2007).

31.   Ling, S., Schumacher, S., Galbraith, I. & Paterson, M. J. Excited-state absorption of conjugated polymers in the near-infrared and visible: A computational study of oligofluorenes. *J. Phys. Chem. C* **117,** 6889–6895 (2013).

32.   Park, K. H., Kim, W., Yang, J. & Kim, D. Excited-state structural relaxation and exciton delocalization dynamics in linear and cyclic p-conjugated oligothiophenes. *Chem. Soc. Rev* **47,** 4279 (2018).

33.   Franco, I. & Tretiak, S. Electron-vibrational dynamics of photoexcited polyfluorenes. *J. Am. Chem. Soc.* **126,** 12130–12140 (2004).

34.   Yu, W., Zhou, J. & Bragg, A. E. Exciton Conformational Dynamics of Poly(3-hexylthiophene) (P3HT) in Solution from Time-Resolved Resonant-Raman Spectroscopy. *J. Phys. Chem. Lett.* **3,** 1321–1328 (2012).

35.   Zhou, J., Yu, W. & Bragg, A. E. Structural relaxation of photoexcited quaterthiophenes probed with vibrational specificity. *J. Phys. Chem. Lett.* **6,** 3496–3502 (2015).

36.   Magnanelli, T. J. & Bragg, A. E. Time-resolved raman spectroscopy of polaron pair formation in poly(3-hexylthiophene) aggregates. *J. Phys. Chem. Lett.* **6,** 438–445 (2015).

37.   Rhinehart, J. M., Mehlenbacher, R. D. & McCamant, D. Probing the charge transfer reaction coordinate of 4-(dimethylamino) benzonitrile with femtosecond stimulated raman spectroscopy. *J. Phys. Chem. B* **114,** 14646–14656 (2010).

38. Rhinehart, J. M., Challa, J. R. & McCamant, D. W. Multimode charge-transfer dynamics of 4-(Dimethylamino)benzonitrile probed with ultraviolet femtosecond stimulated Raman spectroscopy. *J. Phys. Chem. B* **116,** 10522–10534 (2012).

39. Bragg, A. E., Yu, W., Zhou, J. & Magnanelli, T. Ultrafast Raman spectroscopy as a probe of local structure and dynamics in photoexcited conjugated materials. *J. Phys. Chem. Lett.* **7,** 3990–4000 (2016).

40. Hintschich, S. I., Dias, F. B. & Monkman, A. P. Dynamics of conformational relaxation in photoexcited oligofluorenes and polyfluorene. *Phys. Rev. B - Condens. Matter Mater. Phys.* **74,** 1–10 (2006).

41. Dietze, D. R. & Mathies, R. A. Femtosecond stimulated Raman spectroscopy. *ChemPhysChem* **17,** 1224–1251 (2016).

42. Somma, E., Loppinet, B., Chi, C., Fytas, G. & Wegner, G. Static and dynamic solution properties of monodisperse oligofluorenes. *Phys. Chem. Chem. Phys.* **8,** 2773–2778 (2006).

43. Greetham, G. M. *et al. ULTRA: A unique instrument for time-resolved spectroscopy. Applied Spectroscopy* **64,** (2010).

44. Frisch, M. J. *et al. Gaussian 09.* (2009).

45. Runge, E. & Gross, E. K. U. Density-functional theory for time-dependent systems. *Phys. Rev. Lett.* **52,** 997–1000 (1984).

46. Bauernschmitt, R. & Ahlrichs, R. Treatment of electronic excitations within the adiabatic approximation of time dependent density functional theory. *Chem. Phys. Lett.* **256,** 454–464 (1996).

47. Pettersen, E. F. *et al.* UCSF Chimera - A visualization system for exploratory research and analysis. *J. Comput. Chem.* **25,** 1605–1612 (2004).

48. Martin, R. L. Natural transition orbitals. *J. Chem. Phys.* **118,** 4775–4777 (2003).

49. Lu, T. & Chen, F. Multiwfn: A multifunctional wavefunction analyzer. *J. Comput. Chem.* **33,** 580–592 (2012).

CHAPTER 4

RR study of the J-type aggregation process of a water-soluble PBI

4.1 Introduction

Perylene tetracarboxylic acid bisimides, in short perylene bisimides (PBI), are a highly interesting class of dyes for J-aggregates, with very promising functional properties, which were recently exploited in all-polymer photonic microcavities.[1] The elaboration of water-soluble PBI-based aggregate systems via self-assembly evolved as a promising research avenue because of its possible exploitation in biological systems. In the most recent research of Würthner's group, PBI J-aggregates could be formed by hydrogen-bonded self-assembly in water, which was quite surprising if we consider that water is a very competitive solvent for the self-complementary hydrogen bonding between the imide units of the PBIs.[2] Interestingly, however, these hydrogen-bonded self-assembled nanofibers with J-type coupling and fluorescence properties only occurred at elevated temperature, obviously driven by entropy from the less ordered PBI room temperature hydrogel material. This chemical system has been named "aquamaterial"[3,4] because of its capability to behave as a hydrogel-like material with unique and useful properties: the red-to-blue color transition appears indeed to be exploitable in the development of cutting-edge applications e.g. as photonic material in microcavities or as lyotropic liquid crystals. Its unique properties primarily derive from its large extended π-systems, together with its various supramolecular aggregate-based architectures.[5] H-bonded aggregation driven by self-complementary free-imide groups has also been reported to promote alternative J-type aggregate formation in non-polar solvents.[6] Thanks to non-covalent connectivity, such PBIs form very sophisticated supramolecular fibers, enabling interesting photophysics involving exciton coherence and migration.[7] More specifically, hydrogen-bond donors/acceptors and π–π interaction were employed for the design of these functional PBI chromophores with such unique spectroscopic properties: the synergy of these forces lead to a supramolecular assembly of the monomers in a wired

structure with a face-to-face arrangement, typical of a mixed J/H aggregate.[8] Double/triple-stranded aggregates are thus formed by elongating π–π stacked units, where their building blocks are aligned with a translational offset.[9,10] The water-soluble PBI depending on the excitonic coupling extent, forms an aggregate structure with a monomer-like UV/Vis spectrum at room temperature, where the units exhibit a cofacial arrangement with weak H-type coupling, or a slipped packing with J-type coupling when the temperature increases, with fluorescence in the far-red.[2]
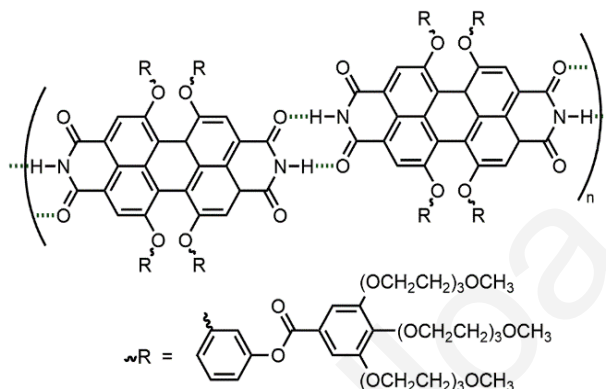
Figure 4-1 Structure of the water-soluble perylene bisimide. J-aggregates are formed upon hydrogen bonding of the imide N-H of one molecule to the C=O of a neighboring one. Bottom: The side chains "R" attached to the main PBI core.

The present work focuses on a water-soluble PBI molecule designed to self-assemble via hydrogen bonding (see **Figure 4-1**) and π–π interactions into a supramolecular J-aggregated structure. A comparison with a PBI counterpart having solubility in organic media has been also performed in order to compare findings and will be analyzed in *Chapter 5*. RR spectroscopy was employed here to investigate in detail the ground state conformation of these perylene bisimide (PBI) systems. In order to provide a complete insight in the structure and the role of hydrogen bonding in the self-assembly, the selectivity of resonance Raman was exploited to elucidate the contribution of specific chromophores through excitation in the UV and visible spectral region. Our results indicate that the supramolecular structure of the water-soluble PBI studied undergoes a change in its aggregation pattern, showing an elongation along the main fiber axis at higher temperatures, resulting in a J-aggregated nanofiber, confirming the involvement of hydrogen bonding.

4.2 Results and discussion

The temperature-dependent optical response of MEG-PBI is presented in **Figure 4-2**. The absorption spectra for MEG-PBI in water at RT and 313 K correspond to the monomer-like state and the J-type supramolecular assembly, respectively, with the latter showing a large bathochromic shift from 563 nm for the 0-0 peak to 633 nm, as usually observed for J-aggregates.

Temperature-dependent Resonance Raman (RR) spectroscopy was employed for the structural characterization of PBI in these two different molecular states. A range of excitation wavelengths were chosen as indicated in the figure in order to observe the involvement of various chromophores in the supramolecular assembly. Excitation in the visible range corresponds to absorption due to the perylene core (according to the DFT computational study in the *Appendix*, **Figure 10-1, Table 10-1** and **10-2**), while excitation in the UV probes the phenyl rings and the bisimide groups on the PBI.[6] Monitoring any spectral changes on resonance with the side-chains can provide insights in their participation in the aggregation process, while on resonance with the perylene core
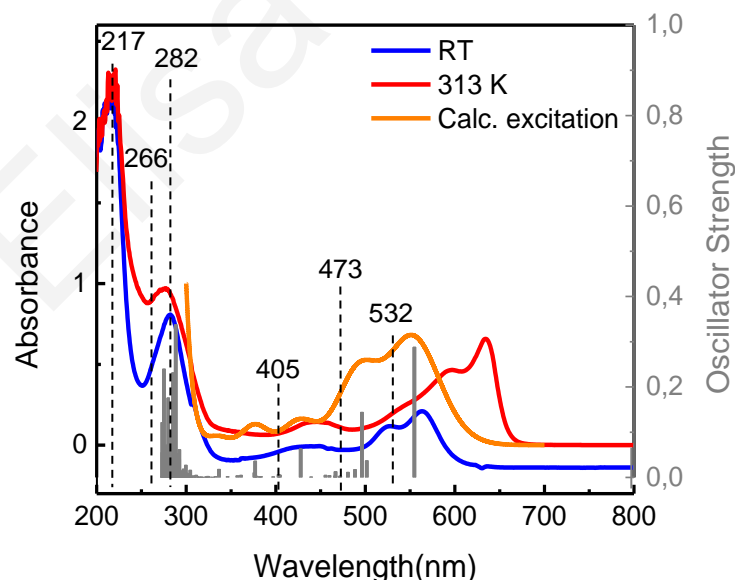
Figure 4-2 UV-vis spectrum of MEG-PBI in aqueous solution as a function of temperature. TD-DFT calculated transitions are shown in vertical grey lines, with the right scale indicating their oscillator strength. The overall calculated spectrum is shown in orange, while the black dashed lines indicate the excitation wavelengths used for the resonance Raman measurements.

structure and its associated bisimide, one can assess the extent of hydrogen bonding and its impact on the core structure. The bisimide group skeleton resembles the structure found in nucleobases (thymine and uracil) that absorb in the UV with bands around 210 n m and 260 nm that can be assigned to π-π* transitions.[11,12] Excitations at 217, 266 and 282 nm probe phenyl rings both in the perylene core and in its side chains, however, in variable proportion.

4.2.1 Visible RR in water

The normalized RR spectra of the MEG-PBI monomer and aggregate conformations in aqueous solution and in thin films acquired at 532 nm are presented in **Figure 4-3**. Even though similar spectra are observed for the two states, distinct differences are observed that provide some insight on the structure of the aggregate. Specifically, a 7 cm^{-1} downshift is observed for the 1359 cm^{-1} and 1557 cm^{-1} bands upon aggregation, while the bands at 1395 cm^{-1} and 1598 cm^{-1} show an upshift. The band at 1447 cm^{-1} remains unchanged at the two different temperatures. RR spectra of MEG-PBI aggregates in thin films are in full agreement with the spectrum displayed by MEG-PBI aggregates in solution.
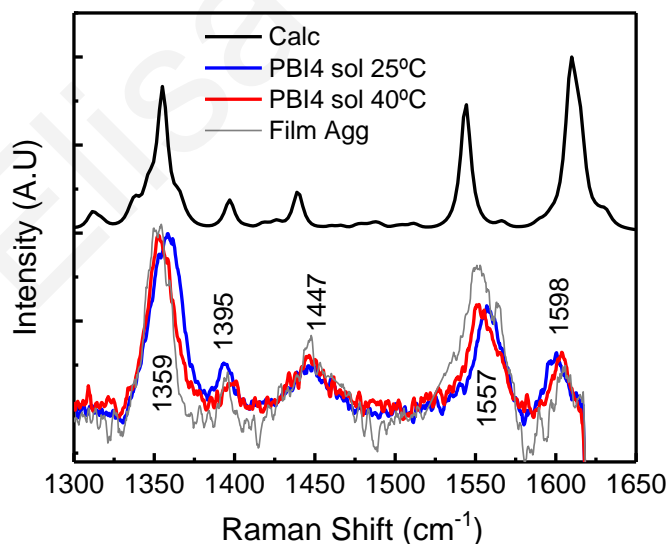
Figure 4-3 Top: Calculated Raman spectrum of MEG-PBI in vacuum (scale factor *0.97). Bottom: Resonance Raman spectra of MEG-PBI in aqueous solution at RT (monomer-like) and 313 K (aggregate) and in a thin film with excitation at 532 nm.

Computation of the normal modes of MEG-PBI provided insights on the structure of the aggregate through correlation of the varied vibrational fingerprint upon aggregation to specific structural changes (**Figure 4-4** and **Table 4-1**). The

Table 4-1 Experimental and calculated Raman frequencies (cm^{-1}), λ_{exc} = 532 nm.

EXP		CALC (vacuum)	Assignment of PBI core vibrations†
Monomer-like	J-Aggr		
1359	1352	1383	$v_{C=C}$ ‖ to N-N axis
1395	1398	1425	ip δ_{C-H} / $v_{C=C}$ ⊥ to N-N axis
1447	1447	1467	s $v_{C=C}$ (central ring)
1557	1550	1575	$v_{C=C}$ ‖ N-N axis
1598	1603	1643	ip δ_{C-H} / $v_{C=C}$ ⊥ to N-N axis
1706	1706	1791	$v_{C=O}$ (free C=O)
†v: stretch, δ: bend, ip: in-plane, s: symmetric, ‖: parallel, ⊥: perpendicular			
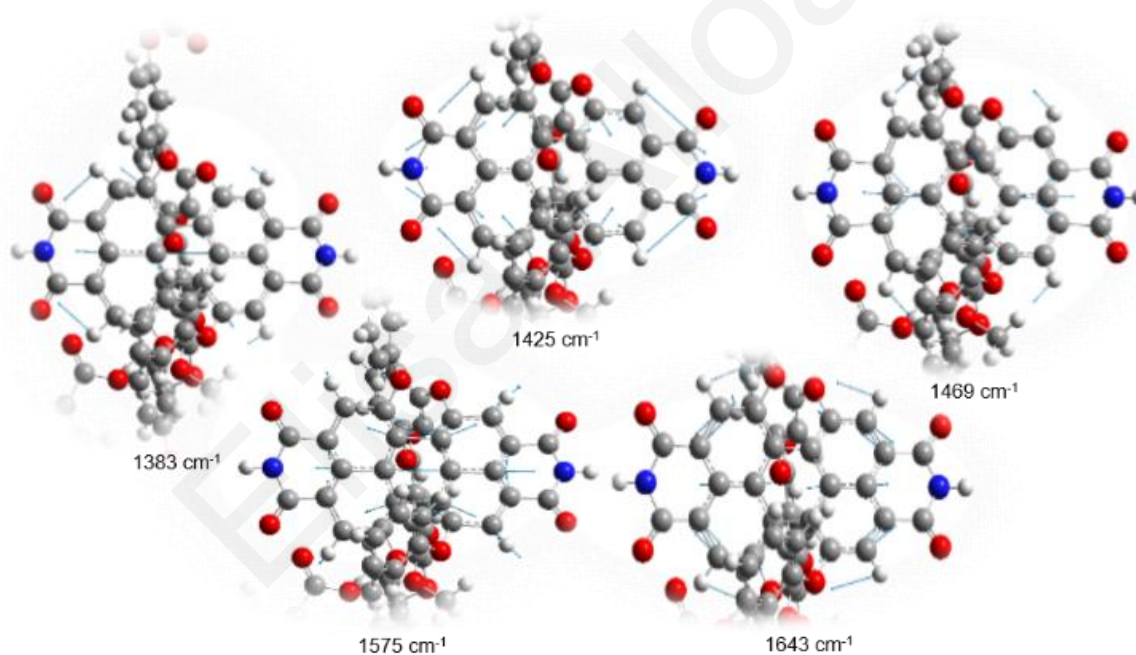
Figure 4-4 Calculated vibrational normal modes for MEG-PBI. The blue arrows denote the displacement vectors.

experimental spectrum of the monomer-like state is well reproduced by the computation, which considers the molecule in vacuum, with the observed bands corresponding to vibrational modes of the perylene core. The bands at ~1355 cm^{-1} and ~1555 cm^{-1} are assigned to C=C stretching along the long axis of the perylene (the N-N axis, see **Figure 4-4**), while the bands at ~1395 cm^{-1} and ~1600 cm^{-1} are associated with C=C stretching perpendicular to the N-N axis and along the periphery of the core in combination with in-plane C-H bending. The band at 1447 cm^{-1}

corresponds to C=C stretching involving the central aromatic ring, where the perylene is twisted. Based on this evidence, a distortion of the perylene core upon aggregation can be proposed, where the bonds along the perylene long axis lengthen and the ones perpendicular to that shorten, with elongation parallel to the N-N axis, likely induced by hydrogen bonding of the imide protons with carbonyls from neighboring molecules, resulting in a head-to-tail arrangement. Overlap of the N-H stretch with the strong O-H stretching bands of water in the high frequency region made direct observation of hydrogen bonding effects difficult.
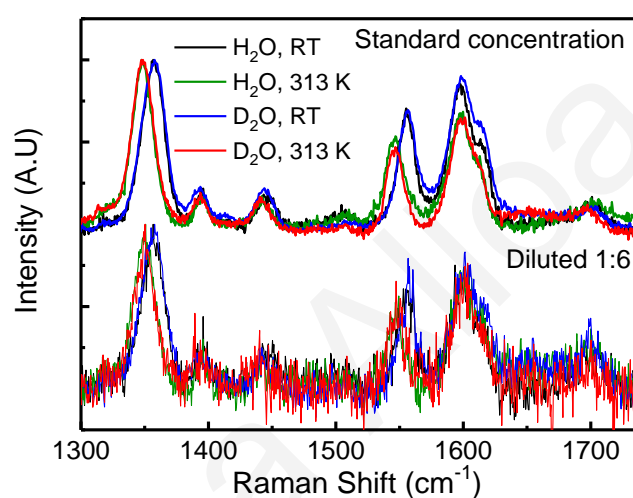
Figure 4-5 RR spectra of MEG-PBI as a function of concentration and temperature with excitation at 473 nm. The comparison is between the standard solution concentration (62.5 uM) and a 1:6 diluted one. RR spectra are also shown for MEG-PBI in deuterated water.

In order to assess whether the chosen concentration affects the aggregation process and whether an entirely monomeric state could be possible with a less close packing of the units, the temperature-dependent experiment was performed with a 1:6 diluted sample (10 μM) with excitation at 473 nm, again on resonance with the main core of the PBI, where most of the shifts appear due to the elongation of the aggregated supramolecular structure. As **Figure 4-5** clearly shows, even though the spectra are noisier due to a lower signal, the same modes and shifts appear at both concentrations, suggesting that we are dealing with the same conformer as in the 62.5 μM concentrated sample and that a monomer-like state can be hypothesized even for the concentrated solution at low temperature. A difference in the relative intensities for

the ~1555 and ~1600 cm^{-1} modes, along with a slight shift to higher energies and broadening of the 1447 cm^{-1} peak for the monomer at both concentrations, suggests that the nature of this electronic transition differs from that at 532 nm. This observation is in agreement with the finding from the DFT calculations that a second strong electronic transition involving the perylene core exists close to this excitation wavelength (calculated at 485 nm, **Figure 10-1** in the *Appendix*). The experiment was also performed in deuterated water, in order to interrogate the role of the imide N-H proton in the aggregation process[13], which is directly involved in H- bonding to the carbonyl groups of another PBI. The signal resembles the spectra obtained in water, confirming that the vibrations observed are due to C=C stretches in the core, without involvement of the imidic N-H. A 5 cm^{-1} downshift is observed for the 1700 cm^{-1} peak at high-temperature in the deuterated sample (J-aggregated conformation). As shown below, this vibration is associated with the carbonyl bond not involved in H-bonding in the aggregate. In deuterated water, free C=Os of aggregated samples that can hydrogen bond to the solvent vibrate at lower energies, similarly to the case of the C=O band of deoxyribonucleotide d-CMP and d-GMP, with 266 and 218 nm excitation, that downshifts upon deuteration.[14]

The lower frequency region was also investigated with RR spectroscopy in order to monitor the presence of 'out of plane' modes, widely reported in literature as
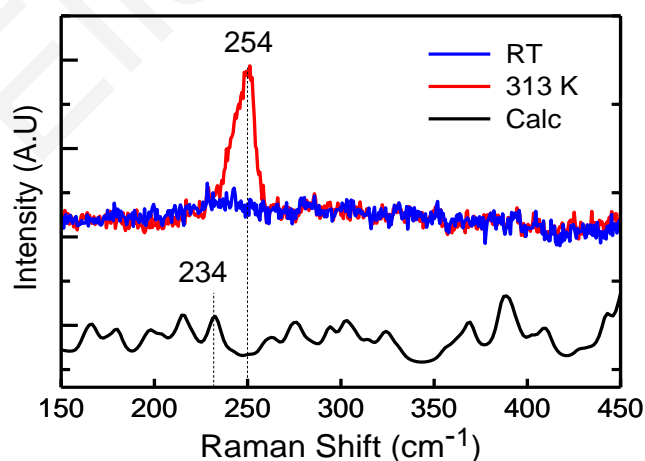
Figure 4-6 Top: Experimental Resonance Raman spectra of MEG-PBI in water solution with excitation at 473 nm in the monomer (blue) and J-aggregate (red) state. **Bottom:** Calculated Raman spectrum of MEG-PBI in vacuum. Dashed lines show the experimental band and the corresponding calculated assignment.

fingerprint of J-aggregation according to the theory of Aggregation-Enhanced Raman

Scattering (AERS).[15]   An intense peak at 254 cm^{-1} is indeed observed in the aggregated state only (**Figure 4-6**) in both solution and film, which corresponds to the out-plane core vibration calculated at 234 cm^{-1}. It is noted in the literature that the significant enhancement of low-frequency modes occurs only when the excitation wavelength is on resonance with the J-aggregate absorption band of the molecule. Moreover, according to the AERS theory, the enhanced peak seen in the low frequency region may be due to π–π stacking among units in the fibers, which is consistent with the supramolecular assembly of MEG-PBI molecules.[16]

4.2.2 UV RR in water and deuterated water

The hydrophobic effect plays a major role in the self-assembly process of MEG-PBI in water, and monitoring N-H bonding of the perylene core imide as well as interactions among the side chains of the supramolecular structure is fundamental. Exploring further excitation wavelengths can help attain this goal. From **Figure 4-7**, showing RR spectra with excitation chosen on resonance with different chromophores in the molecule, it is immediately evident that the peaks in all graphs closely match the calculated Raman spectrum, thus the simulation can provide a good tool for interpretation of results.

It is apparent that different modes are enhanced when the excitation is changed from the visible to the UV, facilitating thus the elucidation of the nature of the different electronic transitions. Specifically, observing the fingerprint region from 1300 to 1700 cm^{1}, one can see that the 1600 cm^{-1} mode is the most prominent band in the UVRR spectra compared to the 1355 cm^{-1} band in the visible. Moreover, the other peaks show a reduced intensity and some disappear, which is a clear sign that the resonance with the main core is reduced in the UV. There is also a perceptible shift in the bands in the visible versus the UVRR spectra; this is an indication that different chromophores are probed. Another clear evidence is the presence of a peak at 1729 cm^{-1}, which, according to the calculations and FT-IR spectra (see below), corresponds to the carbonyl bonds in the esters of the side chains of the molecule. For a detailed description of the observed bands and assignments to the calculated modes see **Table 4-2.**
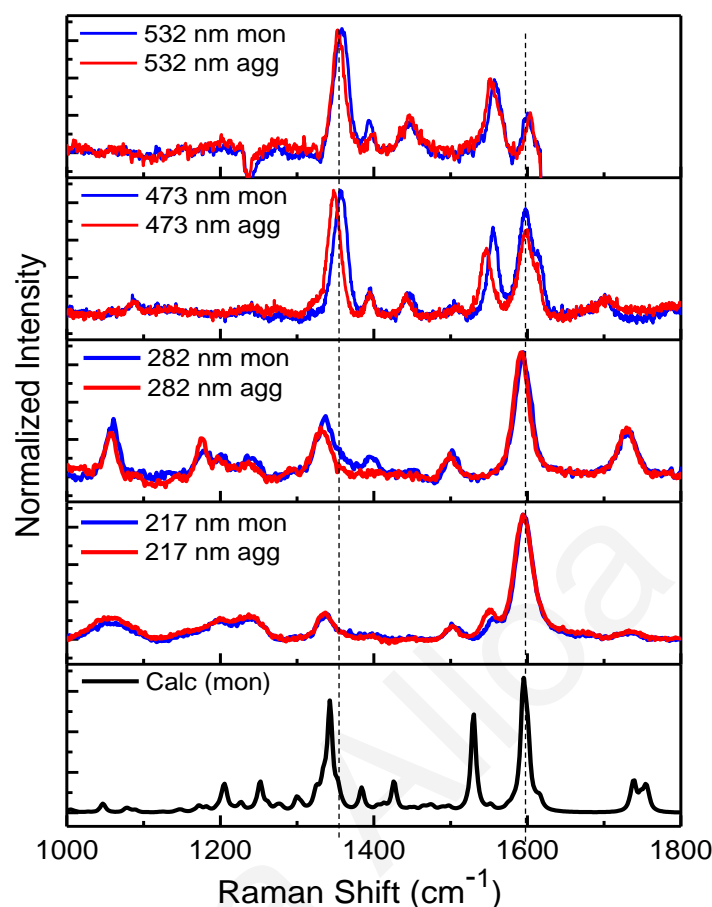
Figure 4-7 Wavelength-dependent RR spectra of MEG-PBI in water showing the monomer-like (at room temperature) and the J-aggregate (at 313 K). Bottom: Calculated Raman spectrum of MEG-PBI in vacuum. Dashed lines highlight major band shifts between visible and UV spectra.

Excitation in the UV is used here to enhance the scattering from the imide groups, where the hydrogen bond between PBI units is suggested to develop, in order to directly probe any interactions upon aggregation due to the sensitivity of amide vibrations to hydrogen bonding. Different N-H vibrations can be examined that provide a signature in the Raman spectrum, as has been shown extensively in the literature on proteins and DNA.[14,17–20] In particular, resonance Raman studies on nucleotides resembling the PBI imide group (uracil, thymine) at different excitations in the UV shows the sensitivity of N-H vibrations to their local environment [14] Besides amides, UV excitation is highly resonant with aromatic rings,[21] therefore the involvement of the aromatic side chains can be resolved. Excitation of aqueous MEG-PBI at 217 nm (**Figure 4-7**) reveals an intense band
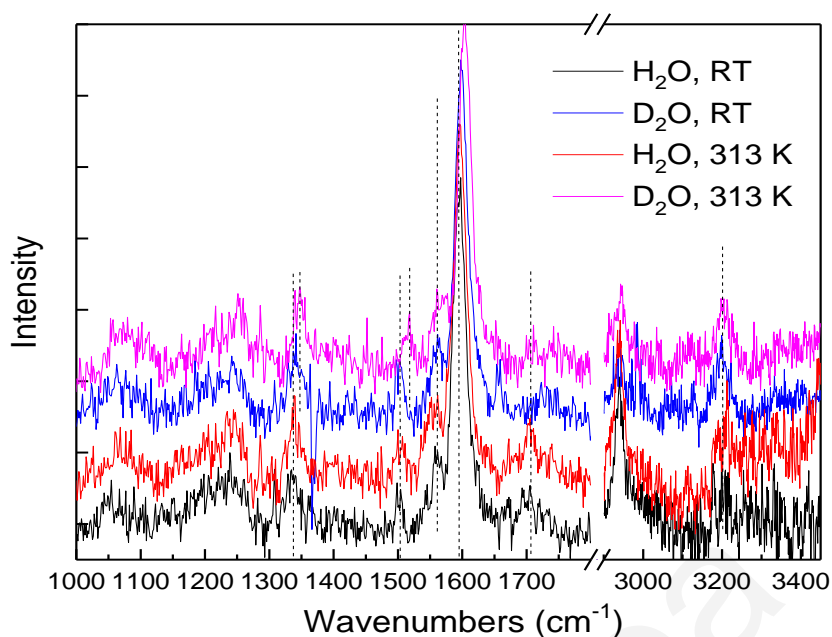
Figure 4-8 RR spectra of MEG-PBI at 217 nm in water and deuterated water showing the monomer at room temperature and the aggregate at 313 K. Dotted lines indicate sample bands.

that corresponds to the C=C phenyl vibrations from the side-chains and smaller bands that correspond to either ring vibrations from the core or the side chains (see **Table 4-2**). A noticeable difference with aggregation is observed in the ~1555 cm^{-1} band that corresponds to a C=C stretch along N-N axis due to the interaction among the PBI units, as it has been established for the visible excitations. It is possible that the bisimide moiety absorbs at this wavelength, therefore the experiment was repeated in deuterated water (**Figure 4-8**) in order to see changes associated with N-D substitution, the crucial connecting point among units in the aggregation process. However, no drastic changes are observed in the spectra that could be associated with the N-D bending vibrations. This suggests that excitation at 217 nm is associated entirely with absorption of the aromatic rings in the molecule. Thus, the invariability of the RR spectra at this wavelength suggests that the aromatic side chains are not involved in the supramolecular assembly.

At 282 nm excitation, the most significant change observed in the RR spectra involves the ~1395 cm^{-1} band that disappears upon self-assembly. This corresponds, according to the calculations, to N-H bending of the imide. Disappearance of this band is consistent with highly restricted movement due to the self-assembly. Assignment of
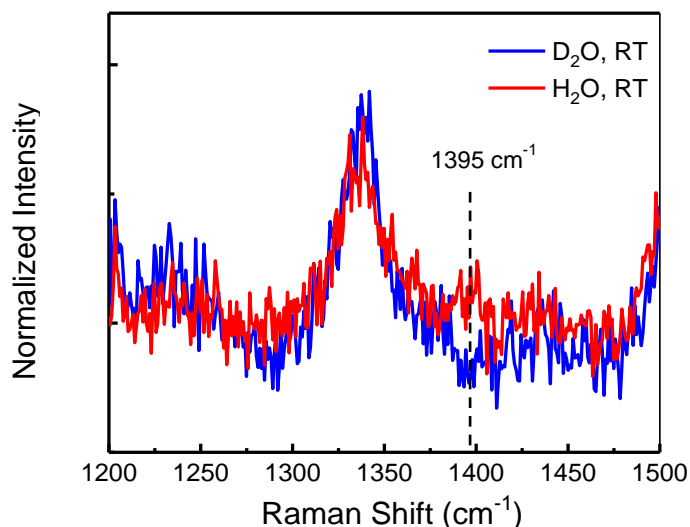
Figure 4-9 RR spectra of MEG-PBI in water and deuterated water with excitation at 266 nm at room temperature. The dash line indicates the position of the N-H bend band.

this band to N-H bending was confirmed by repeating the experiment in deuterated water.

Figure 4-9 shows that the peak disappears upon deuteration, as the N-D bending band is downshifted with respect to the N-H bend. Isotopic substitution has been a valuable tool for band assignment, where for example in proteins N-D substitution clearly shifts the amide II band that involves out-of-phase N-H bending from ≈1555 to ≈1450 cm^{-1}.[22] In addition, a shift is observed for the 1331 cm^{-1} peak with temperature, which could be ascribed to the main ring elongation that we see in the visible (see in the *Appendix*, **Table 10-1**). TD-DFT calculations of the excitation spectrum of MEG-PBI confirm the involvement of the imide moiety in this UV transition (see in the *Appendix*, **Figure 10-1**).

4.2.3 Visible RR in toluene

The PBI aggregated structure in water was compared to the case in an organic solvent, specifically toluene, to get further information about the formation of the supramolecular structure. This experiment helped to understand specific vibrational signatures in the water samples. In organic solvents, PBIs aggregate at lower temperatures (283 K) and dissociate upon increasing temperature (333 K) where the molecule reaches a full monomeric state. The absorption spectra of the molecule in toluene as a function of temperature **(Figure 4-10)** are significantly different to the

ones in water **(Figure 4-2)** both in shape and peak position in the two phases. The intensity ratio of the 0-0 and 0-1 vibronic bands increases noticeably at low temperature as expected for J-aggregates, while both spectra are slightly shifted to higher energies in toluene compared to water. Resonance Raman spectra were obtained with excitation at 473 nm in resonance with the PBI core. The spectra in
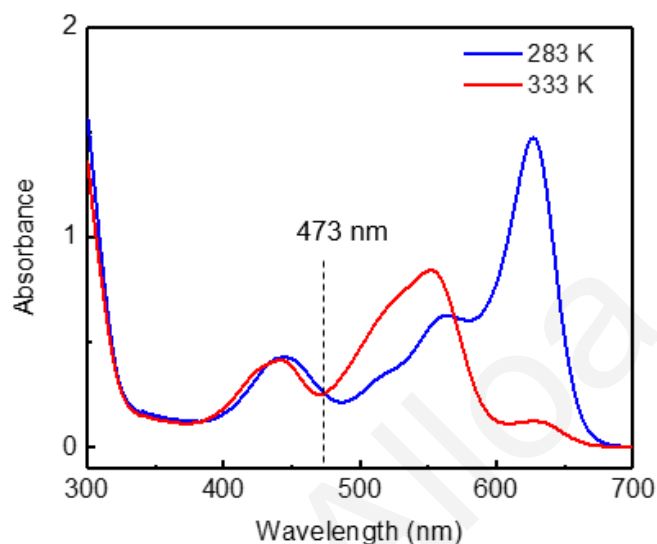
Figure 4-10 Absorption spectra of MEG-PBI toluene solution at 283 K (aggregate) and 333 K (monomer). The excitation wavelength chosen is in a isosbestic point.with the PBI core. The dash line indicate the excitation wavelength employed.

Figure 4-11 show similar relative intensities and shifts in water and in toluene for each phase (monomer-like and aggregate). In particular, the conformations in both solvents share the same peak shift direction; however, the shift is smaller in toluene (4 cm^{-1}), which suggests a weaker hydrogen bond between the units. Moreover, a more intense band is observed at 1704 cm^{-1} in the monomer state, corresponding to the free imide carbonyl, and a weak band at ~1670 cm^{-1} associated with the hydrogen-bonded carbonyl in the aggregate. While a distortion of the perylene core emerges from the band shifts in the aggregate as suggested above for water, increased intensity of the free imide C=O band in toluene reveals a molecule with reduced structural stiffening. In water instead a supramolecular structure is preserved even in the monomer form, where the units are distant in space from each other, resembling single units but still ordered in a macrostructure and hydrogen-bonded to surrounding water molecules, which can be identified, according to previous work,[23] as a less ordered H-aggregate
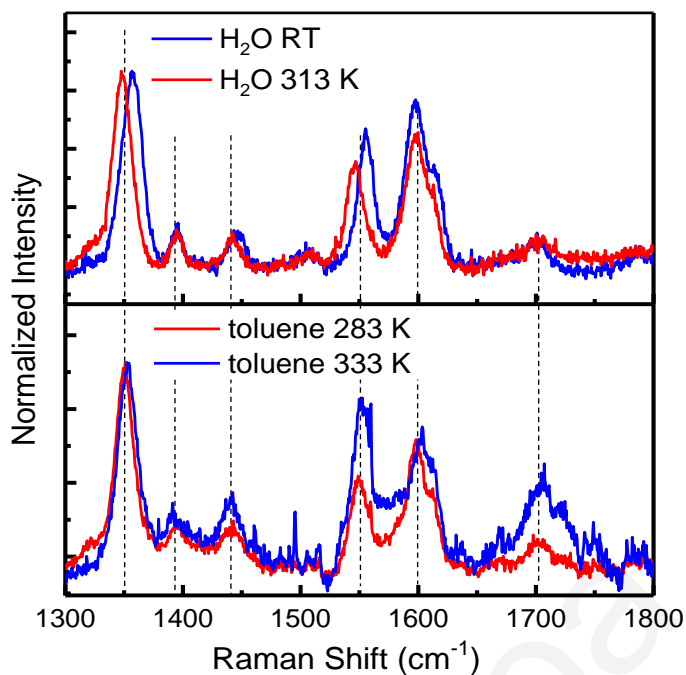
Figure 4-11 RR spectra of MEG-PBI in water versus toluene with excitation at 473 nm. The selected temperatures allow for the corresponding monomer and aggregate species in each solvent: (red) aggregate, (blue) monomers. Dash lines indicate the main aggregate bands in water and toluene.
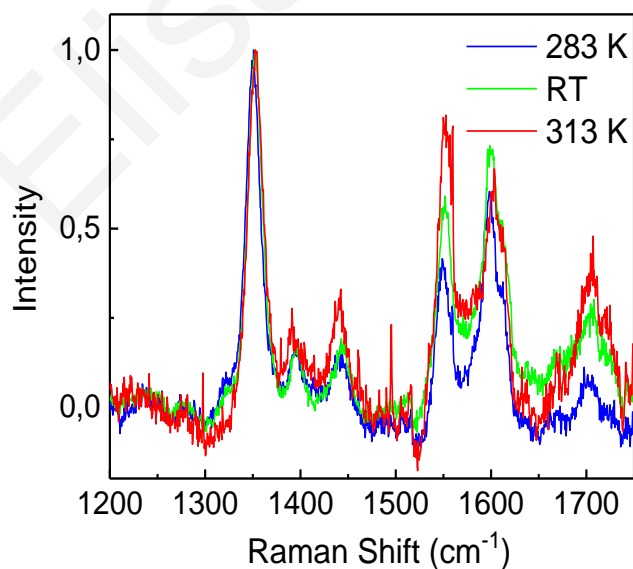
Figure 4-12 Temperature-dependent RR spectra of MEG-PBI in toluene with excitation at 473 nm.

structure. A change in relative intensity is clear for the carbonyl peak (1704 cm^{-1}) and for the ~1555 cm^{-1} band (ring vibration along the main perylene axis): more specifically, both these monomer bands show in toluene a strong increase with increasing temperature.

A progressive reduction of stiffness from aggregate to a fully monomeric state can be identified and this evolution appears clearly in **Figure 4-12** in the changing intensity of these peaks with increasing temperature. The increased relative intensity of the ~1555 cm^{-1} band in the monomer, however, is reminiscent of the relative intensities observed in the water samples with excitation at 532 nm and can thus be associated with resonance with a similar transition, considering that the MEG-PBI absorption bands are blue shifted in toluene.

4.2.4 FT-IR in water and toluene

Driven by the intention of getting more insights in the carbonyl area, and specifically on the imidic C=O bond, complementary FT-IR was employed in order to provide further information on the aggregation process of MEG-PBI in water and toluene. Temperature dependent FT-IR measurements were previously performed on the solid material,[2] where three bands appeared in the C=O stretching region in the case of the aggregate: 1678, 1700, and 1735 cm^{-1}, corresponding to H-bonded imide carbonyls, free imide carbonyls and ester carbonyls in the side chains, respectively, in agreement with the FTIR spectra described above (see **Figure 4-13**). In the monomer state, the 1678 cm^{-1} band disappears, as no H bonding is found. FT-IR experiments in solutions of MEG-PBI in water and toluene were performed at RT, at which water hosts the monomer-like and toluene the aggregate component (**Figure 4-13**). Good agreement is observed for the overall IR spectra in the two solvents, as well as with the calculated IR spectrum, with the exception of the position of the carbonyl bands that are sensitive to the solvent environment (the calculation was performed in vacuum); therefore, the bands that appear in water correspond to real PBI bands, even if the MEG-PBI concentration is quite low and the solvent could interfere with the analysis generating artifacts. As expected, some of the bands appear with similar frequency as in the Raman spectra but with different intensity. The 1734 cm^{-1} peak appears in both

solvents, due to the carbonyl group in the side chain esters. Two peaks at 1670 and 1701 cm^{-1} are observed in toluene, confirming the previous FT-IR on the solid.

Differently, for the monomer-like state in water only a small shoulder to the main ester band is observed in the position expected for the free carbonyl. However, the water bending band at 1650 cm^{-1} is quite large and may possibly interfere with this band upon subtraction. **Table 4-2** summarizes all the assignments of the Raman and IR bands according to the DFT calculations.
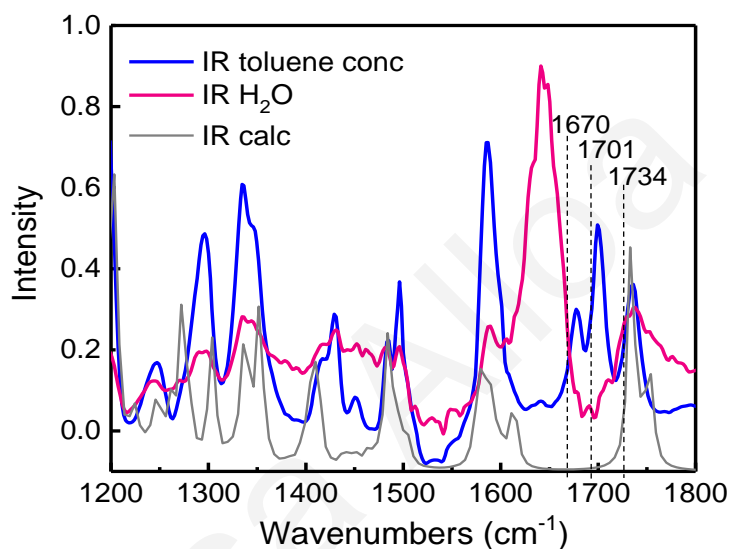
Figure 4-13 FT-IR spectra of toluene and water solution of MEG-PBI run at room temperature, compared with IR calculation (in vacuum, scale factor *0.97). The strong band ~1650 cm^{-1} in the IR spectrum of MEG-PBI in water corresponds to the bending mode of water.

Table 4-2 Assignments of Raman bands observed at 217, 282, 473 and 532 nm.

Band Assignments	Raman Calc (cm^{-1})	Calc *0.97 (cm-1)	RR 217 nm	RR 282 nm	RR 473 nm	RR 532 nm
δ_{C-H}, Breath mode phenyl ring PER	1078	1045	1057 w	1057 m		
δ_{C-H} SC	1217	1180	1178 w	1178 m		
δ_{C-H} SC δ_{N-H} PER	1241	1203	1202 w	1202 w		1202 w
$\nu_{C=C}$, δ_{C-H}, ν_{C-O} SC $\nu_{C=C}$, δ_{C-H} PER	1290	1251	1240	1240		
$N_{C=C}$ ∥ N-N axis, δ_{C-H} PER	1374	1333	1333 w	1333 m		
$\nu_{C=C}$ ∥ N-N axis PER	1383	1341			1359 s	1359 s
$\nu_{C=C}$, δ_{C-H} ⊥ N-N axis PER $\nu_{C=C}$, δ_{C-H} SC	1425	1382			1395 m	1395 m
δ_{N-H} PER	1421	1378		1395 w		
sym $\nu_{C=C}$ PER	1467	1422		1447 vw	1447 m	1447 m
δ_{C-H} phenyl rings SC	1529	1483	1500 w	1500 m		
$\nu_{C=C}$ ∥ N-N axis PER $\nu_{C=C}$, δ_{C-H} SC	1575	1527	1553 w		1557 s	1557 s
$\nu_{C=C}$, δ_{C-H} ⊥ N-N axis PER	1643	1593	1595 s	1595 s	1598 s	1598 m
$\nu_{C=O}$ imide PER $\nu_{C=O}$ esters SC	1791 1806	1737 1751	1729 w (esters)	1729 m (esters)	1706 w (free imide)	

Legend: ν: stretching, δ: bending, SC: side chains, PER: perylene ring, ∥: parallel, ⊥: perpendicular, s: symmetric, s: small, m: medium, i: intense.

4.3 Conclusions

In this work we have used vibrational spectroscopy to analyze the MEG-PBI structure upon transition from the monomer-like to the supramolecular J-aggregate state. RR excitation energy variation facilitated selective probing of different chromophores in order to elucidate their participation in the aggregation process. FT-IR provided complementary insights to RR and could better discriminate the C=O signal involved in the hydrogen bonding among the PBI units. Temperature dependent RR spectroscopy revealed that upon aggregation the perylene core assumes a distorted conformation with elongation parallel to the N-N axis induced by hydrogen bonding of the imide protons with carbonyls from neighboring molecules resulting in a head-to-tail arrangement. A concentration-dependent analysis on MEG-PBI provided evidence that the sample concentration does not affect the aggregation pattern in the range studied. Moreover, a full agreement was found between the Raman spectrum displayed by the MEG-PBI aggregate in solution and that in thin film, suggesting that processing of the material from solution to solid does not affect its conformation. Deuteration of MEG-PBI helped identify the N-H bending vibration, which appeared only in the case of the monomer-like state, as in the J-aggregate the constriction of the supramolecular structure causes a reduced intensity. As previously known, the aggregation pattern of MEG-PBI in water is influenced by the hydrophobic effect, as aggregation is an entropically-driven process. Our study revealed that in water a stiffer macrostructure is induced even in the monomer-like state, while monomers in toluene appear less tightly bound in the supramolecular structure. This study provided key insights in the structure of this supramolecular system that can improve the understanding of the photophysical properties of this and other similar systems.

References

1.   Lova, P. *et al.* All-polymer photonic microcavities doped with perylene bisimide J-aggregates. *Adv. Opt. Mater.* **5**, 1700523 (2017).

2.   Grande, V., Soberats, B., Herbst, S., Stepanenko, V. & Würthner, F. Hydrogen-bonded perylene bisimide J-aggregate aqua material. *Chem. Sci.* **9**, 6904–6911 (2018).

3.   Wang, Q. *et al.* High-water-content mouldable hydrogels by mixing clay and a dendritic molecular binder. *Nature* **463**, 339–343 (2010).

4.   Cohen, E. *et al.* Robust aqua material: a pressure-resistant self-assembled membrane for water purification. *Angew. Chemie - Int. Ed.* **56**, 2203–2207 (2017).

5.   Würthner, F. *et al.* Perylene bisimide dye assemblies as archetype functional supramolecular materials. *Chemical Reviews* **116**, 962–1052 (2016).

6.   Ambrosek, D. *et al.* Photophysical and quantum chemical study on a J-aggregate forming perylene bisimide monomer. *Phys. Chem. Chem. Phys.* **13**, 17649 (2011).

7.   Lin, H. *et al.* Collective fluorescence blinking in linear J-aggregates assisted by long-distance exciton migration. *Nano Lett.* **10**, 620–626 (2010).

8.   Spano, F. C. & Silva, C. H- and J-aggregate behavior in polymeric semiconductors. *Annu. Rev. Phys. Chem.* **65**, 477–500 (2014).

9.   Kaiser, T. E., Wang, H., Stepanenko, V. & Würthner, F. Supramolecular construction of fluorescent J-aggregates based on hydrogen-bonded perylene dyes. *Angew. Chemie* **119**, 5637–5640 (2007).

10. Ghosh, S., Li, X. Q., Stepanenko, V. & Würthner, F. Control of H- and J-type pi stacking by peripheral alkyl chains and self-sorting phenomena in perylene bisimide homo- and heteroaggregates. *Chemistry (Easton).* **14**, 11343–11357 (2008).

11. Sobolewski, A. L. & Domcke, W. Molecular mechanisms of the photostability of life. *Phys. Chem. Chem. Phys.* **12**, 4897 (2010).

12. Toyama, A., Takeuchi, H. & Harada, I. Ultraviolet resonance Raman spectra of adenine, uracil and thymine derivatives in several solvents. Correlation between band frequencies and hydrogen-bonding states of the nucleic acid bases. *J. Mol. Struct.* **242**,

87–98 (1991).

13. Connelly, G. P., Bai, Y., Jeng, M. - F & Englander, S. W. Isotope effects in peptide group hydrogen exchange. in *Proteins: Structure, Function, and Bioinformatics* **17**, 87–92 (1993).

14. Fodor, S. P. A., Rava, R. P., Hays, T. R. & Spiro, T. G. Ultraviolet resonance Raman spectroscopy of the nucleotides with 266-, 240-, 218-, and 200-nm pulsed laser excitation. *J. Am. Chem. Soc.* **107**, 1520–1529 (1985).

15. Akins, D. L. Enhanced Raman scattering by molecular nanoaggregates. *Nanomater. Nanotechnol.* **4**, 1 (2014).

16. Coles, D. M. *et al.* A characterization of the Raman modes in a J-aggregate-forming dye: a comparison between theory and experiment. *J Phys Chem A* **114**, 11920–11927 (2010).

17. Chi, Z., Chen, X. G., Holtz, J. S. W. & Asher, S. A. UV resonance raman-selective amide vibrational enhancement: Quantitative methodology for determining protein secondary structure. *Biochemistry* **37**, 2854–2864 (1998).

18. Asher, S. A. *et al.* Dihedral ψ angle dependence of the amide III vibration: A uniquely sensitive UV resonance Raman secondary structural probe. *J. Am. Chem. Soc.* **123**, 11775–11781 (2001).

19. Rygula, A. *et al.* Raman spectroscopy of proteins: A review. *J. Raman Spectrosc.* **44**, 1061–1076 (2013).

20. Kasiouli, S. *et al.* Resonance Raman investigation of β-cyclodextrin-encapsulated π-conjugated polymers. *J. Phys. Chem. B* **117**, 5737–5747 (2013).

21. Balakrishnan, G. & Spiro, T. G. Ultraviolet resonance Raman (UVRR) spectroscopy studies of structure and dynamics of Proteins. *Encycl. Biophys.* **32**, 2697–2707 (2013).

22. Pieridou, G., Avgousti-Menelaou, C., Tamamis, P., Archontis, G. & Hayes, S. C. UV resonance Raman study of TTR(105-115) structural evolution as a function of temperature. *J. Phys. Chem. B* **115**, 4088–4098 (2011).

23. Sarbu, A., Biniek, L., Guenet, J.-M., Mésini, P. J. & Brinkmann, M. Reversible J- to H-aggregate transformation in thin films of a perylenebisimide organogelator. *J. Mater. Chem.* **3**, 1235–1242 (2015).

CHAPTER 5

Preliminary RR study of a hydrophobic PBI

5.1 Introduction

PBIs in their well-known "traditional" organic-soluble form have been well recognized as versatile chromophores with strong absorption, near unity fluorescence quantum yield, and high thermal and photochemical stability.[1] Their high chemical flexibility allows various substitutions thereby tuning reactivity and spectral properties.[2] Due to these appealing assets, perylene bisimides and their related derivatives have continuously received significant
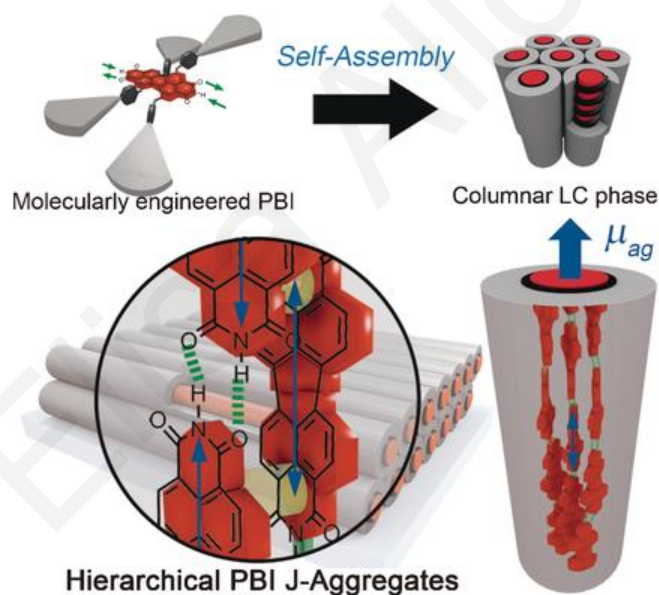
Figure 5-1 Schematic illustration of the molecular self-assembly of MEH-PBI into columnar hexagonal liquid crystals. Blue arrows indicate the direction of the main transition dipole moments (μ_{ag}) of the PBI molecules.[3]

attention for their potential applications in biomedicine (bioimaging)[4] and molecular optoelectronic devices, such as organic photovoltaics (e.g. as acceptors),[5,6] field-effect transistors,[7] light-emitting diodes,[8] light-harvesting arrays[9] and LCD color filters.[10] More challenging still remains their applications as a thermotropic liquid-crystalline phase, which is also the main purpose of the PBI J-aggregate, whose preliminary spectroscopic analysis is presented in this *Chapter*. Herein, the MEH-PBI dye bears organic residues (branched 2-

ethylhexyl groups) at *meta*-positions of a tetraphenoxy-functionalized perylene bisimide. More specifically, hydrogen-bond donors/acceptors and π–π interactions were employed for the design of this functional chromophore: these forces collaborate in a self-complementary way to build a supramolecular connection among the monomers in order to achieve one-dimensional brickwork-type J-aggregates, which in turn organize into liquid crystals. This molecular design typically leads to the spontaneous elongation of stacked units of the cores via π–π interactions forming columnar assemblies with the formation of a triple-stranded J-aggregate helix with an orthogonal orientation of the PBIs, as depicted in **Figure 5-1**. The formation of intermolecular hydrogen bonds appears along the columnar axis. The structural analysis and modeling of the PBI assemblies was carried out by wide and middle angle X-ray scattering (WAXS and MAXS), where the diffraction patterns could properly determine the fiber orientation and the relative position of the fibers.[3,11–13]
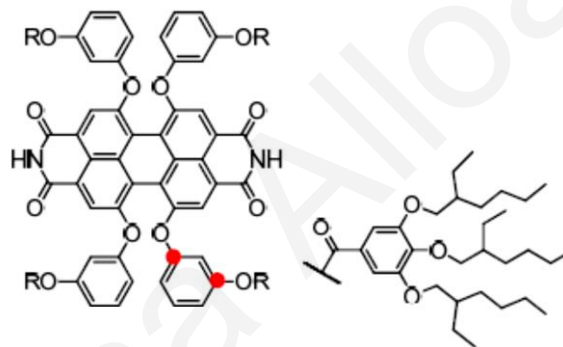
Figure 5-2 Hydrophobic perylene bisimide (MEH-PBI).[3]

The present Chapter complements the Resonance Raman study presented in the previous chapter, comparing the structure of the water-soluble MEG-PBI in the J-aggregate with its hydrophobic analogue (see **Figure 5-2**).

5.2 Results and discussion

5.2.1 Absorption Spectroscopy

The solvent dependent behavior of MEH-PBI was initially studied because of the necessity to have a clear spectral view of the Raman bands that characterize this system, without any overlap from solvent peaks. Moreover, this study gave the opportunity to get clues about the solubility of the MEH derivative in different environments and about its capability to spectroscopically show different aggregate conformations as a function of temperature. UV-vis absorption measurements can help distinguish easily the various phases of the molecule. In particular, the J-aggregate formation, evident from a sharp red-shifted peak at 624 nm,

occurs at lower temperatures with the exact value varying depending on the solvent used. Different organic solvents were used, specifically cyclohexane, carbon tetrachloride and benzene, because of their different melting points, hydrophobicity, polarity, and consequent capability to provide a different transition temperature between the two perylene bisimide conformations. This is an essential aspect if we consider the importance of the PBI side chains in solubilizing the structure by solvent interactions, in order to "tune" with a specific PBI form.
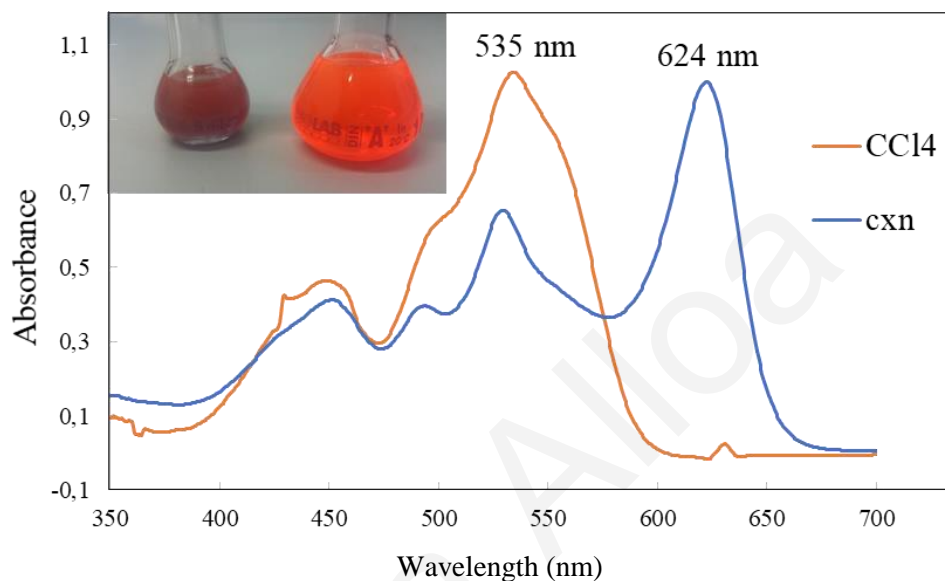
Figure 5-3 Absorption spectrum at room temperature of MEH-PBI in carbon tetrachloride (CCl$_4$) and cyclohexane (cxn). Inset: color change displayed by the two solutions (orange: CCl$_4$, brown: cxn).

At room temperature, solutions of MEH-PBI in carbon tetrachloride and cyclohexane exhibit a different color as shown in the inset in **Figure 5-3**, suggesting that we are dealing with different molecular conformations in each case. The UV-vis absorption spectra show in the case of carbon tetrachloride a band at 535 nm indicating the presence of monomers, and a band at 624 nm in the case of cyclohexane representing the J-aggregate signature. Notably in the case of cyclohexane, a second band (more structured than the carbon tetrachloride one) appears at 535 nm indicating the presence of monomers also in solution at this temperature, while carbon tetrachloride displays a very small peak assigned to aggregated species. Therefore, as a guideline, the intense orange color of the CCl$_4$ solution indicates the

presence of the monomer form, while the brown solution reveals a prevalent aggregate state (in its pure aggregate form the solution would appear blue).

Optical findings were examined to guide the choice of the temperature range for the resonance Raman (RR) experiments in the visible, with the goal to study the solvent-dependent conformation of the MEH-substituted derivative alone and in the supramolecular structure. Cyclohexane was first chosen because it was the solvent in which the Würthner's group (that provided us with the material) previously observed the temperature-driven interconversion at low concentration between the monomer state (343 K, red color) and almost complete aggregation (281 K, bluish color), as shown in **Figure 5-4**.[3] Moreover, cyclohexane is an advantageous solvent for Raman, as it is well characterized and it can be used as an internal standard, both for frequency calibration purposes and absolute intensity measurements. However, the presence of several bands can become a disadvantage when solvent and sample peaks overlap.
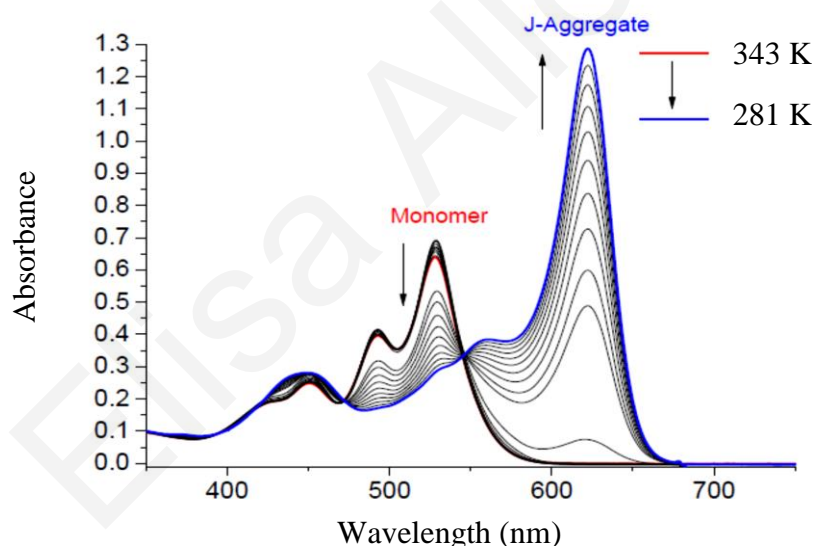
Figure 5-4 Absorption spectra in cyclohexane as a function of temperature.[3]

The profile of the absorption spectra of the hydrophobic PBI in carbon tetrachloride (CCl_4) and cyclohexane (**Figure 5-3**) resembles that of MEG-PBI in toluene, with a few differences concerning the monomer peak position and band profile: this MEH-PBI band is more vibronically structured and it is approximately 15 nm blue-shifted compared to the MEG-substituted derivative, probably because of the limited interaction with the solvent. A broader spectral profile (meaning more disorder of the system) is seen in the case of MEH-PBI itself in carbon tetrachloride.

5.2.2 Visible RR Spectroscopy

Based on the temperatures that the monomer and aggregate form of the MEH-PBI in cyclohexane predominantly appear in the absorption spectra, temperature-dependent RR measurements with excitation at 473 nm were performed at 277 K (aggregated state) and 313 K (monomer state) (**Figure 5-5**). Two MEH-PBI bands are observed in cyclohexane at
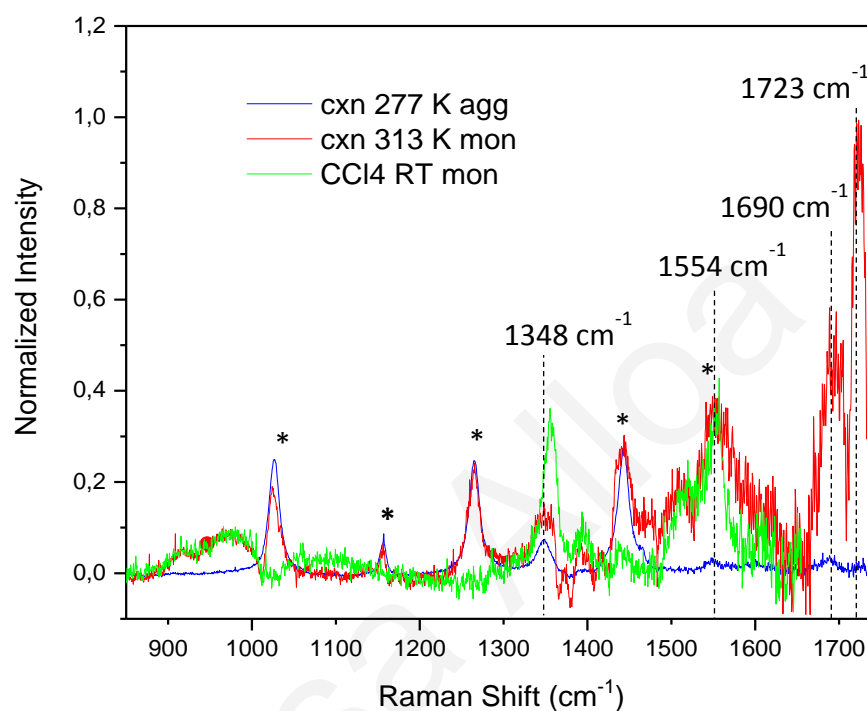
Figure 5-5 Temperature-dependent Resonance Raman spectra of MEH-PBI in cyclohexane and carbon tetrachloride with excitation at 473 nm showing the monomer (red in cyclohexane and green in carbon tetrachloride) and J-aggregate (blue) conformations. *: solvent peaks. Dashed lines indicate the position of the most important sample modes.

1348 and 1554 cm^{-1} that, according to our previous assignments, correspond to C=C stretching along the long (N-N) axis of the perylene. Moreover, two other peaks appear in the 1700 cm^{-1} region (where carbonyl bands are expected), specifically at 1690 and 1723 cm^{-1}, that correspond to free imide carbonyls and side chain esters**.**

Some weaker bands are also noticeable in this spectral range (e.g. 1395 and 1605 cm^{-1}, corresponding to C=C stretching perpendicular to the N-N axis and 1445 cm^{-1} corresponding to C=C stretching that involves the central aromatic ring, where the perylene is twisted). Increasing the temperature of the cyclohexane solution to reach the monomer conformation induces strong fluorescence that produces artifacts in the spectrum (such as negative band

features that affect the profile of crucial bands, as well as artificially strong intensities in the carbonyl band region upon background subtraction) making the comparison to the aggregate spectrum difficult. This can be explained considering the excitation wavelength at 473 nm, where the monomer displays higher absorption, while the aggregate spectra red-shifts with lower fluorescence compared to the monomer. In addition, the presence of many cyclohexane peaks in the RR spectra is problematic for this study, as they overlapped with main sample peaks, making the analysis of results difficult.

Driven by the necessity to better elucidate the presence of the PBI bands without solvent interference, the solvent was evaporated and the PBI powder re-dissolved in carbon tetrachloride and benzene. The color of the solution at room temperature was in these cases orange rather than brown, as these non-polar solvents dissolved the perylene monomer much better. Cooling down the solution in carbon tetrachloride and benzene to 250 and 280 K, the respective solvent melting points, the solution turned again a bluish color (the aggregate form), in a very different range of temperatures compared to cyclohexane. As displayed in **Figure 5-5**, carbon tetrachloride at room temperature sustains the monomer conformation as the C-C stretching band appears at 1354 cm^{-1}, about 6 cm^{-1} upshifted with respect to the aggregate.

Comparing in **Figure 5-6** the RR spectrum of the aggregate conformation in cyclohexane (at 277 K) and the monomer one now in benzene (at room temperature), a shift of 6 cm^{-1} is clearly detected from 1348 to 1354 and from 1548 to 1554 cm^{-1} as in the case of CCl$_4$. Fluorescence complicates the background subtraction in the carbonyl area making the extraction of useful information difficult.

A direct comparison between MEG-PBI and MEH-PBI aggregates in organic solvents, respectively toluene and cyclohexane, is provided in **Figure 5-7**. The main bands appear to match each other quite well due to the same core structure of the two derivatives and both analogues exhibit the same shift pattern for both 1354 and 1554 cm^{-1} peaks, suggesting a distortion of the perylene core with aggregation (notice that the 1447 cm^{-1} is covered by a solvent peak in the MEH-PBI). A difference can be identified for the 1354 cm^{-1} band: in the case of MEH-PBI it shifts to lower frequencies, which means that the aggregate is more strongly bound. The smaller shift for MEG-PBI in toluene (4 cm^{-1} vs. 6 cm^{-1}) suggests a weaker hydrogen bond between the units, possibly due to the difference in side-chain structure and differing interaction with the organic solvent: the bulkiness of the side chains

in the bay area drives the molecule to form self-assemblies with a more slipped J aggregate tendency (thanks to the large degree of twisting of the core), while the π-π stacking, driving to a H aggregate, decreases.[15] A similar explanation may be provided for the differences in frequencies between the two aggregates in the carbonyl region. As mentioned above, this region looks quite uncertain for the MEH derivative as the carbonyl peaks are found in a
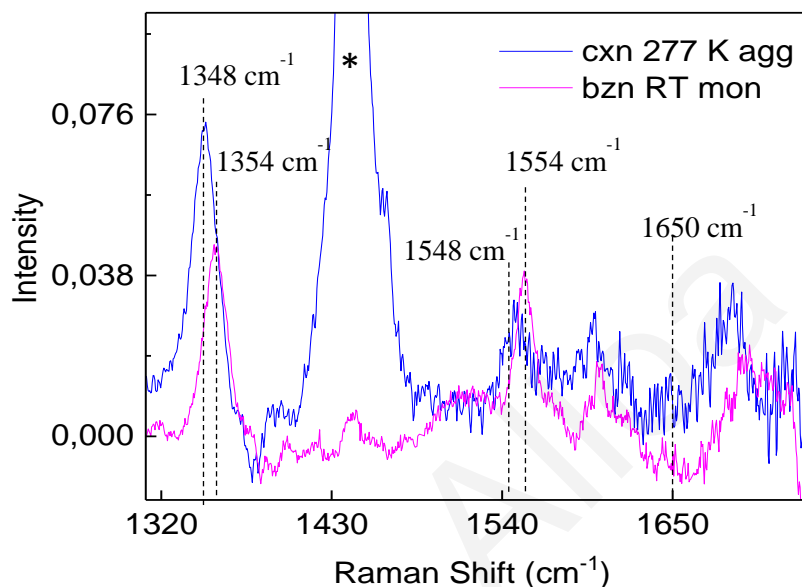
Figure 5-6 Temperature-dependent Resonance Raman spectra of MEH-PBI in cyclohexane (aggregate) and benzene (monomer) with excitation at 473 nm. *: solvent peaks.

spectral range of high fluorescence, so that intensity artifacts may arise. In MEG-PBI the carbonyl bands appear at 1670, 1704 and 1734 cm^{-1} corresponding to H-bonded imide carbonyls, free imide carbonyls and side chain esters, respectively. Two clear peaks appear for the MEH analogue approximately at 1690 and 1723 cm^{-1}, due to the free imide and C=O esters, and a third peak (due to the hydrogen bonded C=Os) may be identified at ~1650 cm^{-1} (however with some speculation due to noise from fluorescence background subtraction). The fact that the carbonyl band that is associated to the aggregate self-assembly is 20 cm^{-1} downshifted in the MEH derivative (compared to the MEG analogue), suggests that the aggregate is more strongly bound, as attested by the stronger downshift of the C-C stretches in the N-N axis direction. The free imide carbonyls and the side chain esters also exhibit a downshift of approximately 10 cm^{-1}. This is unexpected as the solvent is non-polar and aprotic and not prone to hydrogen bonding and further investigation is necessary. If we compare MEH-PBI in cyclohexane with the MEG-PBI in organic solvent (i.e., toluene), in both situations carbonyl monomer bands display a strong increase with increasing

temperature. While we had attributed this increase to a progressive reduction of stiffness from aggregate to a fully monomeric conformation in the case of MEG-PBI, it is highly possible that this similar behavior in MEH-PBI can be attributed to the increase in fluorescence intensity as the monomer state becomes more prevalent.
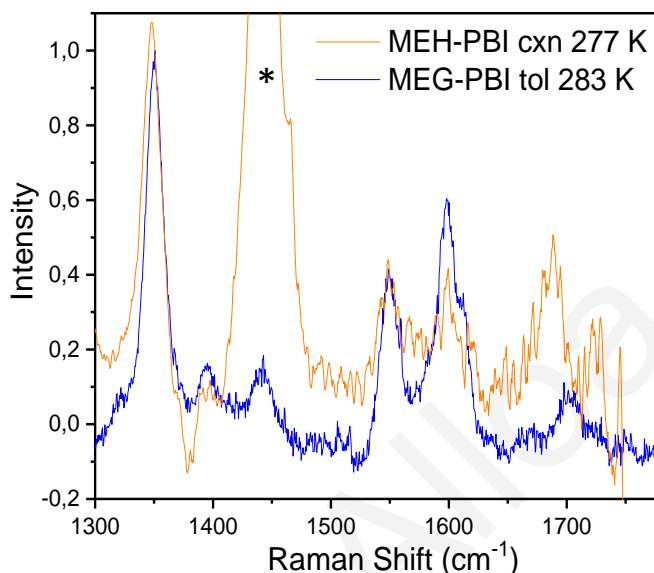
Figure 5-7 Resonance Raman spectra on MEG-PBI and MEH-PBI in organic solvents with excitation at 473 nm. At the chosen temperature excitation at 473 nm is in resonance with the aggregated form of both PBIs. *: solvent peaks.

Perylene bisimide side chains can influence aggregation as previously observed.[16] The length of bulky side chains can affect the intermolecular interactions and under appropriate conditions it can result in phase segregation in the solid state (thin films). The different frequencies observed for the non-hydrogen bonded carbonyls of MEH-PBI reflect a modified carbonyl environment because of the different hydrophobicity and space occupied by the side chains in the aggregate structure. This effect that can be imagined through the model in **Figure 5-8** considering that the MEG structure has repeating polar ethers, while MEH has more hydrophobic alkyl chains, that can be better solvated by the organic non-polar solvent. It is possible that this better solvation can pull these hydrophobic chains away from the PBI core allowing more space for the supramolecular structure to elongate through H-bonding interactions between the units forming J aggregates. This implies two slightly different supramolecular structures (strongly and weaker hydrogen-bonded units), because of the specific molecular solubility exhibited in organic solvents with different polarity. This

is clearly evident from the π-π* absorption band of the MEH-PBI monomer in cyclohexane as the band is 15 nm blue shifted and is more structured than the case of MEG-PBI in toluene.
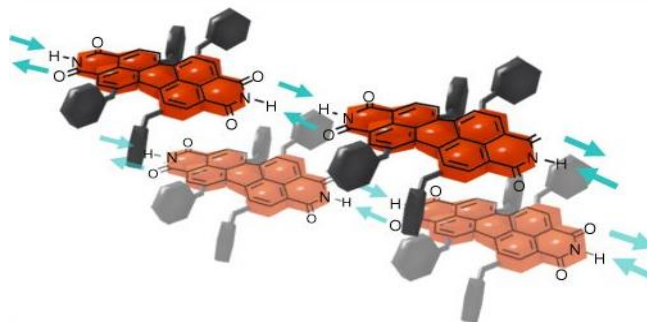
Figure 5-8 Molecular model showing the relevance of the side chains topology, dimension and position on the self-assembling of the PBIs.[17]

5.1 Conclusions

The MEH-PBI molecule here investigated shows a transition between a monomer to a hydrogen-bonded aggregate as a function of temperature, similarly to the case of MEG-PBI. The transition temperature varies depending on the solvent chosen due to the different solubility in each one. The detailed experiments performed on MEG-PBI and presented in *Chapter 4* gave the opportunity to better understand the preliminary data obtained on the hydrophobic analogue. A few differences are observed in the case of MEH-PBI, such as the position and spectral profile of the monomer absorption band, suggesting that the side chains and their interaction with solvent may influence the consequent supramolecular structure of this PBI. Apart from this minor variation, the structure of these two PBI monomers is very similar as the main observed bands in the RR spectra correspond to each other.[18–21] The main frequency shifts from monomer-like to the supramolecular J-aggregate phase seen for the MEG-PBI bands are evident (when not covered by solvent peaks) also in the case of MEH-PBI and this can lead to a similar interpretation: the perylene core undergoes a distortion upon aggregation, where the bonds along the perylene long axis lengthen and the ones perpendicular to that shorten. To conclude, a similar aggregation pattern between different PBIs in organic solvents is found. Due to the interaction of these molecules with the organic solvents they are dissolved in and thus to the different environment occupied by each supramolecular structure, the carbonyl area spectra differs significantly between the two molecules: the hydrogen bonded structure looks more strongly connected in MEH-PBI due to its more hydrophobic side chains, which favor a J aggregation process instead of π-π stacking.

References

1. Weil, T., Vosch, T., Hofkens, J., Peneva, K. & Müllen, K. The rylene colorant family-tailored nanoemitters for photonics research and applications. *Angew. Chemie - Int. Ed.* **49,** 9068–9093 (2010).

2. Würthner, F. Perylene bisimide dyes as versatile building blocks for functional supramolecular architectures. *Chem. Commun.* **4,** 1564–1579 (2004).

3. Herbst, S., Soberats, B., Leowanawat, P., Lehmann, M. & Würthner, F. A columnar liquid-crystal phase formed by hydrogen-bonded perylene bisimide J-aggregates. *Angew. Chemie - Int. Ed.* **56,** 2162–2165 (2017).

4. Sun, M., Müllen, K. & Yin, M. Water-soluble perylenediimides: design concepts and biological applications. *Chem. Soc. Rev.* **45,** 1513–1528 (2016).

5. Zhang, C. *et al.* Thienobenzene-fused perylene bisimide as a non-fullerene acceptor for organic solar cells with a high open-circuit voltage and power conversion efficiency. *Mater. Chem. Front.* **1,** 749–756 (2017).

6. Kaiser, T. E., Wang, H., Stepanenko, V. & Würthner, F. Supramolecular construction of fluorescent J-aggregates based on hydrogen-bonded perylene dyes. *Angew. Chemie* **119,** 5637–5640 (2007).

7. Nowak-Król, A., Shoyama, K., Stolte, M. & Würthner, F. Naphthalene and perylene diimides – better alternatives to fullerenes for organic electronics? *Chem. Commun.* **54,** 13763–13772 (2018).

8. Zhou, J. *et al.* Magic-angle stacking and strong intermolecular π-π interaction in a perylene bisimide crystal: an approach for efficient near-infrared (NIR) emission and high electron mobility. *J. Phys. Chem. Lett.* **9,** 596–600 (2018).

9. Hippius, C., Schlosser, F., Vysotsky, M. O., Böhmer, V. & Würthner, F. Energy transfer in calixarene-based cofacial-positioned perylene bisimide arrays. *J. Am. Chem. Soc.* **128,** 3870–3871 (2006).

10. Struijk, C. W. *et al.* Liquid crystalline perylene diimides: architecture and charge carrier mobilities. *J. Am. Chem. Soc.* **122,** 11057–11066 (2000).

11. Ghosh, S., Li, X. Q., Stepanenko, V. & Würthner, F. Control of H- and J-type pi stacking by peripheral alkyl chains and self-sorting phenomena in perylene bisimide

homo- and heteroaggregates. *Chemistry (Easton).* **14,** 11343–11357 (2008).

12.   Kaiser, T. E., Stepanenko, V. & Würthner, F. Fluorescent J-aggregates of core-substituted perylene bisimides: Studies on structure-property relationship, nucleation-elongation mechanism, and sergeants-and-soldiers principle. *J. Am. Chem. Soc.* **131,** 6719–6732 (2009).

13.   Lova, P. *et al.* All-polymer photonic microcavities doped with perylene bisimide J-aggregates. *Adv. Opt. Mater.* **5,** 1700523 (2017).

14.   Personal communication with Prof. Frank Würthner.

15.   Würthner, F. *et al.* Perylene bisimide dye assemblies as archetype functional supramolecular materials. *Chemical Reviews* **116,** 962–1052 (2016).

16.   Keivanidis, P. E., Howard, I. A. & Friend, R. H. Intermolecular interactions of perylene diimides in photovoltaic blends of fluorene copolymers: Disorder effects on photophysical properties, film morphology and device efficiency. *Adv. Funct. Mater.* **18,** 3189–3202 (2008).

17.   Herbst, S. *et al.* Self-assembly of multi-stranded perylene dye J-aggregates in columnar liquid-crystalline phases. *Nat. Commun.* **9,** (2018).

18.   Angelella, M., Wang, C. & Tauber, M. J. Resonance Raman spectra of a perylene bis(dicarboximide) chromophore in ground and lowest triplet states. *J. Phys. Chem. A* **117,** 9196–9204 (2013).

19.   Brown, K. E., Veldkamp, B. S., Co, D. T. & Wasielewski, M. R. Vibrational dynamics of a perylene-perylenediimide donor-acceptor dyad probed with femtosecond stimulated Raman spectroscopy. *J. Phys. Chem. Lett.* **3,** 2362–2366 (2012).

20.   Wang, H. *et al.* Structure-dependent all-optical switching in graphene-nanoribbon-like molecules: fully conjugated tri(perylene bisimides). *J Phys Chem A* **114,** 9130–9135 (2010).

21.   Gao, F., Zhao, Y. & Liang, W. Vibronic spectra of perylene bisimide oligomers: effects of intermolecular charge-transfer excitation and conformational flexibility. *J Phys Chem B* **115,** 2699–2708 (2011).

CHAPTER 6

OFs model for excited-state dynamics

6.1 Introduction

Monitoring in detail how the ultrafast excited state evolution proceeds with structural probes remains nowadays a challenge. In light of this, we have applied Femtosecond Stimulated Raman Spectroscopy (FSRS)[1–3] as a powerful technique to investigate the ultrafast dynamics and photoinduced conformational changes of a series of oligofluorene compounds, with the goal of understanding the vibrational mode-specific dynamics that are associated with the early relaxation of the electronic excited states.[4] FSRS, apart from providing a complete vibrational spectrum for following early-time (tens of femtoseconds) structural dynamics, adaptable on the timescale that is most valuable for understanding reaction kinetics of photoexcited conjugated molecules.[1,5,6] This technique has been previously employed to directly investigate the ultrafast formation of charge carrie rs in other conjugating polymers, in films as well as in solution.[7,8] While correlations in the excited state absorption among oligofluorenes of different chain lengths have gone unnoticed by Ling et al.,[9] other work, e.g. by Denis et al. or Hintschich et al. reveal changes in the electron density of these oligomers in the excited state, leading to conformational relaxation and exciton migration.[10,11] Previous work by Hayes and Silva on OFs reported the use of ultrafast transient absorption spectroscopy to obtain excited state spectra of two oligofluorene derivatives in dilute solution,[12] which displayed a photoinduced absorption band with clear vibronic structure that changed as a function of chain length. Employing a rigorous computational analysis using a time-dependent formalism of absorption, this study was able to extract the principal excited-state vibrational normal-mode frequencies that couple to the electronic transition, the configurational displacement of the higher-lying excited state, and the reorganization energies. This work has provided some insight on the details of the first two excited states in the energetic manifold of phenylene-based materials ($1B_u$ and mA_g), however, there remained a need for extending the study to longer oligomers. In addition, this and other studies on oligofluorenes using optical spectroscopies lacked the ability to directly probe the structural evolution in the excited state, with their conclusions based on overall

spectral shifts or theoretical calculations. FSRS, however, allows us here to determine the excited-state molecular structure, the totally symmetric modes that couple to the ground and excited-state transitions, and the early-time dynamics of configurational change.

6.2 Results and discussion

Femtosecond stimulated Raman spectroscopy (FSRS) was employed on a series of fluorene oligomers (OFs) in order to directly monitor excited state structural evolution at very early times following excitation on resonance with the ^1A_g to ^1B_u electronic transition (**Figure 6-1**).[12,13] Photoexcitation was at 350 nm, which, despite the red shift in the absorption spectrum with oligomer length that has been previously reported[12,14] indicating the increase in conjugation length, is sufficiently energetic to provide significant excited state population.
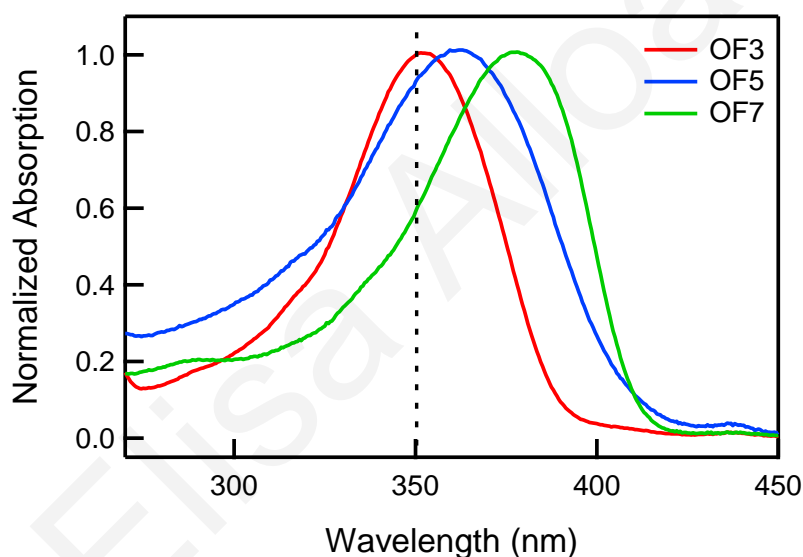
Figure 6-1 Absorption spectra of the three oligomers in dichloromethane solution. The actinic pump wavelength of excitation is indicated by the dashed line.

Transient absorption (TA) spectroscopy was employed first to establish the spectral region for the excited state absorption and thus the Raman pump excitation wavelength, but also to provide the overall dynamics of the excited state. Any spectral evolution observed in the TA spectra can then be correlated to structural evolution obtained from the FSRS spectra. In **Figure 6-2** an exceptional bandshape evolution of the TA spectra of the trimer is observed with delay time. A large change in vibronic intensities is accompanied by significant narrowing of the band: in particular, the 0-0/0-1 relative intensities are gradually modified and the spacing between the vibronic bands narrows with time, suggesting a large geometry change over time in the ^1B_u excited state.
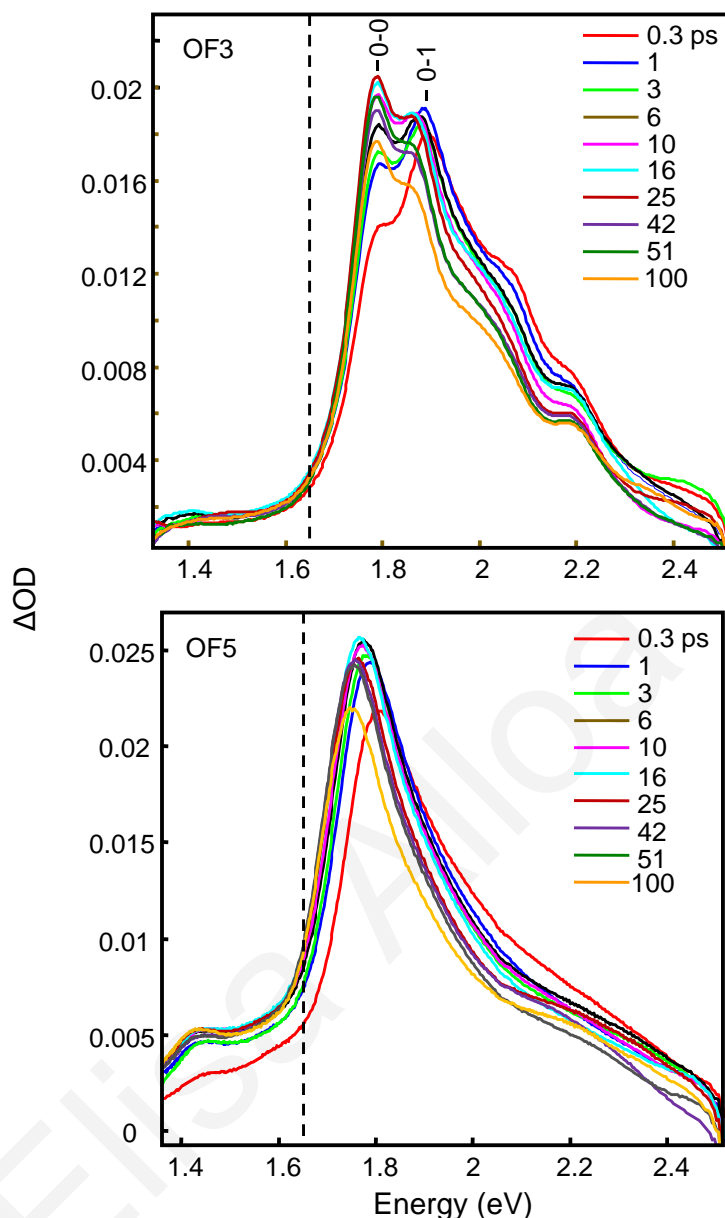
Figure 6-2 Transient absorption spectra of OF3 and OF5 in chloroform solution following excitation at 350 nm. The dashed line denotes the Raman pump excitation energy.

While the red shift of the absorption spectrum with time had been observed previously,[11,15] the detailed vibronic intensity evolution has not been observed before, possibly due to technical difficulties (usually the whitelight is produced with 800 nm, so this spectral region is obscured). Contrary to the trimer, only a shift to lower energies is observed for the unstructured excited state absorption band of OF5 (**Figure 6-2**) and OF7 (not shown) reflecting a smaller structural change with time. Insights on the origin of the excited state evolution and any conformational changes on the time scales observed in the TA experiments can be provided from FSRS spectra of the oligomers. The trimer FSRS spectra

appear in **Figure 6-3**. Similar to the ground state Raman spectra[16] a number of bands appear between 800 and 1700 cm^{-1} (see **Table 6-1**).
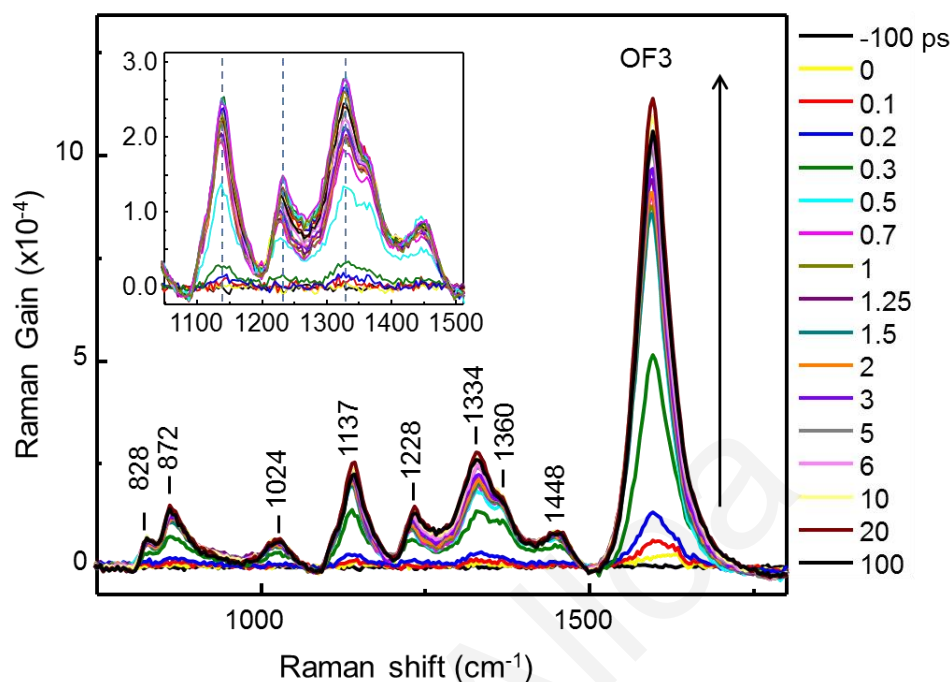
Figure 6-3 FSRS spectra of OF3 as a function of time delay. Inset: zoom of selected area (1000-1500 cm^{-1}).

Frequencies observed are generally slightly higher compared to the ground state spectra. The most intense band appears at 1594 cm^{-1} and is assigned to phenyl ring C-C symmetric stretching. In the ground state, this strong band appears at 1609 cm^{-1}. Such a decrease in the frequency of the C-C stretching mode of the aromatic rings in fluorenes and other phenylene-type polymers was observed in doping studies, where the fluorene/phenylene ring assumes a quinoidal conformation.[17,18] Bands between 1100 and 1400 cm^{-1} can be assigned to C-C and C=C stretching either between the monomer units or in the fluorene phenyl rings, or C-H bending. **Table 6-1** illustrates the assignments for the ground and excited state bands observed in the spectra according to the literature.[19]

An overall increase in the intensity of all the bands is observed as a function of delay time. Comparison of the kinetics of the intensity increase of the aromatic C=C stretching mode at 1595 cm^{-1} to the kinetics of the excited state absorption edge at 1.45 eV (**Figure 6-4**) suggests that this increase can be associated with resonance Raman cross section enhancement due to a red shift in the excited state absorption.

Table 6-1 Ground and excited state frequencies for the main bands observed in RR and FSRS spectra of oligofluorenes.

X^1A_g (cm^{-1})[4]	^1B_u (0.3 ps) (cm^{-1})	Assignment
	422	Ring torsion
732		phenyl ring breathing
	828	
862	872	C-C stretch (bridging C)
1024	1024	C-H in-plane bend
1220	1228	C-C inter-ring stretch
1134	1136	C-H in-plane bend; ring distortion
1280	1330	C-C stretch between monomers
1345	1363	C-C stretch between phenyls
1452	1451	phenyl C-H rock; side chain C-H bend
1582		as phenyl ring C-C stretch
1609	1594	s phenyl ring C-C stretch

Vibrational cooling can also contribute to an increase in the Raman cross section. However, the contribution of thermal effects should be minor if we consider the contribution of cooling
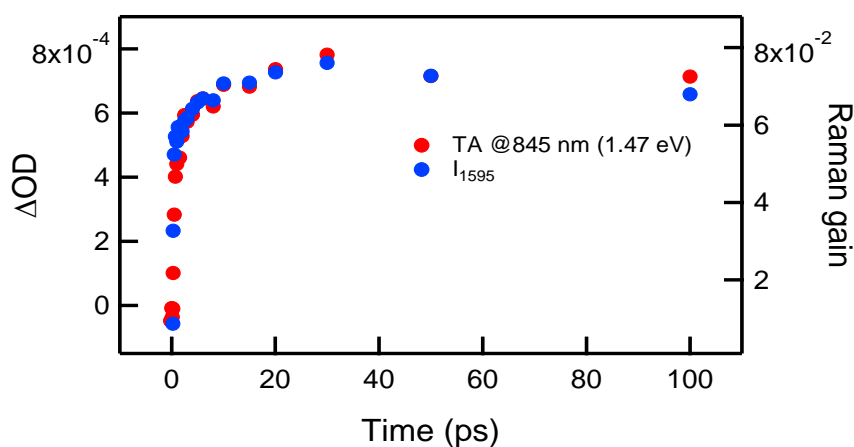
Figure 6-4 Comparison of the kinetics of the red edge of the excited state absorption (FSRS spectral region) and the intensity of the aromatic C=C stretching mode at 1595 cm^{-1}.

on the Raman cross section, especially when excitation is on the red edge of the excited state absorption band.[20] This can also be discounted based on the different extent of intensity increase among peaks observed and the clear correlation of peak shifts to structural changes (see below).
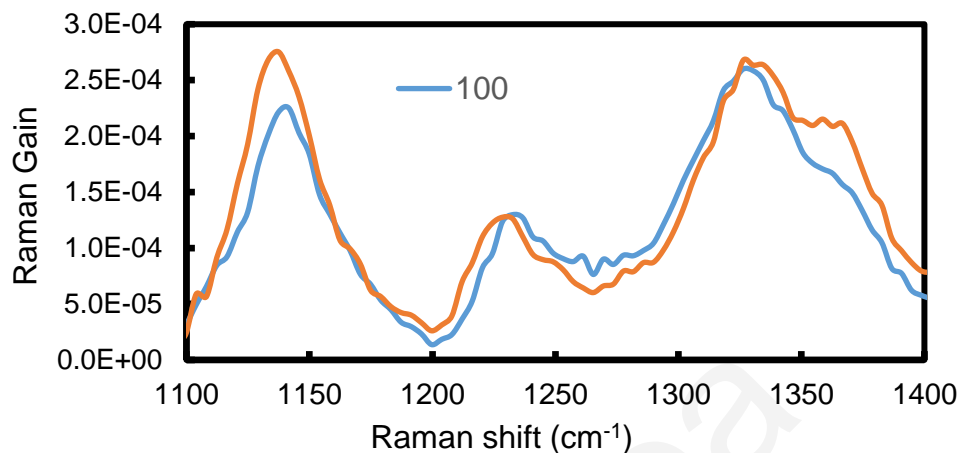
Figure 6-5 Comparison of peak positions and relative intensities in the FSRS spectra of OF3. The 100 ps spectrum is compared to the average of early time delays <0.5 ps.

In order to get insights on the excited state conformational evolution of the trimer, a closer look of the 1100 to 1400 cm^{-1} region is instructive. Comparison of the early and later time FSRS spectra reveals a shift to higher frequencies for the 1137 and 1228 cm^{-1} bands that correspond to C-H in-plane bending and C-C inter-ring stretch, respectively, and a decreased intensity by 100 ps for the 1137 and 1360 cm^{-1} bands (**Figure 6-5**). A decrease in frequency is, however, observed for the ~868 cm^{-1} bridging carbon C-C stretch (**Figure 6-3**). An increase in frequency of certain vibrational bands with time and decrease of others can be associated with conformational change in the molecule. Theoretical calculation of the ^1B_u molecular orbital of terfluorene indicates a shift in electron density from an aromatic to a quinoidal conformation,[4] with an alternation in single and double bonds. In this case, electron density in the bridging carbon C-C bonds is reduced compared to the ground state and should be associated with lower frequencies, while increased density in certain C-C bonds along the long axis of the molecule should be depicted in the vibrational spectra as an increase in frequency. The shift in the 1228 cm^{-1} inter-ring C-C stretch to 1235 cm^{-1}, the ring C-H in-plane bend from 1137 to 1140 cm^{-1} (**Figure 6-6**), and the phenyl ring symmetric C-C stretch from 1594 to 1598 cm^{-1} can be associated with such structural changes reflecting C-C bonds acquiring double-bond character with time. Similar dynamics are observed for the shifts in the 1137 and 1228 cm^{-1} modes, further corroborating their involvement in a concerted conformational change. Inconsistent with these observations is the decrease of the
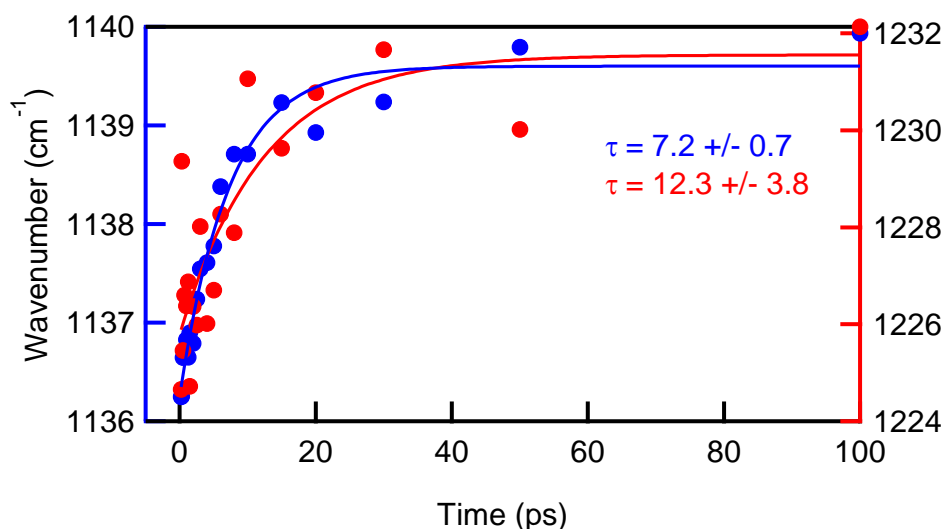
Figure 6-6 Time dependence of the 1137 and 1228 cm^{-1} mode shifts in OF3. Similar shifts but to a smaller extent are observed in OF5 and OF7.

frequency of the 1334 cm^{-1} mode, assigned to the C-C stretch between monomers, which is expected to gain double-bond character upon planarization of the oligomer. This discrepancy can be due to the spectral congestion in this region, or a matter of mode assignments. Theoretical Raman calculations of the excited state are currently underway that will address these issues.
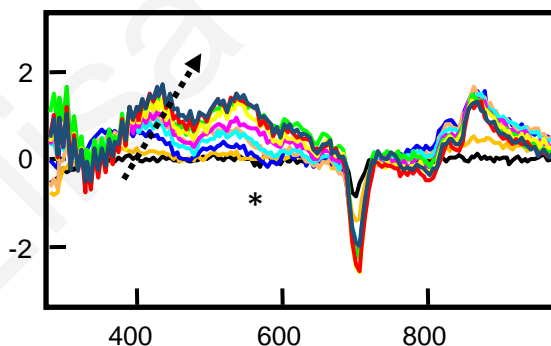
Figure 6-7 FSRS spectra of OF3 as a function of time delay in the low frequency region. The arrow shows the direction of the shift of the torsional mode with time (0.3 – 100 ps).

Torsional relaxation can be directly monitored observing changes in the frequency of torsional and out-of plane modes at low frequencies (reported at 420 and 480 cm^{-1} in ground state Raman spectra of oligofluorenes).[16] This region is difficult to access unequivocally in the FSRS spectra as it is quite close to the Raman pump and background subtraction can produce artifacts. However, in the case of OF3 we indeed observed an upshift in these bands (**Figure 6-7**).

Previous work on fluorene oligomers has shown that conformational changes related to the backbone torsional angle can be also observed by monitoring the frequency of the C-C stretch between fluorene monomers and the relative intensity of the C-H bend with respect to the C-C stretch.[13] Therefore torsional relaxation can be monitored in the FSRS through the temporal evolution of the ratio between intensities for the 1137 to the 1228 and 1334
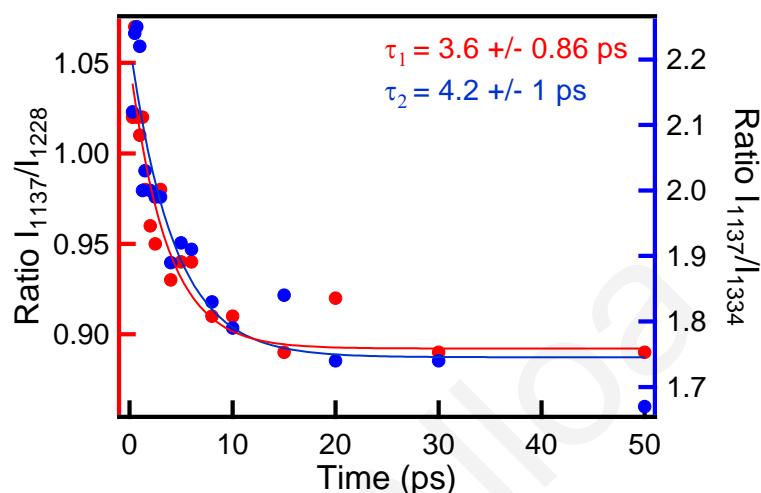
Figure 6-8 Time dependence of the ratio of intensities for the 1137 to the 1228 and 1334 cm^{-1} modes in OF3
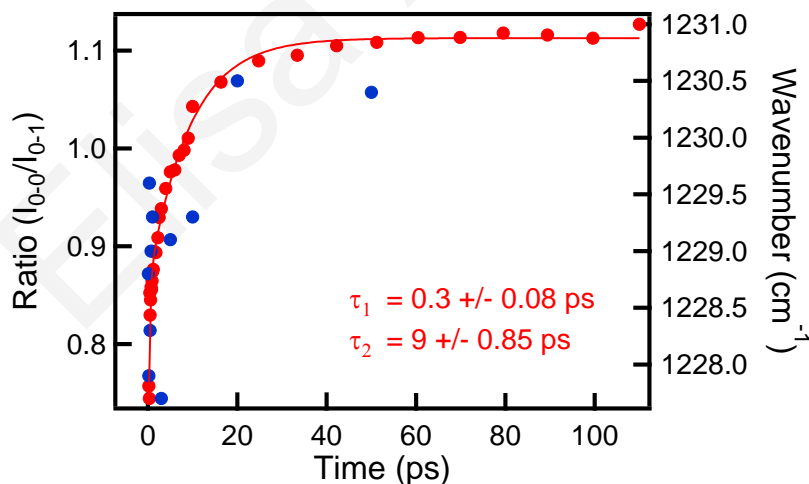
Figure 6-9 Time dependence of the ratio of the 0-0 to 0-1 vibronic intensities from the TA spectra of OF3 (red). The kinetics of this ratio is compared to the kinetics of the frequency change of the 1228 cm^{-1} mode (blue).

cm^{-1} modes (**Figure 6-8**), where the same trend appears for both ratios with a similar time constant, suggesting correlated processes. Changes can also be observed in the relative intensities of bands related to the C-C stretching modes associated with the carbons connecting monomers in the oligomer (1330 cm^{-1}) and carbons connecting the phenyls inside the monomer unit (1360 cm^{-1}) (**Figure 6-4**). Their relative intensity change with time is

additional proof of the concerted conformational change that takes place along the oligomer chain.[21,22] The sum of all these observations suggest that indeed following excitation the conformation changes from benzenoid to quinoidal with time. Shifts observed in the FSRS experiment were compared to the evolution in the TA spectrum in order to obtain insights about the contribution of structural changes to the optical spectral evolution. **Figure 6-9** compares the temporal evolution of the 0-0/0-1 intensity ratio in the TA spectra of OF3 to the blue shift in the 1228 cm^{-1} band (inter-ring C-C stretch), indicative of the evolution towards a quinoidal structure. The temporal evolution of the 0-0/0-1 ratio was fit to a sum of two exponentials with a 300 fs and a 9 ps time constant. The picosecond process can be related to the kinetics observed above for several of the Raman bands in the FSRS spectra. Comparison with the kinetics of the 1228 cm^{-1} mode shift indicates that the change in the 0-0/0-1 ratio is indeed related to conformational change in the trimer, pointing to torsional relaxation. After 10 ps the OF3 structure appears stabilized, with no significant frequency changes, in agreement with the OF3 TA spectra. The femtosecond process may then be ascribed to exciton self-trapping.
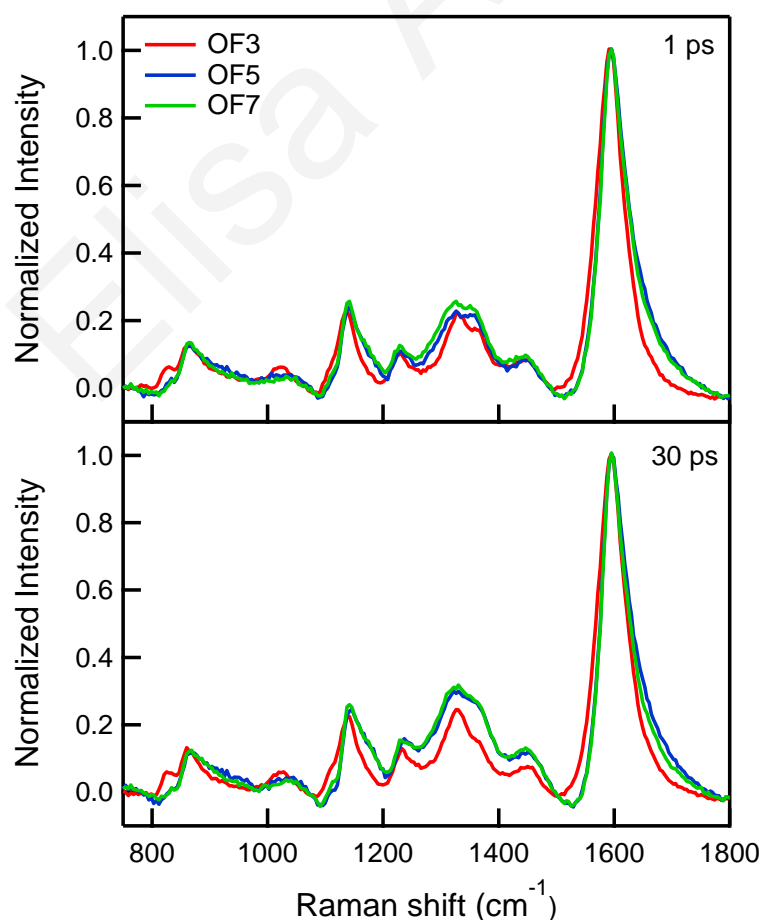
Figure 6-8 Comparison of the 1 and 30 ps spectra of the three oligomers.

A comparison of the FSRS spectra at early and later delay times for the three oligomers is shown in **Figure 6-10**.The spectra appear almost identical. Differences appear mainly in relative band intensities in the 1200-1400 cm^{-1} region. **Figure 6-11** clearly demonstrates that OF3 sustains the largest change in 1330/1360 relative intensities within the first 10 ps, while the pentamer and heptamer follow the same trends. This may be attributed to a greater potential well displacement in the case of OF3, due to a more twisted ground state conformation. A faster relaxation occurs for the longer length oligomers, due to a smaller excited state evolution since they start at a smaller dihedral angle than the trimer,[23] consistent with the small evolution of the TA spectra (**Figure 6-2**). Previous work on the ground state Raman spectra of these oligomers, showed a slight variation with the length of the side chain in this spectral region.[19] Both the pentamer and the hexamer have hexyl side chains, while the trimer has octyl side-chains. However, the temporal evolution of the 1330/1360 relative intensities for all oligomers indicates that this stems from a dynamic process related to the backbone planarization (as also seen from the shifts in the 1600 cm^{-1} mode, see below) and not the difference in the chain-length. In addition, Kang et al. showed that the length of the side chains in solutions of oligofluorenes (for lengths between 4 and 9 carbons) does not affect the fluorescence spectrum, nor the excited state lifetime, thus, we can exclude any aggregates playing a role in the FSRS spectra we observe, nor their temporal evolution.[24]
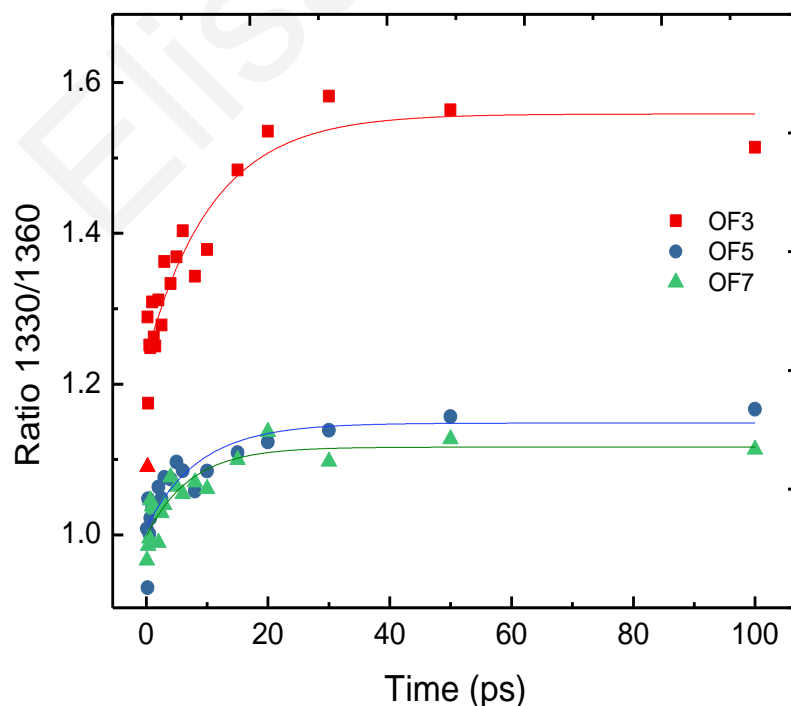
Figure 6-9 Temporal evolution of the ratio of intensities for the 1330 to the 1360 cm^{-1} modes.

The time dependence of the 1595 cm^{-1} phenyl ring symmetric C-C stretch frequency is shown in **Figure 6-12** for the three oligomers. In the case of the trimer the frequency drops initially ~2 cm^{-1} to 1593 cm^{-1} at very early times following photoexcitation(<1 ps) and subsequently increases to 1595 cm^{-1} on the 9 ps timescale, similarly to the evolution observed in other vibrational modes in OF3. For longer oligomers most of the evolution occurs within the first picosecond with a 4 cm^{-1} downshift to 1595 cm^{-1} with limited subsequent change. This initial ultrafast decrease in the C-C stretch frequency could be associated with exciton self-trapping
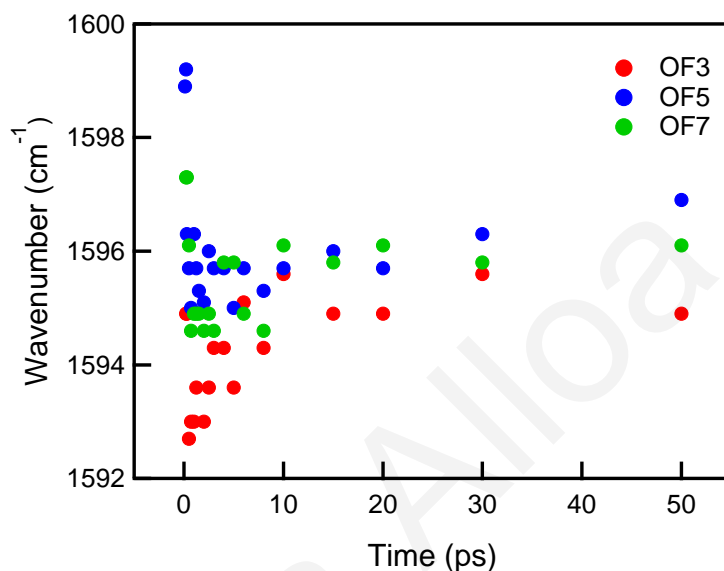
Figure 6-10 Time dependence of the phenyl ring symmetric C-C stretch frequency in the three oligomers.
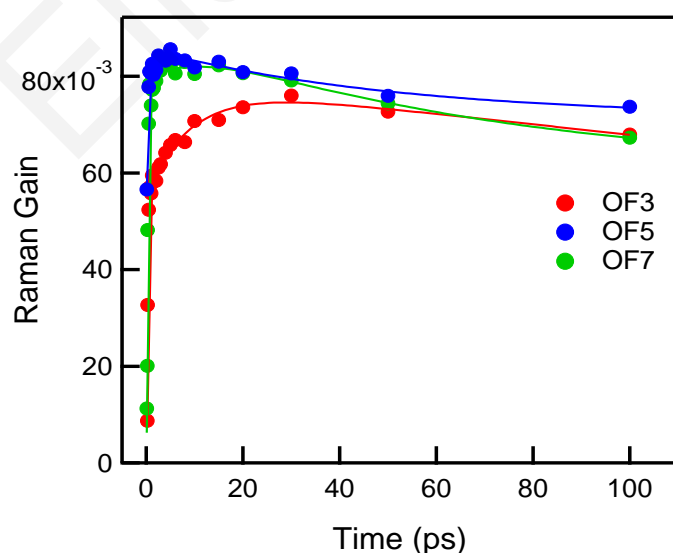
Figure 6-11 Time dependence of the phenyl ring symmetric C-C stretch intensity as a function of oligomer length (used area of peak). **Table 6-2** shows the standard deviations of the curves.

Table 6-2 Time constants for the fits to the kinetics curves in **Figure 6-13**.

	OF3	**OF5**	**OF7**
τ_1	0.136 +/- 0.011 ps	0.154 +/- 0.075 ps	0.246 +/- 0.037 ps
τ_2	9.30 +/- 1.67 ps	1.95 +/- 1.42 ps	

with the subsequent increase on the picosecond timescale associated with dynamic planarization to a quinoidal structure. The time dependence of the 1595 cm^{-1} band intensity follows a similar trend to the peak shifts as a function of oligomer length (**Figure 6-13, Table 6-2**). We observe that most of the intensity evolution occurs on <1 ps timescales, with an increase in intensity at very early times, which is faster for the longer oligomers.

The reorganization process as probed by the phenyl ring C-C stretches seems to vary between the trimer and longer oligomers. While many studies[25–28] discriminate between an ultrafast exciton self-trapping on a subpicosecond time scale and a dynamic planarization process occurring over the next few tens-hundreds of picoseconds, the effect of chain length on exciton dynamics in linear oligomers has still not been well characterized.[25,29] According to Kim et al.[25,30] conformational disorder increases by increasing the chain length and ultrafast localization could be excluded in short oligomers. Considering, however, that this study is based on linear oligothiophenes connected with ethynylene linkers up to 10-mer, i.e. the biggest oligothiophene monomer corresponding to approximately the OF trimer in our study, our observations are in agreement with this work. It is indeed obvious, especially from the dynamics of the 1595 cm^{-1} band, that this localization is more prevalent in the longer oligomers.

Another study carried out in solutions of dimer, hexamer, and closed ring carbazole-bridged phenylene-ethynylene-butadiynylene based systems[28] indicate a similar extent in the emission for all three systems, and this relates to our observations. A significant spectral red shift in the emission peak of the dimer only happens within 100 ps after excitation, thus has been attributed to torsional relaxation, and considered hampered in the hexamer due to its larger size and in the macrocycle because of structural rigidity. This differences in the spectral shift could correlate also to our findings, as in the longer oligomers very limited shifts are observed after the ultrafast initial response.

6.3 Conclusions

We have obtained time-resolved excited state stimulated RR spectra for a series of oligofluorenes for the first time, simultaneously with TA, which enables correlation of specific structural dynamics with dynamics observed with optical time-resolved spectroscopies. Through FSRS spectroscopy we were able to directly observe mode-specific dynamics that provide insight on excited state evolution. Blue shifting of particular modes with time correlates with increase in the double bond character of C-C bonds , such as the 1228 cm^{-1} inter-ring C-C stretch, indicative of a transition from a twisted benzenoid conformation to a more planar quinoidal geometry. Other metrics, such as the I_{1334}/I_{1360} ratio, collaborate to reach the conclusion that torsional relaxation is a major process in this set of oligomers that occurs on the 9 ps timescale. In this work we were able to directly correlate the structural dynamics in the oligomers to the evolution of the excited state absorption band. We find that the torsional relaxation is more pronounced in the trimer, suggesting that it undergoes a greater potential well displacement due to a more twisted ground state conformation. In addition, an ultrafast sub-ps process is observed that may be direct evidence for exciton self-trapping. Overall, our results offer a much needed direct view for the excited state evolution, with structural detail that is not possible from optical spectroscopies.

References

1. Mathies, R. A. Femtosecond stimulated Raman spectroscopy. *Opt. InfoBase Conf. Pap.* **58,** 461–88 (2007).

2. Dietze, D. R. & Mathies, R. A. Femtosecond stimulated Raman spectroscopy. *ChemPhysChem* **17,** 1224–1251 (2016).

3. Frontiera, R. R. & Mathies, R. A. Femtosecond stimulated Raman spectroscopy. *Laser Photon. Rev.* **5,** 102–113 (2011).

4. Zhou, J., Yu, W. & Bragg, A. E. Structural relaxation of photoexcited quaterthiophenes probed with vibrational specificity. *J. Phys. Chem. Lett.* **6,** 3496–3502 (2015).

5. Shim, S., Stuart, C. M. & Mathies, R. A. Resonance Raman cross-sections and vibronic analysis of rhodamine 6G from broadband stimulated Raman spectroscopy. *ChemPhysChem* **9,** 697–699 (2008).

6. Yoshizawa, M., Aoki, H. & Hashimoto, H. Vibrational relaxation of the 2 A−g excited state in all-trans-β-carotene obtained by femtosecond time-resolved Raman spectroscopy. *Phys. Rev. B - Condens. Matter Mater. Phys.* **63,** (2001).

7. Provencher, F. *et al.* Direct observation of ultrafast long-range charge separation at polymer-fullerene heterojunctions. *Nat. Commun.* **5,** 4288 (2014).

8. Takaya, T., Enokida, I., Furukawa, Y. & Iwata, K. Direct observation of structure and dynamics of photogenerated charge carriers in poly(3-hexylthiophene) films by femtosecond time-resolved near-IR inverse Raman spectroscopy. *Molecules* **24,** (2019).

9. Ling, S., Schumacher, S., Galbraith, I. & Paterson, M. J. Excited-state absorption of conjugated polymers in the near-infrared and visible: A computational study of oligofluorenes. *J. Phys. Chem. C* **117,** 6889–6895 (2013).

10. Denis, J. C. *et al.* Self-trapping and excited state absorption in fluorene homo-polymer and copolymers with benzothiadiazole and tri-phenylamine. *Phys. Chem. Chem. Phys.* **18,** 21937–21948 (2016).

11. Hintschich, S. I., Dias, F. B. & Monkman, A. P. Dynamics of conformational relaxation in photoexcited oligofluorenes and polyfluorene. *Phys. Rev. B - Condens.*

Matter Mater. Phys. **74,** 1–10 (2006).

12. Hayes, S. C. & Silva, C. Analysis of the excited-state absorption spectral bandshape of oligofluorenes. *J. Chem. Phys.* **132,** 1–10 (2010).

13. Itoh, T. Franck-Condon analysis of the absorption and fluorescence spectra of all trans α,ω-diphenylpolyenes with one to seven polyene double bonds. *J. Chem. Phys.* **123,** 0–6 (2005).

14. Chi, C., Im, C. & Wegner, G. Lifetime determination of fluorescence and phosphorescence of a series of oligofluorenes. *J. Chem. Phys.* **124,** (2006).

15. Clark, J., Nelson, T., Tretiak, S., Cirmi, G. & Lanzani, G. Femtosecond torsional relaxation. *Nat. Phys.* **8,** 225–231 (2012).

16. Tsoi, W. C. & Lidzey, D. G. Raman spectroscopy of fluorene oligomers in the α-, β- And γ-phases. *J. Phys. Condens. Matter* **20,** 321 (2008).

17. Fujitsuka, M., Cho, D. W., Huang, H. H., Yang, J. S. & Majima, T. Structural relaxation in the singlet excited state of star-shaped oligofluorenes having a truxene or isotruxene as a core. *J. Phys. Chem. B* **115,** 13502–13507 (2011).

18. Sakamoto, A., Furukawa, Y. & Tasumi, M. Resonance Raman characterization of polarons and bipolarons in sodium-doped poly(p-phenylenevinylene). *J. Phys. Chem.* **96,** 3870–3874 (1992).

19. Tsoi, W. C. & Lidzey, D. G. Raman spectroscopy of fluorene oligomers in the α-, β- And γ-phases. *J. Phys. Condens. Matter* **20,** 125213 (2008).

20. Shreve, A. P. & Mathies, R. A. Thermal effects in resonance Raman scattering: Analysis of the Raman intensities of rhodopsin and of the time-resolved Raman scattering of bacteriorhodopsin. *J. Phys. Chem.* **99,** 7285–7299 (1995).

21. Volz, C., Arif, M. & Guha, S. Conformations in dioctyl substituted polyfluorene: A combined theoretical and experimental Raman scattering study. *J. Chem. Phys.* **126,** 122 (2007).

22. Cuff, L. & Kertesz, M. Theoretical prediction of the vibrational spectrum of fluorene and planarized poly(p-phenylene). *J. Phys. Chem.* **98,** 12223–12231 (1994).

23. Bird, M. J. *et al.* Mobility of holes in oligo- and polyfluorenes of defined lengths. *J. Phys. Chem. C* **118,** 6100–6109 (2014).

24.   Kang, J. *et al.* Time-resolved photoluminescence study of low-energy emission mechanisms in oligofluorene and polyfluorene films. *Polymer (Guildf).* **49,** 5700–5704 (2008).

25.   Park, K. H., Kim, W., Yang, J. & Kim, D. Excited-state structural relaxation and exciton delocalization dynamics in linear and cyclic p-conjugated oligothiophenes. *Chem. Soc. Rev* **47,** 4279 (2018).

26.   Kim, P. *et al.* Relationship between dynamic planarization processes and exciton delocalization in cyclic oligothiophenes. *J. Phys. Chem. Lett.* **6,** 451–456 (2015).

27.   Park, K. H. *et al.* Excited-state dynamic planarization of cyclic oligothiophenes in the vicinity of a ring-to-linear excitonic behavioral turning point. *Angew. Chemie - Int. Ed.* **54,** 12711–12715 (2015).

28.   Thiessen, A. *et al.* Exciton localization in extended π-electron systems: Comparison of linear and cyclic structures. *J. Phys. Chem. B* **119,** 9949–9958 (2015).

29.   Chang, M. H., Hoffmann, M., Anderson, H. L. & Herz, L. M. Dynamics of excited-state conformational relaxation and electronic delocalization in conjugated porphyrin oligomers. *J. Am. Chem. Soc.* **130,** 10171–10178 (2008).

30.   Kim, T. W. *et al.* Chain-length dependent exciton dynamics in linear oligothiophenes probed using ensemble and single-molecule spectroscopy. *J. Phys. Chem. Lett.* **7,** 452–458 (2016).

CHAPTER 7

Development of a Stimulated/Inverse Raman optical setup

7.1 Stimulated/inverse Raman spectroscopy: technique development

The need to measure Raman spectra of fluorescent samples (such as PBIs) led us to the development of a method based on stimulated Raman scattering. Picosecond / nanosecond pulses and photonic fibers are used for this purpose. A collaboration with the University of Valencia was established in order to obtain appropriate optical fibers to generate the supercontinuum light, which is necessary in this technique as a probe pulse. A pump is accordingly coupled and synchronized with the probe in time and space. Depending on the excitation wavelength used, gains or losses can be monitored in the spectrum, obtaining, respectively, the stimulated or inverse Raman. While stimulated Raman can be used to quench the fluorescence from technologically important molecule whose structure deems investigation, inverse Raman (the loss signal) can be exploited itself for technological purposes.

All-optical switching is progressively complementing electrical switching for optoelectronic systems in communication technology.[1] The increased operating speed and negligible absorptive losses favor all-optical switching to become a widely required application. In general, an optical switch involves three components: the signal beam, the control beam and the medium through which the switching operation is carried out. Previous attempts for all-optical switching were observed in a silicon waveguide, which could indeed be a valuable tool for chip-scale signal processing. However, silicon support suffers from additional losses due to two-photon induced absorption.[2] Glass optical fibers do not manifest this inconvenience, plus are exploitable in the optical communication network, which is largely based on optical fibers. The achieved level of attenuation in an optical fiber via IRS, considering both experimental data and theoretical calculations, is > 20dB at a time scale < 5ps.[1,3] Further improvements in the field compared to standard glass optical fibers are represented by liquid-core optical fibers (LCOF), where the fiber is infiltrated with liquids (e.g. neat CS_2 liquid, or β-carotene in CCl_4). Inverse Raman scattering in those liquids

produces a narrowband Raman loss signal over the broadband continuum that can simulate a switching process. The LCOF platform unlocks new potentials for ultralow power nonlinear optics such as slow light generation and signal amplification, efficient white light generation for displays and wavelength-division-multiplexed applications.[3] Liquids moreover may exhibit intense Raman loss coefficients, which help reduce the pump power by at least an order of magnitude. Further developments with highly soluble organic compounds possessing large Raman cross sections are still in progress,[4] and the organic system that will be employed from this thesis work onwards goes precisely in this direction.

PCDA[5,6] coupled to nanoparticles[7,8] synthesized during my training at the University of Genova, will be used for the first time for this purpose. The intense and well-defined Raman spectrum of PCDA can be advantageously exploited for all-optical switching applications, enriching the current state-of-the-art for liquid photonics based on integrated LCOF, which is still at its early stages of development.

Supercontinuum laser light was generated by coupling the laser beam into an optical fiber, responsible for the conversion to white light. Different optical fibers were tested in order to choose a proper one, i.e. with the widest possible conversion wavelength range.

7.2 Results

The first trials concentrated on a commercial fiber in order to focus the light inside the fiber. Two excitation wavelengths have been used for this purpose, 1064 and 532 nm.
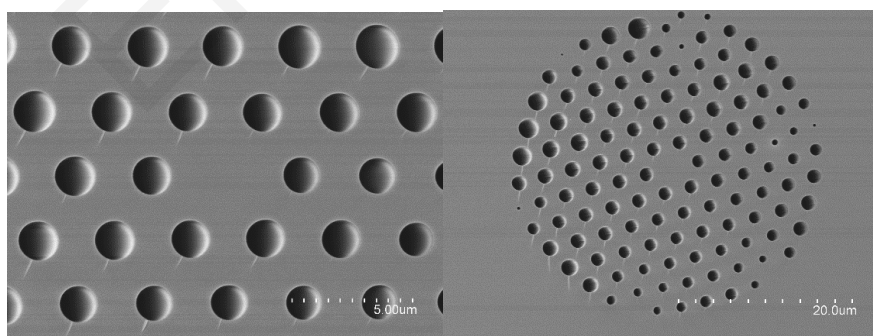
Figure 7-1 SEM images of the selected fiber for the stimulated/inverse Raman.

Once a proper alignment was obtained, a variety of different fibers (synthesized at the University of Valencia) were measured in order to compare their resulting spectra with the maximum average intensity that was possible to be conveyed through the fiber. A representation of the specific inner core pattern of the fiber used in our experiments is

depicted in the SEM images of **Figure 7-1**. The material which constitutes the fiber is amorphous SiO_2 and its structure is triangular. Parameters which define the structure of the fiber are: the diameter of the holes (d) and the separation among holes (Λ). Calculated values from the SEM image are:

- $\Lambda = 3.17$ µm
- $d = 1.68$ µm
- $\dfrac{d}{\Lambda} = 0.53$

These parameters are characteristic of each manufactured fiber and can be related to the outcoming laser light.
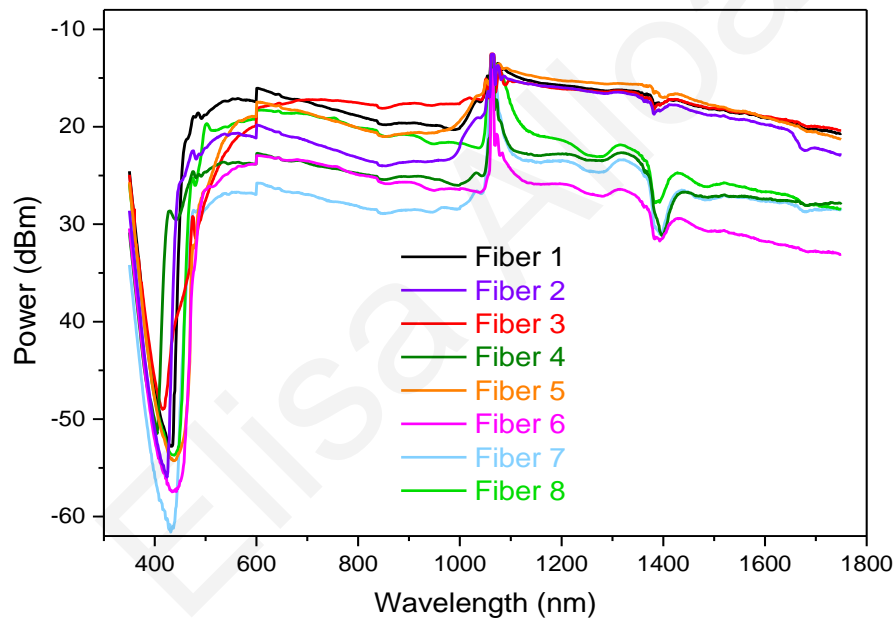
Figure 7-2 Spectrum of the generated supercontinuum from a variety of fibers tested.

Figure 7-2 represents the spectra of the generated supercontinuum light from different fibers provided from the University of Valencia to be tested and used at UCY. The aim here was to check the fibers for their ability to convert light from monochromatic to continuum and for the power intensity that each of these were able to convey. All thefibers show a similar trend, which is suitable for our purpose. The usable wavelength range that we generated extends from 450-500 nm to 1000 nm. The selected fibers, according to the most powerful light continuum achieved, were 1, 2 and 8.

In the system developed at UCY a nanosecond pulse is employed, thus making the conversion to whitelight more challenging to obtain. Initially generation of whitelight was performed with the 532 nm beam alone; however, the obtained whitelight range was too narrow and the output had very distinct structure (**Figure 7-3**). We subsequently switched to a 1064 nm pump and it was then possible to get a broad continuum with Fiber 8, probably because of its longer length and a more suitable inner microstructure, compared to the other fibers.
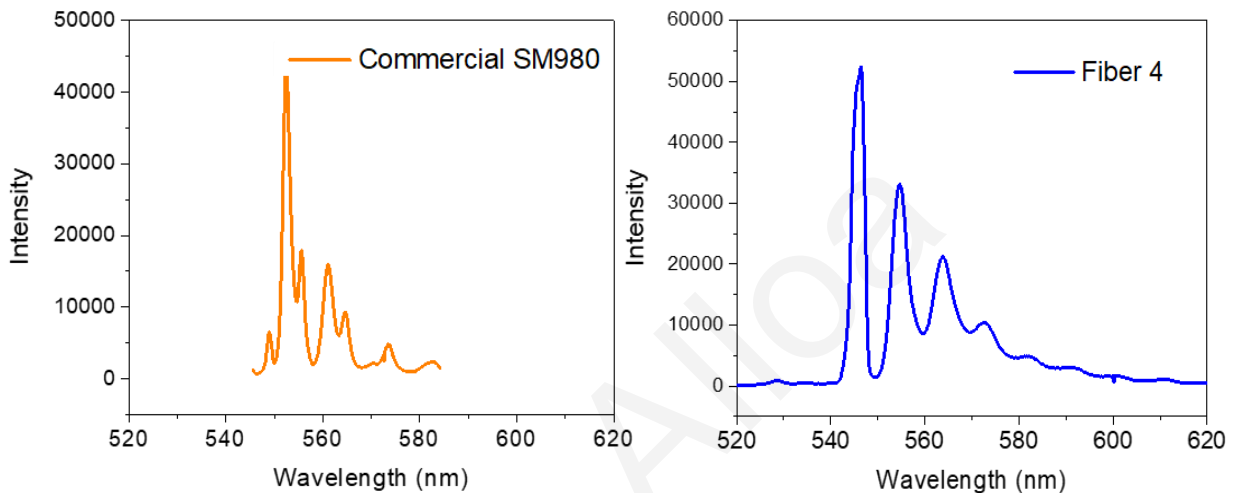
Figure 7-3 Broadband light generation with a 532 nm laser source for a commercial and a manufactured fiber. A notch filter is employed here to block the excitation beam before entering the spectrograph.

In the SRS/IRS experiment a Raman pump beam is necessary to be synchronized both in time and space with the whitelight in order to generate the stimulated process. As the photonic fiber medium generates a significant delay (of around 30-50 ns, depending on the length of the fiber) of the 1064 nm pulses, the synchronization with the Raman pump cannot be done optically. The only other two ways to synchronize the two pulses are either electronically with a delay generator, or to introduce the Raman pump through a similar medium as the 1064 nm light that will induce a similar pulse delay. As the available Raman pump pulse was generated from the same Nd:YAG laser as the 1064 nm, electronic delay was not an option. Therefore, the 532 nm excitation was also passed through the fiber collinearly with the IR component.

Figure 7-4 depicts the generated continuum with and without 532 nm pump (a notch filter was placed before the spectrograph to block this component) using different gratings. The continuum depicted ranges from around 400 nm up to approximately 575 nm. An extension

of the whitelight continuum to higher wavelengths (up to 600 nm) would be profitable for our experiment to be in resonance with the absorption of the PCDA (see **Figure 7-5**).
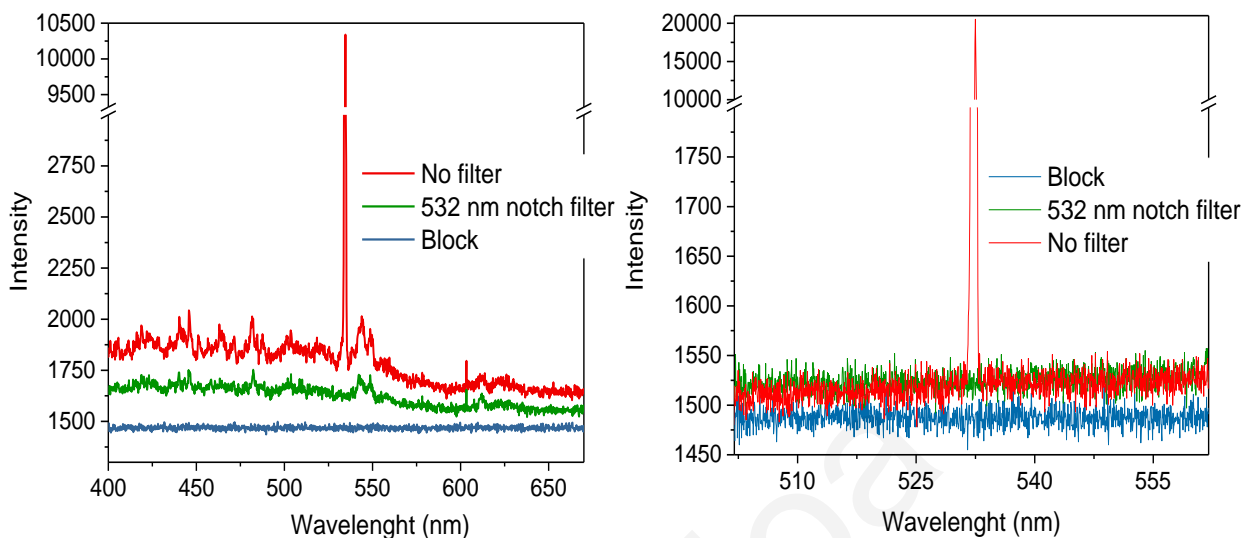
Figure 7-4 Generated whitelight from a 1064 nm laser source, coupled with the excitation pump at 532 nm ('No filter') or alone ('532 nm notch filter'). 'Block' is the comparative spectrum where the transmitted light is stopped (after the fiber). **Left:** 1200 lines/mm grating. **Right:** 300 lines/mm grating.

Maximum laser powers for the incoming beam of 1.5 mW (being 0.85 mW the IR component alone) show no damage to the fiber. In such conditions, the maximum achieved power for the beam coming out of the fiber was around 0.15 mW for the full spectrum of whitelight and 532 nm component (being 0.08 mW the whitelight supercontinuum alone).

The next step was to see if the generated whitelight continuum along with the Raman pump at 532 nm could generate stimulated Raman signal from a solvent. A sample with carbon tetrachloride was placed either inside a 1 cm cell or in a longer capillary (in order to increase the pathlength). However no signal appeared in either case, nor in the stimulated, nor in the inverse Raman range. This is probably due to the short pathlength of the sample cell, and to the low power of the Raman pump used, limited by the optical fiber.

7.3 PCDA samples

PCDA was chosen in this project because of its intense vibrational signal: the large Raman cross-section of its double and triple bonds, together with the surface enhancement due to the coupled nanoparticles, makes this polymer suitable for the purpose of assessing the

SRS/IRS technique. Different solutions of PCDA were prepared for use with this new technique we aim to develop (see **Figure 2-26**). PCDA solutions were characterized with absorption spectroscopy during the synthesis and compared, in order to monitor peaks from the different components (gold and silver plasmons, blue and red PCDA excitons), as shown in **Figure 7-5**. Three solutions were analyzed: one with PCDA alone ('PCDA_Chit'), one with PCDA attached to gold NPs ('PCDA_Au') and one with PCDA attached to silver NPs ('PCDA_Ag'). UV-vis spectra of these solutions were obtained before polymerization ('NOpol'), after polymerization, i.e. with the PCDA polymer in its blue phase ('pol') and after the heating procedure, i.e. with the PCDA in its red phase ('Red'). Moreover, in order to compare these spectra with the ones from NPs alone, absorption spectra of AuNPs and Ag NPs colloidal solutions were also recorded. The bands we observed are in line with previous literature studies.[7,8]

The silver plasmon band is centered around 420 nm; the gold plasmon occurs at 550 nm; the blue phase shows its typical absorption peaks at 640 nm and 665 nm (together with its first vibrational sideband around 560 nm); the red phases appear at 505 and 550 nm (showing up together with the gold plasmon).
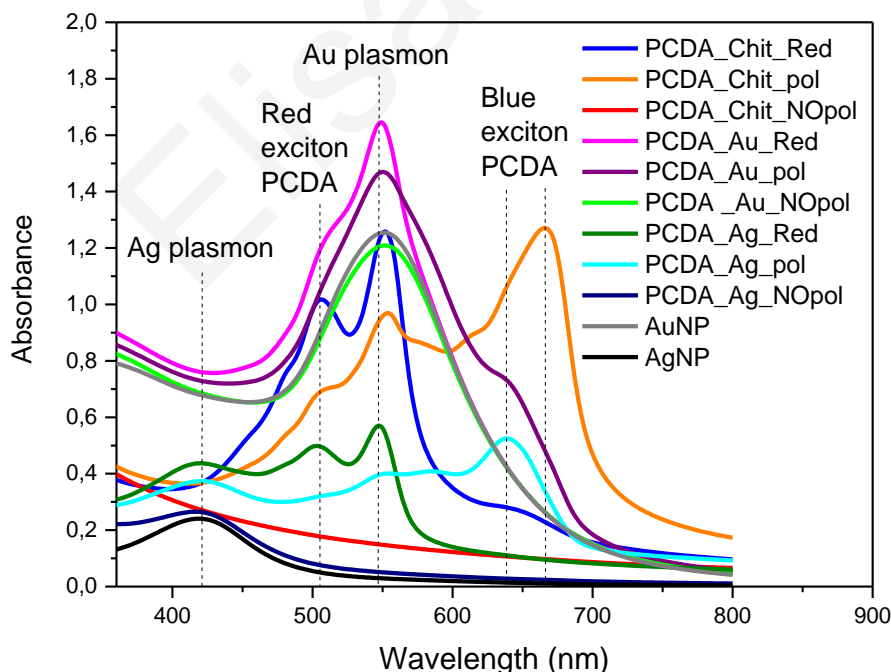
Figure 7-5 UV-vis spectra of PCDA along the synthesis procedure.

According to the absorption bands observed and to the SRS/IRS experiment planned, a Raman pump at 532 nm will be in resonance with the PCDA, and more specifically with its red exciton and with the gold plasmon. Resonance enhancement will further increase the loss signal we expect to see, beyond the surface enhancement due to coupling of PCDA to gold nanoparticles. Therefore, AuNPs-PCDA in its red phase (submitted to thermal treatment, see *Chapter 2-3*) is the candidate of choice for our future experimental setup.

7.4 Conclusions

Supercontinuum laser light was generated by coupling a laser beam at 1064 nm into an optical fiber, responsible for the conversion to white light. This whitelight was then coupled into the fiber with a collinear excitation pump at 532 nm. A supercontinuum light was generated up to around 575 nm, almost reaching the target of 600 nm required for testing the PCDA polymer coupled to NPs. Higher pump and probe powers may be needed to apply the SRS (and even more for the IRS technique). A proper pathlength of the sample cell may help in this direction too. The red PCDA coupled to gold nanoparticles is the material of choice to assess the SRS optical setup.

References

1. Kieu, K. *et al.* Demonstration of Zeno switching through inverse Raman scattering in an optical fiber. *Opt. Express* **19**, 12532 (2011).

2. Solli, D. R., Koonath, P. & Jalali, B. Inverse Raman scattering in silicon: A free-carrier enhanced effect. *Phys. Rev. A - At. Mol. Opt. Phys.* **79**, 1–4 (2009).

3. Kieu, K. *et al.* All-optical switching based on inverse Raman scattering in liquid-core optical fibers. *Opt. Lett.* **37**, 942–944 (2012).

4. Kieu, K., Schneebeli, L., Norwood, R. A. & Peyghambarian, N. Integrated liquid-core optical fibers for ultra-efficient nonlinear liquid photonics. *Opt. Express* **20**, 8148–8154 (2012).

5. https://en.wikipedia.org/wiki/Polydiacetylenes.

6. Jelinek, R. & Ritenberg, M. Polydiacetylenes-recent molecular advances and applications. *RSC Adv.* **3**, 21192–21201 (2013).

7. Alloisio, M. *et al.* Synthesis of fluorescent core-shell metal nanohybrids: A versatile approach. *Materials (Basel).* **9**, 417–425 (2016).

8. Dellepiane, G., Cuniberti, C., Alloisio, M. & Demartini, A. Spectroscopical properties of organic/metal nanohybrids. *Phys. Chem. Chem. Phys.* **12**, 2968 (2010).

CHAPTER 8

Conclusions

In this doctoral dissertation we examined organic conjugated systems for optoelectronics employing vibrational spectroscopic techniques to understand from a structural perspective the driving forces of aggregation and excited state relaxation of promising organic conjugated materials. In this chapter we summarize the main conclusions that derive from this thesis.

The main work presented in this dissertation focused on the water-soluble chemical system (MEG-PBI), because of its innovative interest and potential impact. The local structure of the supramolecular aggregate formed by this water-soluble PBI has been investigated in great detail in this study for the first time using vibrational spectroscopy in order to assess how its conformation can be affected by environmental conditions. Preliminary experiments performed at different concentrations and in thin film clarified that concentration of the sample and processing of the material (from solution to solid) does not affect its aggregation pattern in the range studied. Our RR investigations focused on monitoring the aggregation pattern of MEG-PBI in water and how it is influenced by the hydrophobic effect, as aggregation is an entropically-driven process, achieved here by increasing the temperature. Even though this technique has been utilized for the characterization of a wide variety of supramolecular systems, PBIs have not been yet analyzed by Raman spectroscopy in their J aggregated state, but only as individual molecules.

Our study revealed that in water a stiffer macrostructure is induced even in the monomer-like state, while monomers in toluene appear less tightly bound in the supramolecular structure. The two different J aggregates observed in the PBI structure cause differences in the spectral response and could potentially affect the excitonic coupling among the monomer units. Furthermore, computational methods of the normal modes of MEG-PBI confirmed the correlation of the varied vibrational fingerprint upon aggregation to specific structural changes of the structure of the aggregate. This analysis provided significant considerations about the structure of this

supramolecular system that can improve the understanding of the photophysical properties of such and similar systems. This will also support the development of innovative applications.

Beside the study on the water-soluble PBI, some preliminary comparative studies were realized on a PBI with a higher hydrophobicity of side chains, MEH-PBI, which confirmed the same pattern of aggregation of MEG-PBI upon the conversion from the monomer-like to the supramolecular J-aggregate phase, transition that spectroscopically appeared very clear for both PBI systems studied. An important change between the two molecules could be observed in the carbonyl area due to the stronger interaction of the MEH-PBI side chains with the organic solvent.

In the project dealing with the structural evolution of a series of oligofluorenes, we have obtained time-resolved excited state stimulated RR spectra for the first time, simultaneously with TA, which enables correlation of specific structural dynamics with dynamics observed with optical time-resolved spectroscopies. In particular, through FSRS spectroscopy we were able to directly observe mode-specific dynamics that provide insight on excited state localization and torsional relaxation from a twisted benzenoid conformation to a more planar quinoidal geometry.

We believe that the main goal of this dissertation, which was the structural characterization of the innovative 'aquamaterial' PBI and of the π-conjugated emitting OFs objects of study, is largely accomplished.

Future research is designed to complete the study and settle various issues that arose from the investigation on the stimulated/inverse Raman development which are briefly outlined in the next *Chapter*.

CHAPTER 9

Future work

A) Improvements of the stimulated / inverse Raman method

The guiding purpose of this project was to provide a technique of vibrational analysis, using nanosecond pulses and photonic fibers, in order to measure the Raman spectra for very fluorescent samples. The most useful advantage of such a method is indeed the absence of fluorescence, which is often a major issue with organic conjugated systems (as perylene bisimides).

Experiments on the fiber assessment carried out at UCY were performed using the same lasing source, for pumping and probing beams, with both pulses travelling simultaneously through the optical fiber. This optical arrangement, however, limits the power that can be used for the Raman pump, as the power necessary to observe the SRS/IRS signal is too high to be sustained in the optical fiber. Therefore, in order to better modulate the power of the two pulses we need to couple beams from different lasers, using a digital delay generator to synchronize them in time. Moreover, the sample cell can be optimized by achieving a longer pathlength. According to the literature, a fused silica capillary has been used before with a specific inner tube diameter (LCOF with 10, 5, and 2 μm inner diameters)[1]. This solution could provide a sufficient signal-to-noise for the stimulated Raman to be detected (expected to be more intense than the inverse signal). Carbon tetrachloride or a similar solvent with good Raman intensity peaks will be used in order to test the signal. Once a good outcome is successfully achieved with the testing molecule, the PCDA samples previously prepared will be measured and compared for a comparison in the signal-to-noise, among red and blue conformations, PCDA molecule alone or coupled to nanoparticles (silver or gold ones).

This possibility could provide clear specifics on the sensitivity of the method under study. The spectral range obtained throughout the optical fiber will hopefully offer the possibility to most probably perform the stimulated Raman (at higher wavelengths compared to the probe beam), rather than the inverse technique (on the higher frequency side of the probe beam), as our preliminary efforts have shown that the continuum extends primarily on the

higher energy side of the excitation beam. Considering the polydiacetylene sample, the whitelight continuum would be needed to extend up to 600 nm. We are very near that target.

This final stage of experiments can accomplish the target of improving a technique which can be a resource for samples with too much fluorescence to be tested with conventional Raman. Furthermore, a step towards a functional application (all-optical switching) could potentially result from the implemention of the inverse Raman technique.

B) Excited-state dynamics of OFs

In order to complete our interpretation of results from the excited-state dynamics study on the OFs system, we have initiated a collaboration with a theoretical group that will provide us with excited state dynamics simulations, as well as with excited state Raman calculations. Clear assignments of the excited state vibrational modes are necessary for a detailed and robust interpretation of the mode-specific dynamics we observe. In addition, this work will be extended to the polymer system for which we have preliminary data, so we can evaluate the extent of exciton localization and torsional relaxation in longer chains.

References

1. Kieu, K. *et al.* All-optical switching based on inverse Raman scattering in liquid-core optical fibers. *Opt. Lett.* **37**, 942–944 (2012).

References

CHAPTER 10

Appendix

Computational Results
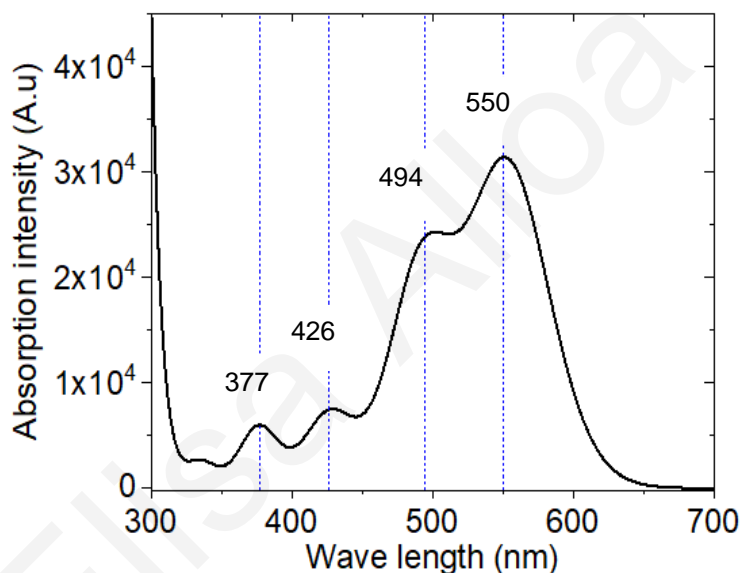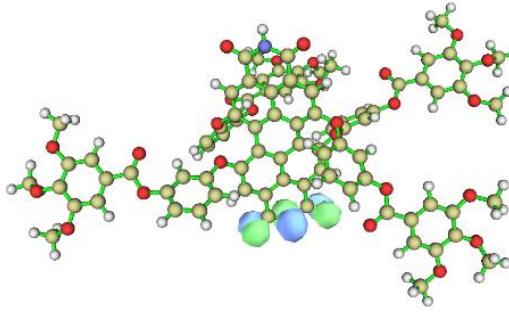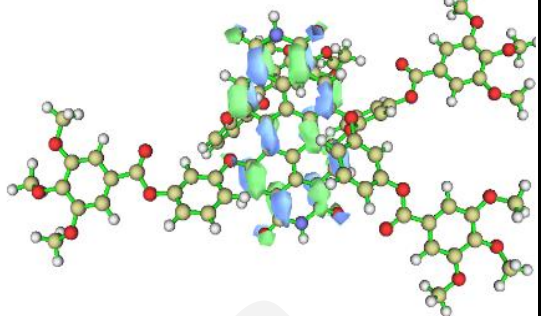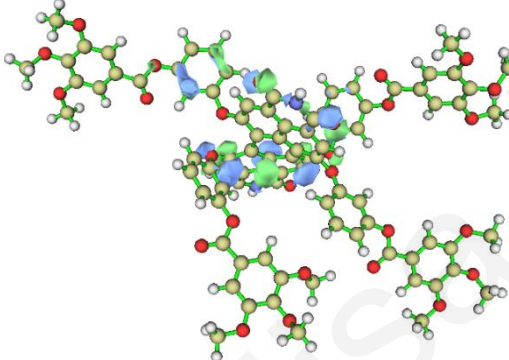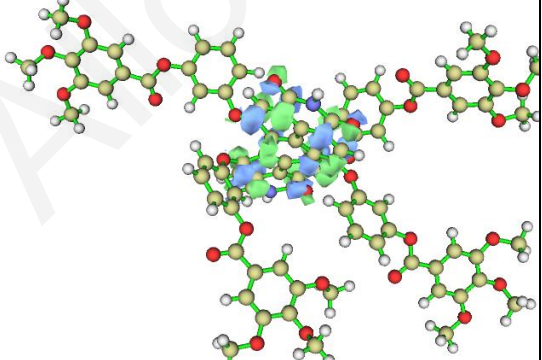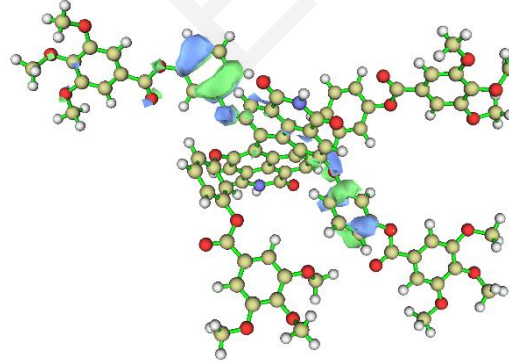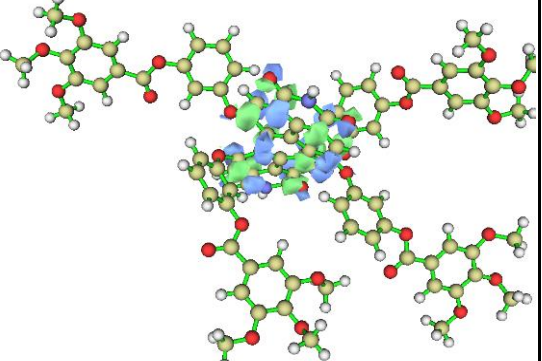
Figure 10-1 Calculated UV-Vis absorption spectrum. Each vertical line represents a transition for which the hole and electron NTOs are pictured in **Table 4-1**.

The TD-DFT calculations show two main absorption bands at ~530 and ~300 nm, in good agreement with the measured spectrum, see **Figure 4-1** in the main text. Analysis of the natural transition orbitals (NTOs, see **Table 10-1**) shows that, while the lowest optically-allowed electronic excitation is confined over the core of the molecule as expected, the higher-lying transition involves a redistribution of the electron density from the outer imide moieties, where the hole NTO is localized, to the inner part of the molecule. Note the accidental symmetry breaking for the localized holes (a similar NTO confined over the other imine group is predicted at close energy).

Table 10-1 Hole and electron NTOs for the major electronic transitions of MEG-PBI.

λ (nm)	Hole NTO	Electron NTO
300		
377		
426		
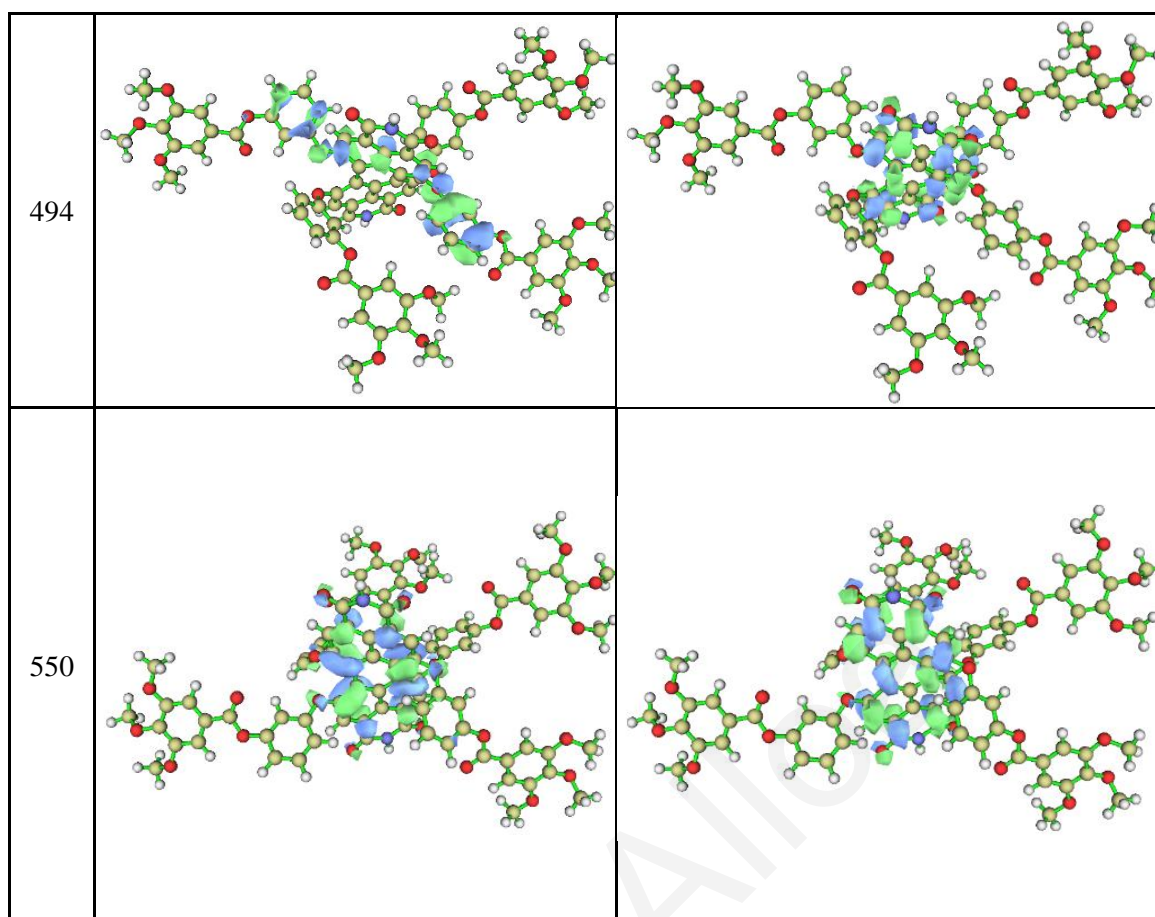
Table 10-2 Calculated coordinates for optimized ground state structure. The energy minimum of MEG-PBI was calculated as neutral species (charge = 0 and multiplicity singlet).

Coordinates	X	Y	Z
C	-2.53473300	-1.75721400	-4.47654200
C	-2.63345300	-1.48336700	-3.03522100
C	-1.47076500	-1.18077100	-2.28371900
C	-0.19578700	-1.12031000	-2.90206400
C	-0.05027500	-1.37623700	-4.34166600
C	-3.87539500	-1.56486200	-2.40785600
C	-1.58924200	-0.92400500	-0.88037900
C	-2.88748200	-0.81514200	-0.29293300
C	-3.99970200	-1.27105100	-1.05490900
C	-0.40350600	-0.77000400	-0.07674100
C	0.82006000	-0.58318100	-0.77714700
C	0.92150600	-0.77104400	-2.14804000
H	1.87432900	-0.63903400	-2.64903100
H	-4.73451500	-1.86448400	-2.99635900
H	-1.16193000	-1.85254400	-5.99809700
C	-2.98209800	-0.29707700	1.05596300
C	-1.85100100	-0.46603400	1.91768100
C	-4.09732800	0.40774800	1.58535400

132

C	-0.56419500	-0.81391100	1.36564200
C	-2.00411500	-0.25812600	3.32947500
C	-4.22688000	0.64924500	2.94312700
C	0.40928400	-1.18280100	2.32555200
C	-0.93552700	-0.56912600	4.20804500
C	-3.22470500	0.25997500	3.83320600
C	0.25758900	-1.06988100	3.68865200
C	-1.07653900	-0.40294900	5.65882600
C	-3.40424700	0.47343100	5.27458600
H	1.05318100	-1.35127900	4.36981200
H	-2.42268300	0.24370100	7.06318200
O	-0.20605300	-0.68654300	6.47936100
O	-4.41531100	0.93238300	5.79581400
O	1.01497000	-1.34504300	-4.95269200
O	-3.48155100	-2.05007200	-5.19997500
O	1.68995300	-1.70384100	1.92195100
O	-5.08065900	0.92025200	0.75310000
O	1.96727400	-0.21058900	-0.08052300
O	-5.19294300	-1.39730400	-0.38846100
C	2.58625500	0.97408800	-0.43895700
C	3.97942800	0.99388600	-0.37036100
C	1.87392500	2.11838400	-0.80597500
C	4.65473300	2.17085600	-0.68052300
H	4.53143200	0.10238500	-0.09611400
C	2.57789200	3.28107000	-1.11632800
H	0.79094400	2.09792300	-0.84826500
C	3.97216400	3.32347900	-1.06523500
H	2.02780900	4.17323600	-1.39961300
H	4.51265900	4.22815300	-1.31036100
C	-4.81753400	2.08809700	0.06776900
C	-3.67005100	2.85628800	0.26221500
C	-5.79153100	2.49707400	-0.84993200
C	-3.50424000	4.03028300	-0.47524600
H	-2.90666600	2.56948000	0.97373000
C	-5.60209600	3.67711000	-1.56213000
H	-6.67636800	1.88531400	-0.98990200
C	-4.46023400	4.46640600	-1.39034900
H	-6.35857200	3.99381700	-2.27469200
H	-4.31410200	5.37344900	-1.95804400
C	-6.18083200	-2.26954700	-0.79803100
C	-5.92619400	-3.58755700	-1.18712200
C	-7.48843000	-1.79509200	-0.70006600
C	-7.00369400	-4.41708400	-1.49784700
H	-4.90726700	-3.95289500	-1.24782300
C	-8.54419900	-2.65015500	-1.00487500
H	-7.67289500	-0.77601200	-0.38084500
C	-8.32102800	-3.96472800	-1.41578000
H	-6.81349800	-5.44087000	-1.80721400
H	-9.15137000	-4.61684200	-1.65064800
C	1.87283700	-2.94605600	1.58657700
C	3.21465200	-3.28537400	1.25305100
C	0.83451300	-3.94790800	1.55580400
C	3.52025500	-4.57289400	0.89303500
H	3.97092000	-2.51268000	1.28436600
C	1.16816200	-5.22798300	1.18287800
H	-0.17614500	-3.67121400	1.81864200
C	2.49074000	-5.56706800	0.82972900
H	0.40433400	-5.99595800	1.14281800
H	2.73231000	-6.56710000	0.50289000
O	4.80840300	-4.80495900	0.52322300
O	-9.81116500	-2.07350600	-0.95813600
O	-2.34341800	4.73139200	-0.14473300

O	6.04817100	2.07993000	-0.68386000
C	5.45162000	-6.02369300	0.78442400
C	-10.87109000	-2.72775600	-0.38562200
C	6.82322700	3.04075400	-0.09624500
C	-1.63747400	5.48752500	-1.03502600
C	-12.11011000	-1.90998000	-0.44819600
C	-12.15046700	-0.65211700	-1.04417700
C	-13.26352000	-2.45869600	0.13386000
C	-13.34343100	0.08145800	-1.06448600
H	-11.26945800	-0.21268900	-1.49384800
C	-14.45506600	-1.74295400	0.10630500
H	-13.19549900	-3.44218700	0.57963800
C	-14.50900200	-0.45607500	-0.48740200
C	6.85352600	-5.98238700	0.34851100
C	7.41965600	-4.84494700	-0.22752200
C	7.62585000	-7.13783100	0.56276900
C	8.76995100	-4.83669400	-0.59413700
H	6.84560800	-3.94289100	-0.39266100
C	8.96349300	-7.14491900	0.18464000
H	7.15519800	-8.00580800	1.00482700
C	9.55743100	-5.98829600	-0.38999300
C	8.27082600	2.73868700	-0.25281800
C	8.73911600	1.65597200	-0.99691600
C	9.17335500	3.60889400	0.37663000
C	10.11399100	1.44259900	-1.12703500
H	8.05879400	0.97706900	-1.49515900
C	10.54314300	3.38733700	0.27169200
H	8.77216700	4.43378100	0.95084400
C	11.03290000	2.30143300	-0.49679100
C	-0.39033700	6.01552600	-0.41554100
C	-0.03919600	5.75616700	0.91097700
C	0.44352900	6.79631000	-1.23321100
C	1.15865300	6.26140100	1.42207100
H	-0.66945400	5.15500800	1.55375600
C	1.63699200	7.30585300	-0.72434200
H	0.12854100	6.98403900	-2.25181500
C	2.00926600	7.03053700	0.61277300
O	6.38247600	4.01070300	0.48303700
O	-1.97329700	5.69504600	-2.18170900
O	-10.79598100	-3.83063500	0.11083100
O	4.87726300	-6.94304600	1.31992600
O	9.20428600	-3.69547300	-1.18673600
O	10.84003100	-5.99813400	-0.85096800
O	9.78303600	-8.22663800	0.29540300
O	1.51201700	5.93143000	2.70523500
O	3.16304700	7.54471400	1.13832500
O	2.51795900	8.07119200	-1.43024600
O	10.49915900	0.33077800	-1.83290400
O	12.36563100	2.00092800	-0.56726500
O	11.49136900	4.14389400	0.89734700
O	-13.28246700	1.27494300	-1.72345100
O	-15.69447000	0.22281500	-0.60287100
O	-15.64050900	-2.20873800	0.60017300
C	-14.01245700	2.40521000	-1.24754800
H	-15.06072700	2.36755500	-1.55107300
H	-13.94962100	2.48695100	-0.15499300
H	-13.52646800	3.27486900	-1.69723000
C	-16.33739800	0.62794500	0.61208500
H	-16.63303200	-0.23418600	1.21328200
H	-15.68043500	1.28186100	1.20058100
H	-17.22373200	1.18762400	0.30518000
C	-15.66532100	-3.51887900	1.15002700

H	-15.00909400	-3.60135300	2.02580600
H	-16.69922500	-3.69321800	1.45303100
H	-15.37077200	-4.26970200	0.40627700
C	9.23426300	-9.43983900	0.79796600
H	8.40792200	-9.79229600	0.16875800
H	10.04811000	-10.16560300	0.76987600
H	8.88330000	-9.32377100	1.83095800
C	11.89780900	-6.24070400	0.09003700
H	11.87151300	-5.49816200	0.89729900
H	11.83699600	-7.24664700	0.50789400
H	12.82328500	-6.12691000	-0.47723900
C	10.51035500	-3.17306900	-0.90758100
H	10.75758700	-3.28642400	0.15500600
H	11.27234000	-3.66577400	-1.51499800
H	10.45542000	-2.11035600	-1.15295800
C	11.05388200	5.20827100	1.73342000
H	10.42104000	4.83905000	2.54968600
H	11.96121800	5.65091400	2.14750100
H	10.50402400	5.96767800	1.16343300
C	13.24500500	2.99590600	-1.11094300
H	12.91336200	3.30123800	-2.11168900
H	13.30861200	3.87065200	-0.46159000
H	14.22249000	2.51447900	-1.18470700
C	11.46459200	0.48698900	-2.87659700
H	11.27331500	1.40136600	-3.45172200
H	12.48268900	0.50783700	-2.48069200
H	11.33878100	-0.37870200	-3.53156100
C	2.18417600	8.40136800	-2.77142900
H	1.24474700	8.96605600	-2.82312000
H	3.00271900	9.02444600	-3.13591900
H	2.09989300	7.50494000	-3.39944700
C	4.36809300	6.86839600	0.74559900
H	4.33537400	5.80970700	1.02121700
H	4.53720900	6.97051800	-0.33156800
H	5.17745700	7.36108300	1.28838100
C	1.54575900	7.01334000	3.64196800
H	2.28745500	7.76425100	3.35567800
H	0.55653100	7.48215100	3.72857500
H	1.81847200	6.56880600	4.60173900
H	-5.10673900	1.15905300	3.32028300
N	-2.30684000	0.10848000	6.06445700
N	-1.24214000	-1.67382700	-5.00272400